UNDERSTANDING AND IMPLEMENTATION OF HYDROGEN PASSIVATION OF DEFECTS IN STRING RIBBON SILICON FOR HIGH-EFFICIENCY, MANUFACTURABLE, SILICON SOLAR CELLS

A Thesis
Presented To
The Academic Faculty

by

Vijay Yelundur

In Partial Fulfillment
Of the Requirements for the Degree
Doctor of Philosophy in Materials Science and Engineering

Georgia Institute of Technology
November, 2003

UNDERSTANDING AND IMPLEMENTATION OF HYDROGEN PASSIVATION OF DEFECTS IN STRING RIBBON SILICON FOR HIGH-EFFICIENCY, MANUFACTURABLE, SILICON SOLAR CELLS

Approved by:

Dr. Ajeet Rohatgi, Advisor	Dr. C.P. Wong
Dr. William Brent Carter	Dr. Z. L. Wang
Dr. Meilin Liu	November 14, 2003 Date Approved

DEDICATION

This work is dedicated to

my parents, Rama and Geetha Rau Yelundur,

for their unwavering love, support, and kindness.

ACKNOWLEDGEMENTS

I would like to express gratitude to all of the past and present members of the University Center for Excellence in Photovoltaic Research and Education (UCEP) at Georgia Tech. I would like to express my deepest thanks to my thesis advisor, Dr. Ajeet Rohatgi, for providing me with many opportunities to develop my professional and technical skills, and the guidance and resources for this research. I would like to thank Sachin Kamra, Wayne Devezin, Dean C. Sutter and Ajay Upadhaya for their assistance in developing and maintaining device fabrication and characterization tools used extensively in this research. My sincere gratitude to Ms. Denise Taylor for coordinating my multidisciplinary research between UCEP and the School of Materials Science and Engineering. I would like to thank Dr. Brent Carter for serving as my academic advisor in the School of Materials Science and Engineering. I would also like to thank Dr. Jack Hanoka, Dr. Andrew Gabor, and Richard Wallace of Evergreen Solar for sharing their knowledge of industrial solar cell manufacturing and their support of this research. I would like to thank Dr. Dong Seop Kim, Dr. Stuart Bowden, Dr. Christiana Honsberg, and Dr. Abasifreke Ebong for sharing their experience and understanding of semiconductor device physics and characterization. I would like to express thanks to Alan Ristow, Ben Damiani, Ji-Weon Jeong, Aleksandar Pregelj, Michael Finnegan, and Mohamed Hilali for their friendship and dedication to photovoltaic research. Finally, I express my appreciation and deepest affection to my wife-to-be Jamie Howard for her love and encouragement throughout this research.

This work has been partially supported by Evergreen Solar through PVMaT and NIST contracts.

TABLE OF CONTENTS

LIST OF TABLES

LIST OF FIGURES

SUMMARY

Photovoltaics offers a unique solution to the energy and environmental problems simultaneously because unlimited sunlight serves as the fuel for solar cells, which generate electricity with and no air pollution, hazardous waste, or noise. However, widespread application of photovoltaics will not be realized until costs are reduced by about a factor of four. The goal of *The U.S. Photovoltaic Industry Roadmap* is to achieve an installed system, end-user cost of $3/Wp by 2010 and near $1.50/Wp by 2020. Currently, more than 85% of photovoltaic modules are based on monocrystalline or multicrystalline silicon. Silicon crystallization and wafering account for about 55% of the photovoltaic module manufacturing cost, which can be reduced significantly if a ribbon silicon material is used as an alternative to cast Si. String Ribbon Si is grown directly from the Si melt, eliminating the need for ingot slicing and the removal of surface damage from wafers. However, the growth of String Ribbon leads to a high density of electrically active bulk defects that limit the minority carrier lifetime and String Ribbon solar cell performance. While the growth of String Ribbon Si makes it an attractive material for low-cost silicon photovoltaics, the as-grown minority carrier lifetime in the material is typically 1-10 μs. Solar cell simulations performed in Chapter 3 clearly indicate that, for a 300 μm-thick device, the as-grown lifetime in String Ribbon silicon is not suitable for high-efficiency (>16%) screen-printed solar cells. However, cell efficiency increases sharply to 15.4% as the lifetime increases to 25 μs at which point, the back surface recombination velocity, S_b, begins to significantly impact solar

cell efficiency. High-efficiency screen-printed cells (>16%) can be achieved if the bulk lifetime is in excess of 75 μs, and S_b is less than or equal to 300 cm/s. Therefore, to fabricate high-efficiency screen-printed devices on String Ribbon Si, impurity gettering and defect passivation techniques that can improve the minority carrier lifetime in the material without significantly raising the cost must be developed and understood. The research tasks of this thesis focus on the understanding, development, and implementation of defect passivation techniques to reduce carrier recombination in the bulk of String Ribbon Si in order to enhance solar cell efficiency.

Task 1 of this thesis was to develop an Al-enhanced, low-cost bulk defect hydrogen passivation treatment using a plasma-enhanced chemical vapor deposited (PECVD) silicon nitride (SiN_x:H) anti-reflection coating. This task is addressed in Chapter 4, where it is shown that PECVD SiN_x:H-induced hydrogenation and Al gettering treatments combined in one heat treatment at 850°C for two minutes result in a noteworthy average lifetime improvement of 30 μs. This improvement in lifetime was far greater than the sum of the SiN_x:H hydrogenation and Al treatments alone, demonstrating that there is a positive synergistic interaction between the hydrogenation from the front surface and the Al alloying process occurring simultaneously at the back surface of the substrate.

The objective of Task 2 was to develop a physical model to explain the Al-enhanced, SiN_x:H-induced hydrogen passivation treatment. A three step physical model was proposed in Chapter 4 which demonstrates that hydrogen defect passivation from PECVD SiN_x:H during a post-deposition anneal depends on three processes: i) the release of hydrogen from the PECVD SiN_x:H film; ii) the retention of hydrogen at defect sites in

silicon; and iii) Al alloying at the back surface of the wafer. The model suggests that the synergistic effect of SiN_x:H-induced passivation in the presence of Al could be the result of the interaction of vacancies and hydrogen in Si and the high solubility of hydrogen in the Al-Si melt. Such interactions can increase the concentration and flux of atomic hydrogen in Si. As a result, the combination of hydrogenation and Al gettering effectively improved the lifetime in String Ribbon silicon beyond 30 μs even though the retention of hydrogen at defects in silicon is low at high temperatures.

The physical model for SiN_x:H-induced hydrogenation was validated in Task 3 through the appropriate implementation of Al-enhanced, SiN_x:H-induced hydrogen passivation to achieve high-efficiency String Ribbon solar cells. Chapter 5 demonstrated the importance of two components of the proposed physical model for SiN_x:H-induced hydrogenation, namely Al-Si alloying and hydrogen retention by rapid cooling. Partial Al coverage of the rear surface of String Ribbon samples eliminated thin wafer bowing, but decreased the spatially averaged lifetime enhancement to 80%, validating the importance of Al during hydrogenation. Chapter 5 also showed that the SiN_x:H-induced defect passivation can be improved by rapidly cooling samples at a rate of 40°C/s after the hydrogenation anneal. When rapid cooling was implemented in String Ribbon solar cell fabrication during contact firing after the hydrogenation, cell efficiencies as high as 14.7% with bulk lifetimes in the range of 25-30 μs. Rapid contact firing improved String Ribbon cell efficiency by an average of 1.2% (absolute) over slower belt furnace contact firing with a much lower cooling rate of 4°C/s, which may have led to the dehydrogenation of defects.

The goal of Task 4 was to provide further enhancement of defect passivation and bulk lifetime through in-situ NH_3 plasma pre-treatment and low-frequency (LF) plasma excitation during SiN_x:H deposition. In Chapter 6, high-frequency (13.56 MHz) PECVD SiN_x:H, deposited at 300°C, was replaced by low-frequency PECVD SiN_x:H, deposited at 430°C. Chapter 6 showed that LF SiN_x:H-induced hydrogenation increases the lifetime in String Ribbon to 92 μs and 62 μs with and without in-situ NH_3 plasma pretreatment, respectively. The SIMS depth profile of deuterium in Si after LF SiN_x:H deposition at 300°C from SiH_4 and ND_3 gases showed a surface concentration of 8×10^{18} cm^{-3}. Heat treatment after LF SiN_x:H deposition reduced the surface concentration for deuterium, suggesting that the incorporated hydrogen may act as an additional source of hydrogen during LF SiN_x:H-induced hydrogenation. However, SIMS depth profiles of deuterium in Si were unable to show enhanced H incorporation due LF SiN_x:H deposition or enhanced H diffusion in Si in the presence of Al alloying, presumably due to the high detection limit of deuterium. Therefore, to detect hydrogen in Si at lower concentrations and support the proposed hydrogenation model, another profiling technique, such the infrared spectroscopy should be used.

The objective of Task 5 was to investigate and optimize a rapid thermal anneal (RTA) to enhance LF SiN_x:H-induced hydrogenation for high-efficiency String Ribbon solar cells. This task is addressed in Chapter 7 which showed that optimum hydrogenation anneal temperature may be the result of competition between the supply of H from the SiN_x:H film and H stored near the Si surface, and the retention of H at defects. The optimum RTA temperature for high-frequency (HF) and LF SiN_x:H-induced hydrogenation in String Ribbon was found to be 800°C and 740°C, respectively. The

optimum RTA temperature for LF SiN_x:H-induced hydrogenation was implemented in String Ribbon solar cells as part of a two-step RTA scheme. Step 1 provided effective SiN_x:H-induced hydrogenation and was designed to have a fast ramp-up rate (50°C/s) to improve Al-BSF quality, but was not suitable for sintering the Ag contacts. Step 2, also performed in RTP, was designed for optimal Ag contact sintering and high retention of hydrogen at defects introduced in Step 1. String Ribbon solar cells fabricated with a two-step firing scheme that included LF SiN_x:H-induced hydrogenation performed at the optimum RTA temperature of 740°C had an average V_{oc} of 596 mV, an improvement of 13 mV over co-firing at 700°C for one second. The best String Ribbon solar cell fabricated with this two-step firing scheme had an efficiency of 15.6%. Room temperature scanning photoluminescence showed that the enhancement of band-to-band photoluminescence, proportional to lifetime enhancement, was maxim in the sample annealed at 740^{o}C, consistent with the lifetime and V_{oc} enhancements. Reduction of the average R-parameter, which is defined as the ratio of the intensity of the defect band photoluminescence to the band-to-band photoluminescence, was maximized in a sample annealed at 740°C. This result indicated that the initial active dislocation density in the sample was reduced by 67% by LF SiN_x:H-induced hydrogenation.

Lifetime degradation of pre-hydrogenated String Ribbon samples during subsequent heat treatment shown in Chapter 7 indicated that the anneal time must be reduced to avoid dehydrogenation. Very effective lifetime enhancement (6 μs to 92 μs) was observed during a short RTA (one second) even though the supply of H may be low. The high average lifetime achieved during one second RTA at 740°C is attributed to the decrease in dehydrogenation of defects for this short RTA. Record-high-efficiency

(17.8%) String Ribbon solar cells with photolithography defined contacts were fabricated to confirm that a short (one second) RTA can result in effective LF SiN_x:H-induced hydrogenation and the formation of a high-quality Al-doped back surface field.

The final task of this thesis was to fabricate record-high-efficiency, screen-printed String Ribbon Si solar cells by developing a single thermal treatment performed in a conveyer belt furnace for enhanced hydrogenation, back surface field, and screen-printed contacts. The optimum belt furnace firing cycle was identified in Chapter 8 and had a peak temperature of 753°C, a heating rate of 68.8°C/s, a cooling rate of 18.7°C/s, and a dwell time near the peak temperature of four seconds. String Ribbon samples annealed in this firing cycle for LF SiN_x:H-induced hydrogenation had an average lifetime of 77 μs, confirming that this anneal is suitable for effective defect passivation. String Ribbon solar cells fabricated with this firing cycle had an average efficiency of 15.2% and a maximum efficiency of 15.9%, which is the highest efficiency to date for a String Ribbon solar cell with screen-printed contacts. Light-biased internal quantum efficiency measurement and analysis with PC1D indicated that the effective surface recombination velocity in the 15.9%-efficienct String Ribbon cell was 300 cm/s. Thus, the belt furnace firing scheme developed in Chapter 8 not only provides effective defect passivation, but also forms an effective Al-doped back surface field. Solar cell simulations in Chapter 9 showed that planar String Ribbon solar cell efficiencies as high as 17.6% on 3 Ω-cm material with a lifetime of 140 μs could be achieved if the FF is improved to 0.78, S_b is reduced to 128 cm/s, the emitter doping is reduced from 40 Ω/sq. to 100 Ω/sq. coupled with a reduction in the front surface recombination velocity, the Ag front contacts coverage fraction is reduced, the cell thickness is reduced, and a good optical reflector is

applied to the rear surface. Further improvement of efficiency could be realized if the base resistivity is reduced, provided that the effects of dopant-defect interactions are mitigated. Finally, surface texturing could enhance the efficiency well over 18% if surface passivation and front contact quality can be maintained.

CHAPTER 1

Introduction and Research Objectives

1.1 Opportunities and challenges in photovoltaic power generation

The demand for energy is increasing at a rapid pace concurrent with a swift depletion of traditional energy resources. Since the availability of energy is critical for the advancement of civilizations around the world in the 21st century, energy will be an intensely sought commodity. In 2001, the world's energy consumption grew to 1.18 $x10^{14}$ kW-hr [1], and is expected to increase to $1.88x10^{14}$ kW-hr by 2025 [2]. Today, renewable energy resources contribute to only about 13% of the world's energy needs, of which 80% comes from biomass, mainly in non-commercial applications. A breakdown of the $2.84x10^{13}$ kW-hr of energy consumed in the U.S. in 2001 is shown in Figure 1 [1] and indicates that 86% of the energy came from the burning of fossil fuels, which produces harmful greenhouse gases such as CO_2 [1]. In addition, the burning of crude oil and coal for electric power generation contributes about ⅔ of U.S. SO_2 emissions [3], which is a main cause of acid rain. The remaining 14% of energy in the U.S. comes from

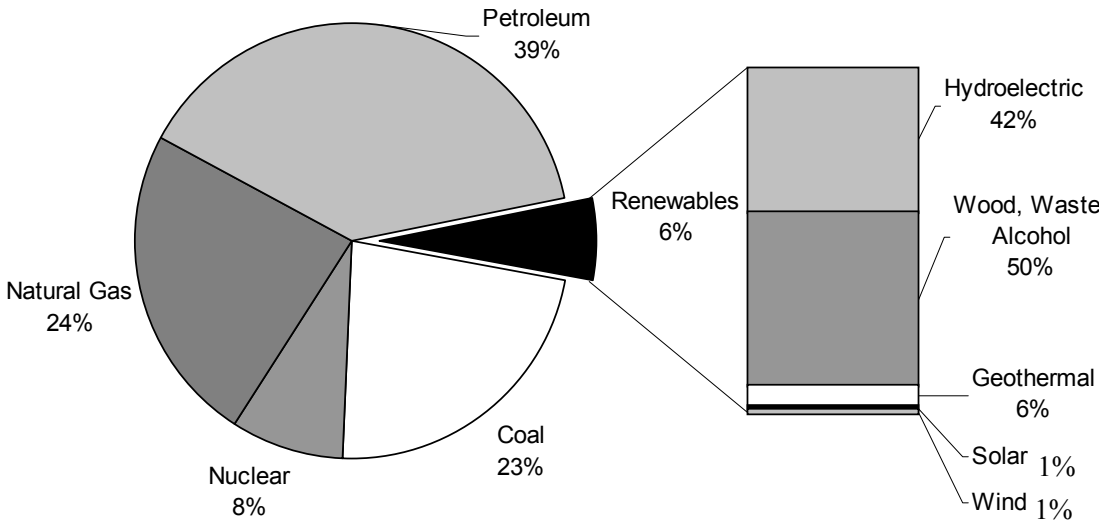

Figure 1. Renewable energy share of total U.S. energy consumption, 2001 [1].

nuclear power and renewable energy sources. While nuclear power generation does not contribute to harmful emissions, it does result in the production of dangerous nuclear waste that is costly to treat and store. Figure 1 [1] shows that hydroelectric power is the second most widely consumed renewable energy source in the U.S. Although hydroelectric power generation is considered to be a renewable energy resource, it negatively impacts the ecosystem surrounding the water source. Wind power is the fastest growing renewable energy resource. The worldwide total installed capacity for wind energy grew to 31,000 MW in 2002, a year in which 6,868 MW [4] of wind power was installed. However, in many applications wind power is not the proper energy solution because wind power generation is noisy, occupies a large amount of space, and is harmful for birds, causing controversy in the environmental community. Among renewable energy sources, solar energy is particularly attractive because it is free, unlimited, and it is not localized in any part of the world. Photovoltaics (PV) is the direct

conversion of sunlight into electrical energy using a semiconductor device called a solar cell. PV offers a unique solution to the energy and environmental problems simultaneously because sunlight serves as the fuel and no air pollution, hazardous waste, or noise are produced during power generation. PV is attractive to potential users because PV systems do not require the transportation of fuels and they can be sized according to the user's needs. The basic element of a PV system is the solar cell, which are connected together in a PV module, which generally provides 100-200 Wp of clean energy. PV modules are connected with power conditioning equipment, which includes a DC/AC power inverter. PV systems can be connected to the electric utility grid or operate with a battery bank in remote areas where the grid is not accessible.

Figure 1 [1] shows that solar energy, including PV, supplies only 1% of U.S. renewable energy and is less than 0.1% of the total energy portfolio. However, the worldwide demand for PV continues to grow as indicated by a 25-30% annual

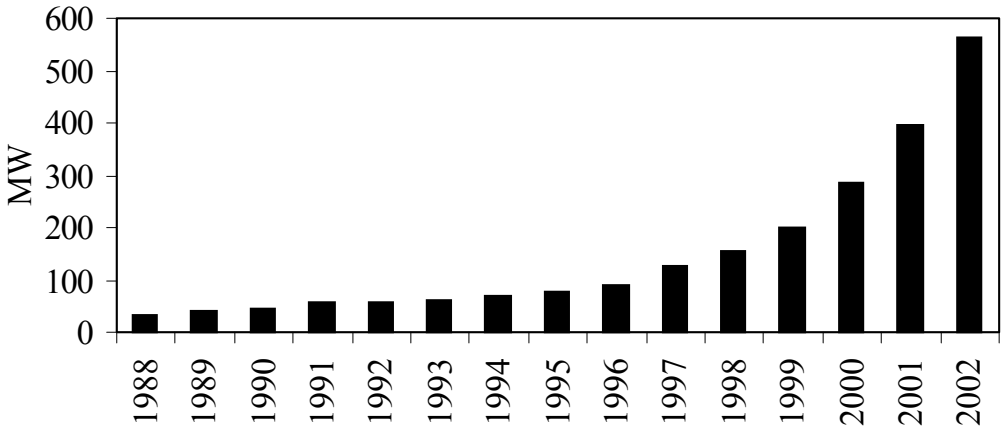

Figure 2. Worldwide photovoltaic module shipments, 1988-2002 [5].

increase in PV module shipments in recent years, as shown in Figure 2 [5]. Photovoltaic module prices continue to decrease and have followed an historical trend consistent with an 80% progress ratio, PR, shown in Figure 3. A PR of 80% indicates that PV module prices are decreasing by 20% for every doubling of total cumulative PV module production worldwide [6]. In 2001, the value of the 396 MW of PV modules delivered was estimated at $2,067.5 million and this value is expected to nearly double by 2006 [7].

Recognizing that a large and growing market for PV exists, representatives from the

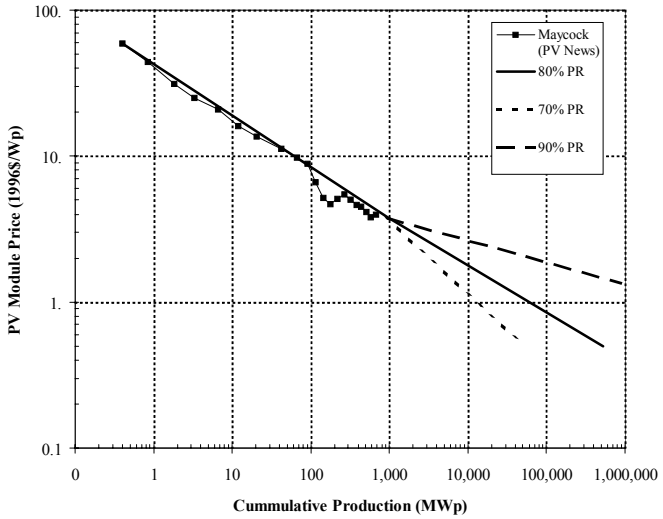

Figure 3. PV module production experience curve [7].

U.S. PV industry, Department of Energy, and academia have convened to develop the *U.S. Photovoltaic Industry Roadmap* [8] to guide U.S. PV research, technology, manufacturing, markets and policy through 2020. The endpoint goal for the roadmap is "*For the domestic photovoltaic industry to provide up to 15% (about 3200 MW) of new U.S. peak electricity generating capacity expected to be required in 2020. The*

cumulative U.S. PV shipments will be about 30 GWp at this time." At the present growth rate of 25%/year, PV may account for 10% of the total energy production in the U.S. by 2030. The overall goals outlined in the roadmap can be categorized in two areas – installed volume of photovoltaics measured in MWp and the cost of the PV system measured in $/Wp.

Currently, PV modules alone cost $3-4/Wp, with 88% of the market based on crystalline silicon (Si) technology. The cost goal of the *PV Industry Roadmap* is an installed system, end-user cost of $3/Wp by 2010 and near $1.50/Wp by 2020. In 1997, a cost analysis of a hypothetical 500 MWp Si PV module fabrication facility performed by the European Commission found that multicrystalline Si ingot crystallization and wafering account for 55% of the total module fabrication cost, while solar cell fabrication and module assembly account for 12% and 33% of module fabrication cost respectively [9]. A major loss in crystallization and wafering is the slicing of wafers in which a kerf loss of 50% is common using the current multi-wire wafer sawing technology. The findings of the European Commission's study illustrate that a significant reduction in the total manufacturing cost of Si PV modules can be achieved if silicon crystallization and wafering costs are reduced by eliminating the kerf loss.

Another driving force for the reduction of crystallization and wafering costs is the recent increase in the demand for high-purity Si feedstock. Most of the feedstock Si for PV comes from polycrystalline or single-crystal Si material rejected from the integrated circuit (IC) industry, which has impurity levels suitable for Si PV. Current projections indicate that the Si available from the IC industry alone will support only 220-440 MW of Si PV in 2003 [10]. As the Si PV industry grows and the production efficiency of IC

silicon improves, demand for suitable purity Si feedstock will quickly outgrow supply, and the cost of Si feedstock will rise. Solar cell technologies that consume less Si, by reducing the Si wafer thickness, or use the feedstock more efficiently, by eliminating kerf loss, will have a cost advantage in an economic environment of rising Si feedstock costs. *Therefore,* a *major focus of this work is the investigation of a novel multicrystalline ribbon silicon material that reduces silicon crystallization and wafering costs, without sacrificing solar cell performance*.

To meet the *PV Industry Roadmap's* installed volume target of 3200 MW for 2020 at $1.50/W, Si PV manufacturing is restricted to high-volume, high-throughput, technologies, such as conveyer belt furnace processes and screen-printing. Historically, these high-volume, high-throughput technologies limit the implementation of solar cell design features that enhance solar cell efficiency. However manufacturing processes that lead to high-efficiency solar cells contribute to cost savings by reducing the amount of Si, glass, and module support materials required per Wp. Therefore, this work seeks to provide some resolution to this challenging problem by fabricating high-efficiency cells on low-cost Si material by developing low-cost, high-volume solar cell fabrication technologies. A combination of materials characterization, device modeling, and technology development is used extensively to achieve low-cost, manufacturable, high-efficiency cells to reduce the cost of Si photovoltaics.

1.2 Specific Research Objectives

To meet the production volume and cost goals identified in the PV Roadmap, the cost of PV module manufacturing must be reduced and the solar cell efficiency must increase. Low-cost ribbon Si materials reduce crystallization and wafering costs, but their growth leads to a high density of electrically active bulk defects that limit solar cell performance. There is a need to develop cost-effective bulk defect gettering and passivation techniques that can be easily integrated into the solar cell fabrication sequence and enable the fabrication of high-efficiency solar cells. The key requirements for achieving high-efficiency solar cells on a low-cost Si material are 1) bulk defect passivation to reduce bulk carrier recombination, 2) rear surface passivation to reduce surface recombination, and 3) high-quality metallization to reduce carrier recombination at the contact interface. This study focuses on the understanding, development, and implementation of defect passivation techniques to reduce carrier recombination in the bulk of Si solar cells in order to enhance solar cell efficiency. The specific research objectives of this study are detailed below.

1.2.1 Task 1: Develop an Al-enhanced, low-cost bulk defect hydrogen passivation treatment using plasma-enhanced chemical vapor deposited silicon nitride anti-reflection coating

An obvious approach towards reducing the cost of silicon photovoltaic modules is to reduce the cost of the silicon substrate, which accounts for 40-55% of the current module

cost. The String Ribbon silicon growth process can reduce the cost of substrate growth because ribbon substrates for solar cells are grown directly from the melt, eliminating the losses associated with slicing and subsequent etching. Another advantage of String Ribbon silicon is that it can be grown to a thickness' below 100 μm, rather than the current commercial solar cell thickness of 300 μm, resulting in further material and cost savings. While the growth of String Ribbon silicon makes it an attractive material for low-cost silicon photovoltaics, the as-grown minority carrier lifetime in the material is limited to one to ten microseconds due to the presence of electrically active extended defects and impurities. Solar cell simulations show that the as-grown lifetime in String Ribbon silicon is not suitable for high-efficiency (>15%) screen-printed solar cells, and there is only a small impact of back surface passivation. However, the cell efficiency increases sharply as the lifetime increases to 25 μs or higher. Therefore, to fabricate high-efficiency screen-printed devices on String Ribbon silicon we must understand and develop impurity gettering and defect passivation techniques that can improve the minority carrier lifetime in the material without significantly raising the cost.

In this task, an atomic hydrogen defect passivation technique is developed using plasma-enhanced chemical vapor deposition of SiN_x:H individually and in combination with phosphorus and aluminum gettering. The aim of this task is to increase the bulk lifetime in String Ribbon beyond 25 μs, where device simulations indicate that solar cells with efficiencies in excess of 15% may be realized. SiNx:H films deposited by PECVD perform several functions in a silicon solar cell. SiN_x:H films contain atomic hydrogen that may be used to passivate electrically active bulk defects during a post-deposition anneal. SiN_x:H films also serve as an effect anti-reflection coating, a surface passivation

layer, and prevent excessive penetration of the screen-printed silver paste during contact firing. To maintain the cost-effectiveness inherent in String Ribbon Si, the heat treatments in this study will be performed in a conveyer belt furnace. In addition, commercially available phosphorus spin-on dopants and screen printable aluminum pastes will be used. The phosphors and aluminum gettering techniques employed will also be used in the formation of an n^+ emitter that is compatible with screen-printed front contacts and a high-quality aluminum-doped back surface field. Particular emphasis will be placed on exploiting the presence of Al on the rear of solar cells to enhance the defect hydrogenation from SiN_x:H. Carrier lifetime enhancement in String Ribbon samples will be evaluated using the quasi-steady state photoconductance technique.

1.2.2 Task 2: Develop a physical model the for the Al-enhanced, SiN_x:H-induced hydrogen passivation treatment

A physical model will be proposed to improve the fundamental understanding of SiN_x:H-induced hydrogen passivation. The model will relate PECVD SiN_x:H-induced hydrogenation of defects to the supply of hydrogen released into the substrate, the retention of hydrogen at defect sites at high temperatures, and backside Al alloying. The development of the model will be based on the behavior of hydrogen in silicon and the interaction of hydrogen with point defects in silicon.

1.2.3 Task 3: Validate the physical model through the appropriate implementation of Al-enhanced, SiN_x:H-induced hydrogen passivation to achieve high-efficiency solar cells on a low-cost Si material

The physical model for the Al-enhanced SiN_x:H-induced hydrogenation of defects in Si will be used to design experimental strategies that provide additional support and verification of the model. Of particular interest are process conditions identified through application of the model that improve SiN_x:H-induced hydrogenation by increasing the supply and retention of hydrogen in Si. The effect of rapid cooling after the post-deposition anneal of SiN_x:H on hydrogen passivation will be investigated using a rapid thermal processing furnace (RTP) to improve the retention of hydrogen at defects and provide further lifetime enhancement. In addition, the effect of Al alloying on back of the wafer during hydrogenation will be studied by controlling the amount of Al coverage of the back surface. The physical model will be further supported by the implementation of Al-enhanced SiN_x:H-induced hydrogenation of defects to fabricate high-efficiency, manufacturable String Ribbon Si solar cells. Rapid cooling will be implemented in the rapid thermal firing (RTF) of screen-printed contacts, which is performed after the simultaneous formation of a screen-printed Al-doped back surface field and SiN_x:H-induced hydrogenation to improve defect passivation and contact quality. For comparison, cells will also be fabricated by using a conventional lamp heated belt furnace, which is characterized by slow heating and cooling rates. Solar cells will be analyzed by light-beam induced current (LBIC) mapping and internal quantum efficiency (IQE).

1.2.4 Task 4: Further enhancement of defect passivation through in-situ NH_3 plasma pre-treatment and low-frequency plasma excitation during SiN_x:H deposition

While Al may play an important role in increasing the supply of hydrogen during SiN_x:H-induced passivation, Al alloying is not compatible with thin Si substrates because the difference in the thermal expansion coefficients of Al and Si produces stresses which cause thin wafers to bend. Consequently, the goal of this task is to further increase the lifetime in String Ribbon to 100 μs or higher by enhancing the supply of hydrogen without relying on Al-Si alloying. In this task, further lifetime enhancement is sought through atomic hydrogen incorporation in silicon via ion bombardment near the substrate surface during PECVD SiN_x:H deposition using a low plasma excitation frequency. In addition, the effect of NH_3 plasma pre-treatment will be investigated for enhanced hydrogen incorporation and hydrogen passivation of defects in String Ribbon Si. Hydrogen incorporation in Si during PECVD treatments will be characterized by secondary ion mass spectroscopy (SIMS) profiling of deuterium in Si. Hydrogen incorporated in the Si wafer during PECVD SiN_x:H deposition and subsequent anneal will be compared with the release of hydrogen from SiN_x:H films. This study will involve detecting hydrogen by Fourier transform infrared spectroscopy (FTIR).

1.2.5 Task 5: Investigate and optimize a rapid thermal anneal to enhance low-frequency SiN_x:H-induced hydrogenation for high-efficiency String Ribbon solar cells

The hydrogen stored in the SiN_x:H film and incorporated in the Si wafer near the front surface must be driven into the Si wafer during a post-deposition anneal. The post-deposition anneal must be designed to maximize the release of stored hydrogen, while preventing dehydrogenation of passivated defects during prolonged anneals at high temperatures. Rapid thermal annealing (RTA) appears to be suitable for the post-deposition hydrogenation anneal because high heating and cooling rates on order of 50-100°C/s can be achieved. RTA also offers accurate control of the sample temperature and the hold time at the peak temperature. In this task, the optimum RTA temperature for hydrogenation will be identified through a combination of solar cell analysis, carrier lifetime enhancement, and room temperature mapping of the photoluminescence response of String Ribbon solar cells. In addition, the presence of hydrogen in silicon will be confirmed by FTIR detection of Pt-H pairs in hydrogenated Si wafers.

1.2.6 Task 6: Fabricate record high-efficiency String Ribbon Si solar cells by developing a single thermal treatment for enhanced hydrogenation, back surface field, and screen-printed contacts

The main objective of this task is to achieve a record-high-efficiency solar cell on String Ribbon Silicon using optimized SiNx:H deposition and a single thermal treatment for hydrogen in a continuous belt furnace. The hydrogen anneal will be merged with screen-printed Ag and Al contact firing to form a high quality Al-doped back surface

field and Ag front contacts. A post-deposition anneal of the SiN_x:H film is required to redistribute atomic hydrogen incorporated near the surface of the Si substrate. At the same time, commercial String Ribbon solar cells suffer from a FF response that is generally in the range of 0.73 to 0.74. A heat treatment that simultaneously serves as the hydrogenation anneal and contact firing in a continuous belt furnace is desirable to reduce the number of high temperature steps in solar cell processing. Important aspects of this anneal such as the peak temperature, dwell time, and cooling rate, which can be controlled by the setpoint temperatures and belt speed will be investigated. The appropriately designed conveyer belt furnace anneal will be implemented in the fabrication of record high-efficiency screen-printed String Ribbon silicon solar cells. Finally, through device simulation and characterization by internal quantum efficiency, the rear surface recombination velocity in String Ribbon solar cells will be evaluated and guidelines for the next generation of high-efficiency, manufacturable String Ribbon solar cells will be established.

CHAPTER 2

A Review of Silicon Solar Cell Operation and the Impact of Impurities and Defects on Carrier Recombination

2.1 Silicon solar cell operation

Solar cells are semiconductor devices that operate by directly converting sunlight into electrical energy. The energy conversion efficiency of a solar cell is defined as the ratio of the maximum power generated by the solar cell (P_{max}) to the energy of the incident light (P_{in}) as follows

$$\eta = \frac{P_{mas}}{P_{in}} = \frac{J_{sc} \bullet V_{oc} \bullet FF}{P_{in}} \quad (1)$$

where J_{sc} is the short circuit current, V_{oc} is the open circuit voltage, and FF is the fill factor. A basic silicon solar cell is composed of an n-p junction, front and rear electrical contacts, and an anti-reflection coating. Most commercial silicon solar cells are fabricated using boron doped, p-type silicon wafers into which phosphorus is diffused to form an n^+-emitter layer and an n-p junction near the front surface as shown in Figure 4.

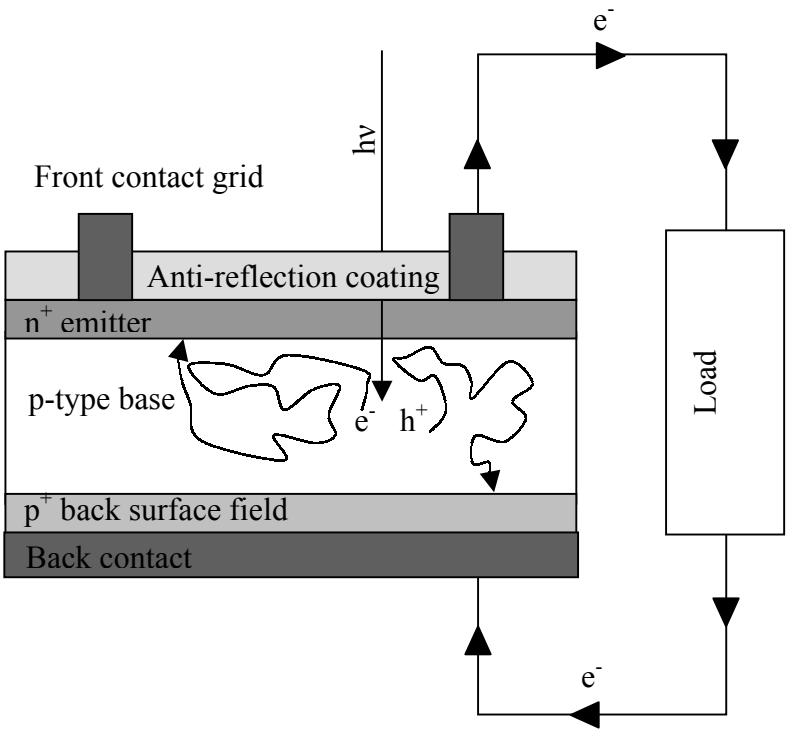

Figure 4. Structure of a basic silicon solar cell.

When light with energy greater than the band gap (E_g^{Si}=1.12eV) strikes a solar cell, electrons and holes are generated in the semiconductor layers and diffuse randomly. Electrons in the base are minority carriers and diffuse close to the n-p junction where they are swept into the emitter by the very high local electric field and extracted to the external circuit through the electrical contacts. Solar cell efficiency is typically characterized by three parameters as shown in (1) and identified in Figure 5: V_{oc}, J_{sc}, FF. V_{oc} can be expressed as

$$V_{oc} = \frac{kT}{q} \ln\left(\frac{J_{sc}}{J_o} + 1\right) \qquad (2)$$

where k is the Boltzman constant, T is the temperature, q is the unit charge, and J_o is the reverse saturation current density. J_o links V_{oc} to the device and material properties of the solar cell and can be expressed as

$$J_o = \frac{qD_n n_i^2}{L_n N_D}\left[\frac{S_f L_p / D_p + \tanh\left(W_n / L_p\right)}{1 + S_f L_p / D_p \tanh\left(W_n / L_p\right)}\right] + \frac{qD_p n_i^2}{L_p N_A}\left[\frac{S_b L_n / D_n + \tanh\left(W_p / L_n\right)}{1 + S_b L_n / D_n \tanh\left(W_p / L_n\right)}\right] \quad (3)$$

where $D_{n,p}$ is the diffusivity of electrons or holes, $L_{n,p}$ is the minority carrier diffusion length of electrons or holes, $N_{A,D}$ is the base and emitter doping level, n_i is the intrinsic carrier concentration, $W_{n,p}$ is the thickness of the emitter or base, and $S_{f,b}$ is the front or back surface recombination velocity. Equations 2 and 3 show that V_{oc} is strongly

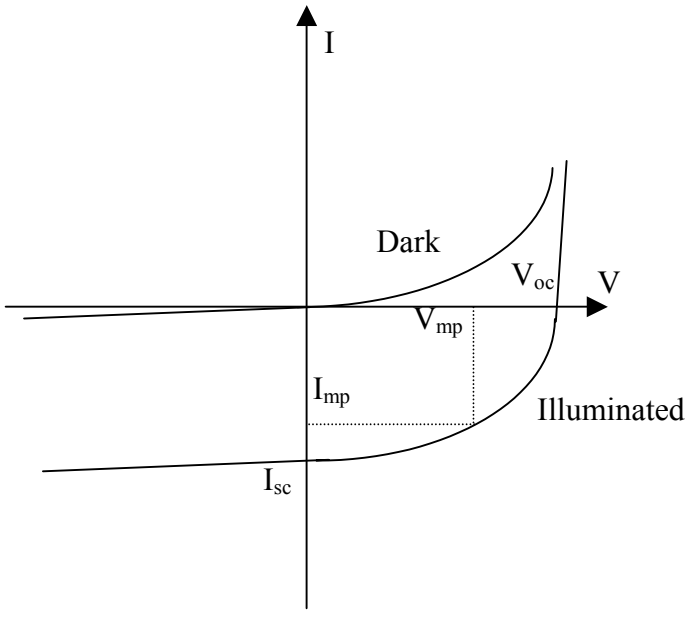

Figure 5. Current-voltage characteristic of a solar cell.

dependent on the surface recombination velocities, minority carrier diffusion length, device thickness, and doping level. Like V_{oc}, J_{sc} is strongly affected by bulk and surface recombination of minority carriers in all regions of the device. In addition, J_{sc} is affected by the optical properties of the solar cell such as the quality of the anti-reflection coating and light trapping schemes. The FF is a measure of the squareness of the I-V curve and is an indicator of the quality of the metallization. The FF depends on the total series resistance of the cell and the presence and magnitude of all shunt elements. Elements of a solar cell contact that effect the FF can be evaluated through the use of the dc equivalent circuit shown in Figure 6 where J_L is the photogenerated current density, R_{sh} is the shunt resistance across the n^+-p junction, J_1 is the total recombination current density in the emitter and base regions, J_2 is the recombination current density in the depletion region, and R_s is the total series resistance of the cell.

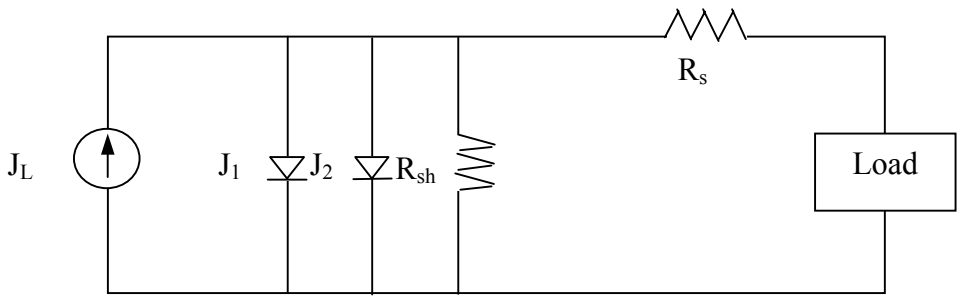

Figure 6. DC equivalent circuit of an n^+-p solar cell.

2.2 Electron-hole recombination in the bulk

Recombination of photogenerated electron-hole pairs significantly limits solar cell efficiency. Recombination is typically characterized by the effective carrier lifetime τ_{eff}, which is defined as

$$\tau_{eff} = \frac{\Delta n}{U} \tag{4}$$

where U is the net recombination rate and Δn is the excess carrier concentration. The effective lifetime in Si solar cells must be maximized to allow photogenerated carriers to reach the collecting junction. The effective lifetime is composed of the bulk lifetime, τ_r, and surface lifetime, τ_s as follows

$$\tau_{eff} = \frac{1}{\tau_s^{-1} + \tau_r^{-1}} \tag{5}$$

The bulk recombination lifetime is determined by three electron-hole pair recombination mechanisms: 1) Shockley-Read-Hall (SRH) recombination; 2) radiative band to band recombination; and 3) Auger recombination. The total bulk recombination lifetime, τ_r, is

$$\tau_r = \frac{1}{\tau_{SRH}^{-1} + \tau_{rad}^{-1} + \tau_{Auger}^{-1}} \tag{6}$$

given by

where τ_{SRH} is the Shockley-Read-Hall recombination lifetime, τ_{rad} is the radiative recombination lifetime, and τ_{Auger} is the Auger recombination lifetime. In SRH recombination, electrons and holes recombine through intermediate energy levels in the band gap, shown in Figure 7 (c), and energy as is released mainly through lattice vibrations. The energy levels in the band gap or traps are characterized by a trap density

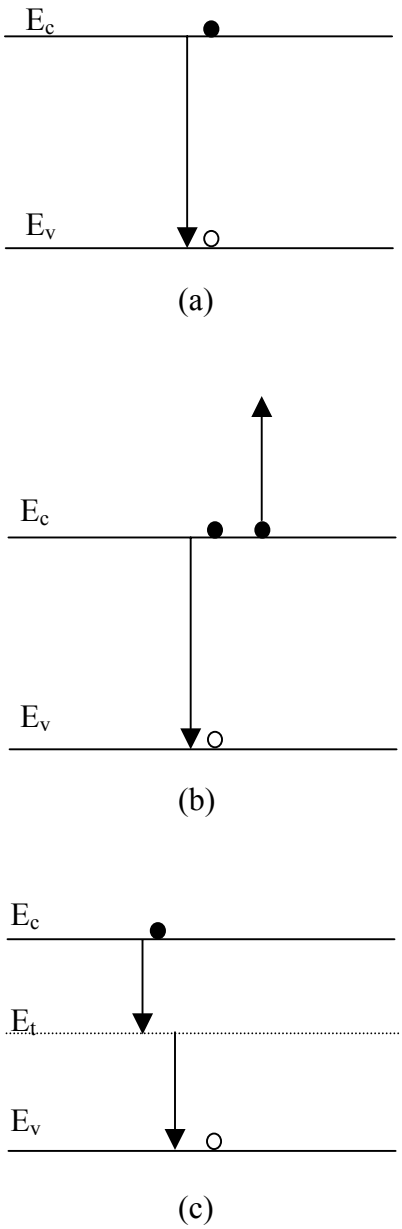

Figure 7. Illustration of recombination processes in silicon: (a) radiative band to band; (b) Auger; (c) Shockley-Read-Hall.

N_T, trap energy level, E_T, and capture cross sections for electrons and holes, σ_n and σ_p. The SRH lifetime is given by (7) below [11]

$$\tau_{SRH} = \frac{\tau_{po}(n_o + n_1 + \Delta n) + \tau_{no}(p_o + p_1 + \Delta p)}{p_o + n_o + \Delta n} \tag{7}$$

$$n_1 = n_i e^{(E_T - E_i)kT} \tag{8}$$

$$p_1 = n_i e^{-(E_T - E_i)kT} \tag{9}$$

$$\tau_{po} = \frac{1}{\sigma_p v_{th} N_T} \tag{10}$$

$$\tau_{no} = \frac{1}{\sigma_n v_{th} N_T} \tag{11}$$

where p_o and n_o are the hole and electron concentrations in equilibrium, Δp and Δn are the excess hole and electron concentrations and n_1, p_1, τ_{po}, and τ_{no} are defined as [11] Radiative recombination involves electrons and holes directly from band to band as shown in Figure 7 (a) and energy is released as photons. The radiative recombination lifetime is inversely related to the carrier concentration and is given by [11]

$$\tau_{rad} = \frac{1}{B(p_o + n_o + \Delta n)} \tag{12}$$

where B is the radiative recombination coefficient equal to 2×10^{-15} cm^3/s in Si [11]. In Auger recombination, a third carrier (majority carrier) absorbs the energy released from a radiative recombination event as shown in Figure 7 (b), and τ_{Auger} is inversely related to

$$\tau_{Auger} = \frac{1}{C_p\left(p_o^2 + 2p_o\Delta n + \Delta n^2\right)} \quad (13)$$

the square of the carrier concentration as followswhere C_p is the Auger recombination coefficient equal to 0.1 to 1.1 x 10^{-30} cm^6/s in Si [11].

2.2.1 Impact of defects and impurities on solar cell performance

2.2.1.1 Properties of transition metal impurities and their effect on silicon solar cell performance

Metal impurities degrade Si solar cell performance primarily by introducing SRH centers in the band gap that reduce the minority carrier diffusion length in the base. Transition metals are the most detrimental impurities in silicon solar cells because they can be found in the silicon growth environment, and have energy levels near mid-gap, high diffusivities, and high solubilities. The energy levels, diffusivity, and solubility for common transition metal impurities in silicon are listed in Table 1 [12]. Impurities such as Cr, Mn, Fe, Co, Ni, and Cu are well known as fast diffusers in silicon, and are particularly harmful if found in the material growth environment. However, the high diffusivity of metal impurities in silicon often improves the effectiveness of external impurity gettering techniques. The diffusivity for transition metal impurities generally increases with atomic number with Cu having the highest diffusivity. Substitutional

Table 1. Trap position, solubility, and diffusion coefficient at 1000°C for transition metal impurities in Si [12].

Transition Metal	Atomic Number	Trap position (eV)	Impurity solubility in Si at 1100°C (cm^{-3})	Diffusion coefficient in Si at 1100°C (cm^2/s)
Ti	22	E_v+0.30 E_c-0.26	2×10^{13}	6×10^{-11}
V	23	E_v+0.42 E_c-0.22 E_c-046	1×10^{13}	1×10^{-7}
Cr	24	E_v+0.22 E_v+0.31 E_c-0.25	3×10^{14}	2×10^{-6}
Mn	25	E_v+0.40	3×10^{15}	3×10^{-6}
Fe	26	E_v+0.40	3×10^{15}	4×10^{-6}
Co	27	E_v+0.35 Ec-0.54	4×10^{15}	1×10^{-5}
Ni	28	E_v+0.23 E_c-0.49	5×10^{17}	4×10^{-5}
Cu	29	E_v+0.24 E_v+0.4 E_v+0.53	9×10^{17}	1×10^{-4}

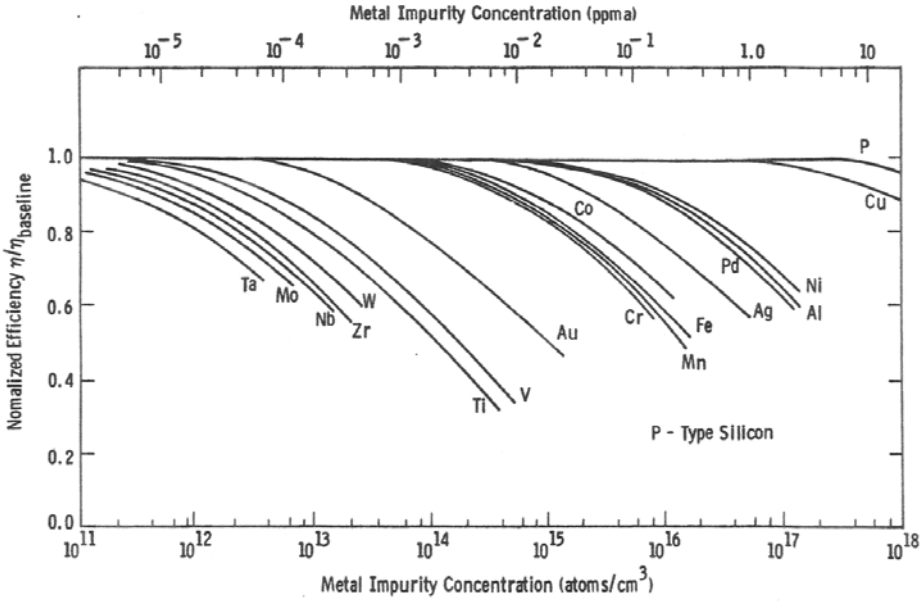

Figure 8. Effect of various impurity concentrations on single crystal silicon solar cell performance [13].

impurity diffusion is somewhat retarded in Si and the diffusion coefficient can be 10^{-11} cm^2/s even at temperatures near the melting point of Si. Among the metallic impurities that occupy substitutional sites in silicon are Au and Pt. The solubility of transition metals also increases with atomic number as shown in Table 1. Highly supersaturated and mobile transition metal impurities show a strong tendency for silicide precipitation, electrical behavior of which is discussed in the next section. An analytical model developed by Davis et al. predicts the threshold concentration for metallic impurities in Czochralski Si, above which solar cell efficiency declines due to carrier lifetime reduction [13]. The results of the model shown in Figure 8 show that some impurities such as Al, Ni, Cu and Ag do not significantly reduce solar cell performance until concentration levels of 10^{15} cm^{-3} are reached. Metal impurities such as Ti and V are more detrimental and concentrations of only 10^{14} cm^{-3} lead to a 50% (relative) reduction

in solar cell efficiency. The effect of Ti on EFG solar cells has be studied by Borenstein et al. [14] who found that a Ti concentration of $4x10^{-13}$ in the space charge region reduces solar cell efficiency to 60% of its original value, in good agreement with Figure 8.

2.2.1.2 Impact of metal precipitates on solar cell performance

The impact of fast diffusing impurities can be mitigated by gettering techniques and as a result, transition metals in the dissolved state do not present an insurmountable problem for silicon solar cells. However, metal precipitates are highly stable in silicon and are not easily dissolved in a reasonable thermal budget. Most metals precipitate as silicon rich, thermally stable metal silicides (MSi_2), and precipitation usually occurs heterogeneously at lattice defects or other impurity clusters. Metal precipitates themselves may not produce deep level states responsible for recombination, but they may affect solar cell performance by creating a conductive shunt element across the depletion region of the n-p junction. Segregation and precipitation of impurities at grain boundaries and dislocations in mc-Si has been observed in intentionally contaminated samples by Auger electron spectroscopy (AES) and secondary ion mass spectroscopy (SIMS) [15], and in uncontaminated samples by synchrotron based x-ray fluorescence [16]. Analysis of the x-ray absorption spectra of sub-micron size Fe precipitates in Si has shown that precipitates may be in multicrystalline Si as oxides or silicates. This makes precipitate dissolution difficult because of the high binding energy of Fe atoms to oxides and silicates [16]. The precipitation rate of Fe has been studied in solar-grade materials including float zone, Czochralski, and EFG Si [17]. In low defect density materials such as float zone and Czochralski silicon, Fe precipitation occurs at a low rate and most of the intentionally diffused Fe can be gettered. In EFG Si wafers, Fe precipitation occurs at a

higher rate and is enhanced by heterogeneous nucleation at intragranular microdefects, dislocations, and grain boundaries. The precipitation of Fe in EFG Si has a lasting effect, and even after gettering the diffusion length cannot be improved substantially.

2.2.1.3 Effect of defect complexes in solar performance

Impurities in silicon may interact with defects, dopants, or other impurities to form defect complexes. Two important impurity complexes in solar grade silicon are the FeB complex and and BO complex. Interstitial Fe is positively charged near room temperature in p-type silicon and forms pairs with shallow level acceptors such as B. The FeB complex has a donor level at E_v+0.1 eV and an acceptor level at E_c-0.29 eV, while Fe_i has an acceptor level at E_v+0.40 eV [18]. Both Fe_i and FeB are strong recombination centers, but the recombination activity for FeB is about ten times lower than that of Fe_i. The FeB complex can be dissociated at temperatures of about 200°C or illumination of high intensity light [18]. This has important consequences for Si solar cells because a high level of Fe contamination may be present in multicrystalline Si wafers, but undetectable because of FeB formation. However, FeB pair dissociation during solar cell operation increases the interstitial Fe concentration, and reduces the carrier lifetime.

Another defect complex that is detrimental to solar cell performance is the BO complex. Carrier injection processes such as forward bias and illumination stimulate the formation of the BO complex and for this reason, the effect of the defect is commonly referred to as light induced degradation or LID. Activation of the metastable boron-oxygen defect complex results in an efficiency degradation of 3-7% (relative) in commercially manufactured, B-doped Czochralski Si solar cells. While the chemical structure of this defect is not fully understood, the impact of the defect on the carrier

lifetime in Czochralski silicon has been studied in detail [19,20]. Two defect generation rates have been observed, indicating that the defect formation process is composed of two steps. The first defect formation step results in a fast initial degradation of carrier lifetime and occurs in the first 200 seconds of light illumination. In this step, an interstial O dimer is transformed to an active configuration ($O_{2i} \rightarrow O_{2i}^{*}$). The second step occurs during the next ten hours of illumination, when the fast O_{2i}^{*} is captured by substitutional B to form the electrically active, metastable BO_{2i} defect complex. Recently, it has been shown that there is a quadratic dependence of the normalized defect concentration (N_t^{*}) on the interstitial oxygen concentration ($[O_i]$) for $[O_i]>4x10^{17}$ cm^{-3}, and a linear dependence for lower oxygen concentrations [21]. A linear dependence of N_t^{*} on the substitutional B concentration has also been found. The impact of LID can be greatly reduced through the use of magnetic stabilization of the melt during Czochralski silicon growth to reduce the incorporation of oxygen, and the use of Ga as a p-type dopant in Czochralski silicon [22].

2.2.1.4 Effect of extended defects solar cell performance

Extended defects such as grain boundaries and dislocations are prevalent in multi-crystalline silicon used in the majority of commercially manufactured solar cells. Grain boundaries are not considered to be significantly deleterious to solar cell efficiency, because the grain size in multicrystalline silicon is several millimeters and many times greater than the thickness of a crystalline silicon solar cell. However, enhanced recombination is observed if there is a high degree of asymmetry at the grain boundary [23] and there is impurity segregation [18]. Intragranular dislocations result from the stresses created by high thermal gradients during the growth, and are the most common

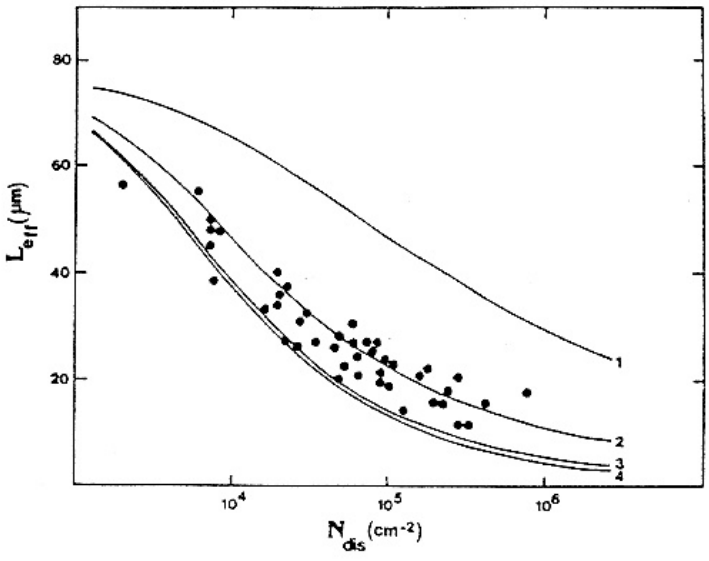

Figure 9. Modeled and experimental results of the effect of dislocation density on L_{eff} for various S_d : 1- S_d=10^3cm/s; 2 - S_d =10^4 cm/s; 3 - S_d = 10^5 cm/s; 4 - S_d = 10^6 cm/s [25].

defect in ribbon multicrystalline silicon materials, where the dislocation density is in the range of 10^5-10^6 cm^{-2}. The effect of the density (N_{dis}) and recombination strength (S_d) of dislocations on solar cell performance has been modeled by El Ghitani et al. [24]. This model considers a density of dislocation (N_{dis}) that are perpendicularly oriented to the solar cell surface and are surrounded by a space charge region with a surface recombination velocity, S_d. El Ghitani's model predicts that the photocurrent and effective minority carrier diffusion length (L_{eff}) will decrease when the dislocation density of is greater than 10^3 cm^{-2}, and the impact is larger when the $S_d \geq 10^4$ cm/s, as shown in Figure 9. Experimental results have shown that recombination at dislocations limit L_{eff} when N_{dis} and S_d exceed 10^4 cm^{-2} and 1000 cm/s, respectively [25]. The recombination strength of dislocations is strongly enhanced by impurity decoration.

Electron hole pair recombination at impurity-decorated dislocations in silicon can be understood through a description of the electronic band structure around the dislocation core. Figure 10 shows the band structure of an impurity decorated dislocation and is composed of shallow dislocation bands, E_{De} and E_{Dh}, induced by the dislocation strain field, and a deep level, E_M, caused by a segregated impurity [26]. The probability of a recombination event directly between E_{De} and E_{Dh} is low, and as a result the recombination rate through the channel $R_{De\text{-}Dh}$ is low. The presence of the deep level E_M near midgap introduces the additional recombination channels R_{De}-M and R_{Dh}-M, and

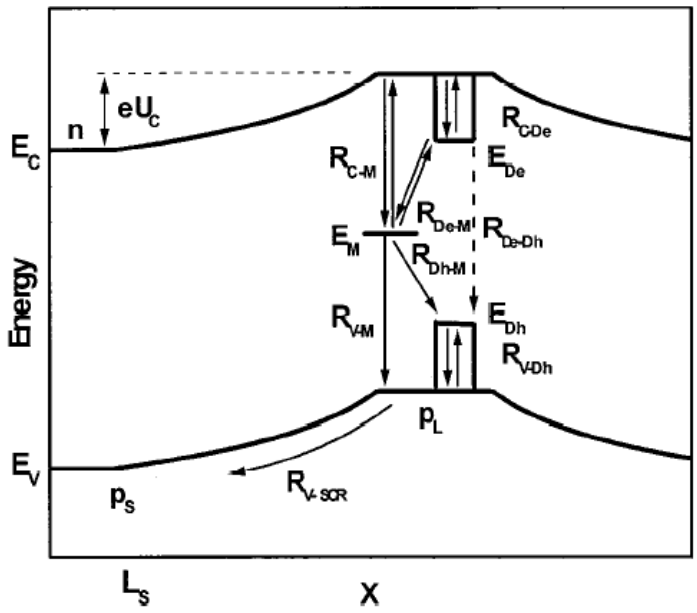

Figure 10. Energy band diagram of an impurity-decorated dislocation. Recombination in clean dislocations proceeds directly from E_{De} to E_{Dh} through recombination channel $R_{De\text{-}Dh}$. Impurity decoration introduces a deep level center at energy level E_M and adds the $R_{De\text{-}M}$ and $R_{Dh\text{-}M}$ recombination channels [26].

increases the recombination rate dramatically. The energy level of the segregated impurity has little effect on the recombination activity as long as the impurity level is deeper than E_c-0.3 eV. In general dislocations and impurities are non-uniformly distributed throughout a multicrystalline wafer. As a result, the carrier lifetime in multicrystalline silicon can show significant variance from wafer to wafer or within a single wafer. The clustering of defects, such as dislocations, stacking faults, and grain boundaries, can also have a profound influence on the performance of large area solar cells made on multicrystalline silicon. In addition to mediating electron-hole pair recombination, defect clusters act as shunts, dissipating power internally in the solar cell due to the parallel interconnection of good and bad regions. Impurity decoration of defect clusters enhances the shunt behavior and cannot be resolved by conventional impurity gettering treatments.

2.2.2 Measurement of the bulk lifetime in solar-grade silicon wafers

Carrier recombination lifetimes in silicon are commonly determined from photoconductance (PC) data or the photoconductance decay (PCD) transient after excitation by a laser, flash lamp, or LED array. In the PCD technique, measurement of the decay transient is made upon termination of a rapidly decaying light pulse by use of an rf-bridge circuit that senses the photoconductance of the silicon wafer. The effective lifetime of carriers in a sample during PCD measurement is expressed as

$$\tau_{eff} = -\frac{\Delta n}{\partial \Delta n / \partial t} \tag{14}$$

where Δn is the photo-induced excess carrier concentration and t is time. A typical PCD apparatus is capable of accurately measuring carrier lifetimes greater than 50 μs. A drawback of the PCD technique is that the measurement of low lifetimes, common in industrial grade silicon, requires the use of fast electronics to capture the decay transient and an illumination source with a steep cut-off.

Recently a technique known, as quasi-steady state photoconductance [27], has been developed to directly relate the carrier lifetime to the steady-state photoconductance. During steady-state illumination, the rates of photo-generation and recombination events are balanced and may be expressed in terms of current density

$$J_{ph} = J_{rec} = qU \tag{15}$$

where J_{ph} and J_{rec}, are the generation and recombination rate of electron hole pairs expressed as current densities, an U is the electron-hole pair recombination rate. The total recombination in a sample of thickness W can be written as [28]

$$J_{ph} = \frac{q\int_0^W \Delta n dx}{\tau_{eff}} = \frac{q\Delta n_{av} W}{\tau_{eff}} \tag{16}$$

where Δn_{av} is the average excess electron carrier concentration through the sample thickness. The increase in electron and hole concentration during illumination results in an increase in the conductance of the sample under test. The difference between the dark and illuminated conductance, or excess photoconductance, is given by [28]

$$\Delta\sigma_L = q\int_0^W \left(\Delta n\mu_n + \Delta p\mu_p\right)dx \approx q\Delta n_{av}\left(\mu_n + \mu_p\right)W \tag{17}$$

where μ_n and μ_p are the electron and hole mobilities. It should be noted that the approximation in (17) assumes that the variation in mobilities with carrier concentration can be accommodated by evaluating them at the average excess carrier concentration. Equations 16 and 17 must be combined to arrive at an expression for the carrier lifetime [28].

$$\tau_{eff} = \frac{\Delta\sigma_L}{J_{ph}\left(\mu_n + \mu_p\right)} \tag{18}$$

The instrumentation used in this thesis was developed by Sinton Consulting and utilizes a flash lamp with an exponentially decaying light pulse. The decay constant of the flash lamp is greater than the lifetime of the carriers in the sample and a so-called quasi-steady state condition of electron-hole pair generation and recombination is established. The decay of the light intensity during the flash pulse allows the determination of the effective lifetime over a range of excess carrier concentrations. The lifetime measurement relies upon the use of a calibrated instrument with an rf-bridge circuit to detect the conductance of the sample, and a reference solar cell to measure the illumination intensity as depicted in Figure 11. Current flowing through a coil under the test sample creates a magnetic field that induces Eddy currents in the sample. The power loss resulting from the interaction of Eddy currents and the sample is proportional to the conductance of the sample. An increase in the conductance causes an increase in the power loss and a

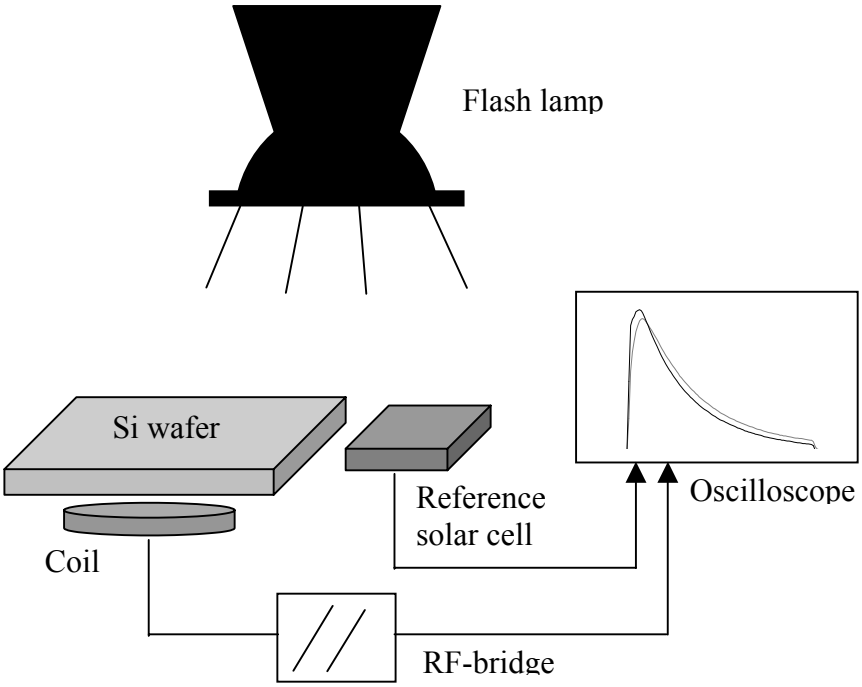

Figure 11. Configuration of the QSSPC lifetime measurement apparatus developed by Sinton Consulting and used in this thesis.

reduction of the Q-factor of the coil. The circuit relates the Q-factor to a voltage output displayed on an oscilloscope. The coil is calibrated by placing a series of samples each of known conductance, and measuring the output voltage. The illumination intensity is determined by measuring the voltage across a resistor connected in series with the reference solar cell. This measured voltage is compared with the known voltage measured at one Sun (one Sun = 100 mW/cm^2) to determine the illumination intensity during the measurement. A linear dependence of J_{ph} on the illumination intensity is assumed and a value of J_{ph}=38 mA/cm^2 is used for a 300 μm thick sample at an illumination intensity of one Sun. Figure 12 shows the voltage traces for the output of the reference solar cell and the RF-bridge circuit. A spreadsheet calculates the effective lifetime of the sample using (19) below where T is the transmissivity of the wafer.

$$\tau_{eff} = \frac{\Delta\sigma_L}{\boldsymbol{J}_{ph,1Sun} \cdot \boldsymbol{T} \cdot \boldsymbol{Suns} \cdot \left(\mu_n + \mu_p\right)} \tag{19}$$

The corresponding excess carrier concentration is determined by

$$\Delta \boldsymbol{n} = \frac{\Delta\sigma_L}{\boldsymbol{qW}\left(\mu_n + \mu_p\right)} \tag{20}$$

Knowledge of some properties of the test sample including the doping level, transmissivity, and thickness is required. Equations 19 and 20 applied to the measured voltage data in Figure 12 (a) to produce a plot of the effective lifetime as a function of excess carrier concentration shown in Figure 12 (b). Quasi-steady state lifetime measurements of defective Si materials often show abnormally high lifetimes at low-injection levels. This phenomenon has been attributed to the presence of shallow level

traps located near the edge of the conduction band that trap electrons, but do not contribute to recombination [29]. The trapped electrons lead to an excess of holes, resulting in a larger photoconductance and lifetime than would be expected without traps. The effect of shallow traps on the lifetime measurement can be mitigated if traps are filled, which occurs at an injection level of 10^{15} cm^{-3} [29].

As indicated by (4) the bulk lifetime can be approximated by the effective lifetime if the surface recombination velocity approaches zero. In this work, bulk lifetime measurements are performed on samples whose surfaces have been thoroughly cleaned in the series of solutions listed in Appendix A. After surface cleaning, samples are individually immersed in a solution of 70 mg I_2 in 250 mL of methanol, which has been shown to reduce the surface recombination velocity to below 10 cm/s on single crystal silicon [30].

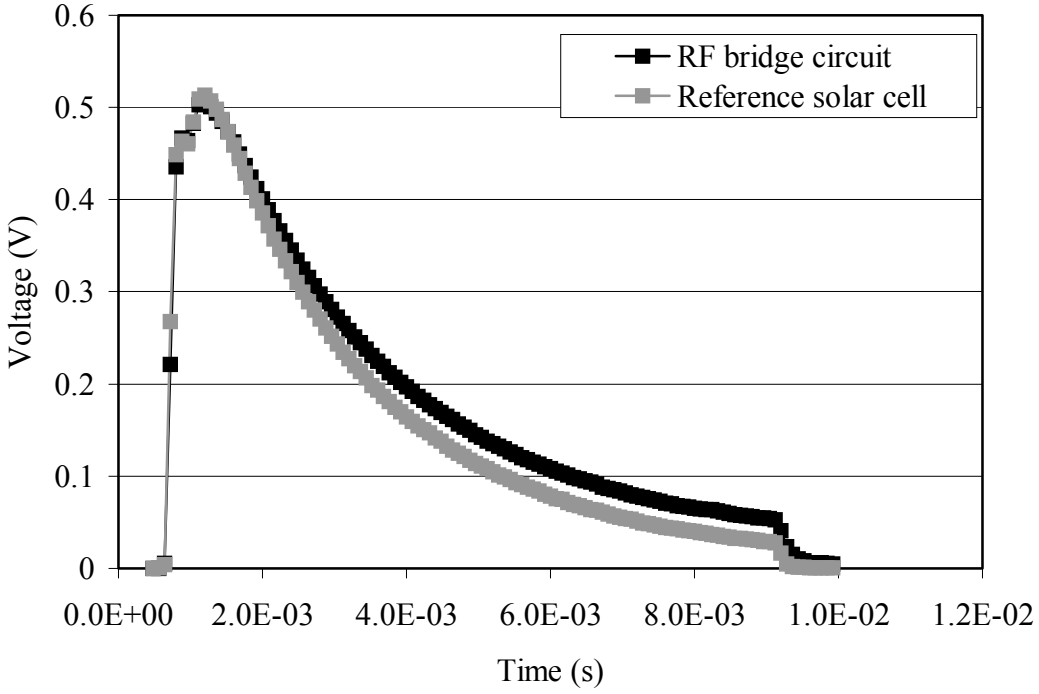

(a)

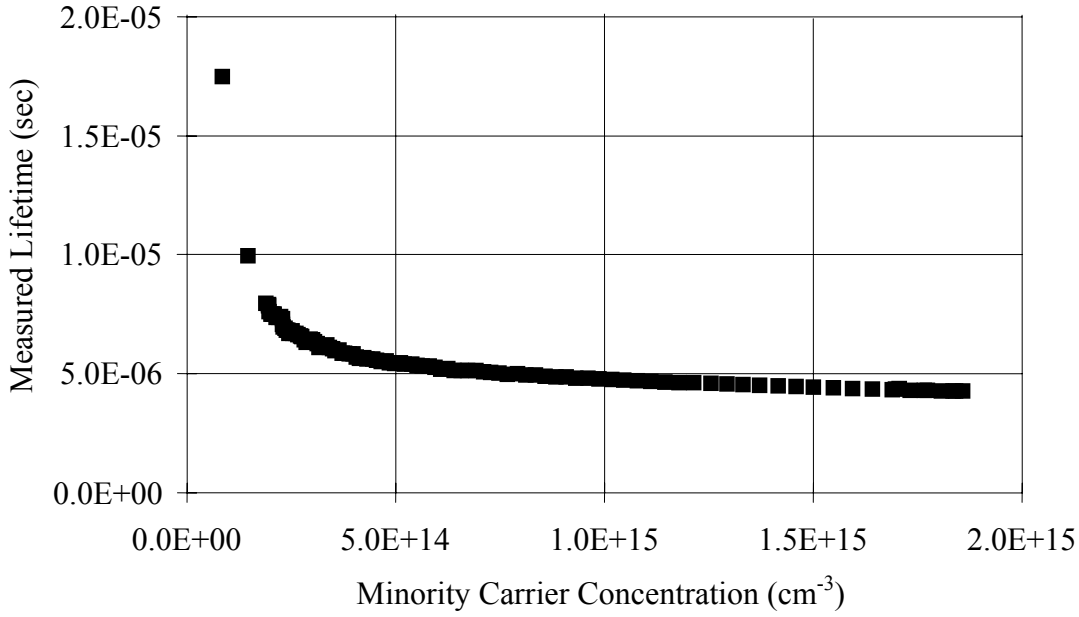

(b)

Figure 12. Measurement of carrier lifetime by QSSPC technique showing (a) output of RF-bridge circuit and reference solar cell and (b) measured lifetime as a function of minority carrier concentration.

CHAPTER 3

History of Low-cost and High-efficiency Silicon Solar Cells

In an effort to achieve its aggressive long-term cost goals, the *U.S. Photovoltaic Industry Roadmap* has set a mid-term R&D milestone to develop an 18% solar cell fabrication line in the next three to five years using low-cost thin Si materials. While solar cell efficiencies in excess of 18% have been demonstrated on multicrystalline silicon materials, cell fabrication involved multiple high-temperature and photomask steps that make costs prohibitively high for commercial purposes. In addition, ingot based multicrystalline silicon solar cells have been unable to meet the cost target of $1/W due in part to a high cost of crystallization and wafering. In contrast, ribbon silicon substrates are pulled directly from the melt, eliminating the need for wafering. As a result, ribbon silicon materials have the potential to reduce the silicon crystallization and wafering costs that plague ingot based silicon technologies. However, a high density of electrically active defects limits the as-grown minority carrier lifetime in ribbon silicon materials to less than 10 μs, which is too low for achieve high target efficiencies. Model calculations performed in this chapter indicate that the key to improving solar cell efficiencies to 16% and higher is lifetime enhancement to 75 μs. Several impurity

gettering and defect passivation techniques have been developed to improve the as-grown lifetime in silicon for photovoltaic applications. Phosphorus and Al gettering are effective in improving the lifetime, but require high temperatures (≥800°C) and long processing times (more than one hour) due to their dependence on impurity diffusion. In contrast hydrogen passivation of defects in silicon can be performed at low temperatures for short times due to the high diffusivity of hydrogen in silicon. Hydrogen passivation can be performed during solar cell processing by utilizing the hydrogen available in PECVD SiN_x:H films, which are used for anti-reflection coating. In this chapter, the state of the art in crystalline silicon solar cell research is reviewed with particular emphasis on the growth, characterization, and fabrication of solar cells on ribbon silicon. In addition, widely used impurity gettering and defect passivation techniques are discussed.

3.1 A review of high-efficiency laboratory scale and manufacturable silicon solar cells

Single crystal Si solar cell efficiencies as high as 24.7% have been achieved using expensive float zone Si and laboratory scale processing, both of which are not suitable industrial manufacturing. Multicrystalline Si (mc-Si) is better suited to meet the low-cost and high-volume production goals of large scale Si PV due to its lower crystallization cost. In the 1980s, the performance of laboratory scale mc-Si solar cells reached only 17% due to the presence of performance limiting defects and impurities. Directionally solidified and cast mc-Si wafers are generally characterized by large grains (a few mm)

and a high density of intragranular defects such as dislocations, twins, vacancies, self-interstitials, and impurities such as carbon, oxygen, and transitions metals. The simultaneous presence of these defects makes their interaction very complex. The rate of defect interactions increases with temperature, making it difficult to predict the effect of solar cell processing steps, such as phosphorus diffusion and SiO_2 growth, which are performed at elevated temperatures (800°C).

Recent breakthroughs in mc-Si solar cell efficiencies have been achieved through an improved understanding of the behavior of defects in mc-Si during thermal processing, concurrent with improvements in the control of mc-Si ingot growth. In 1996, Georgia Tech reported the highest efficiency (18.6%) planar, mc-Si device using 0.65 Ω-cm cast mc-Si material grown by the heat exchanger method (HEM) and laboratory-scale processing technologies [31]. Cell fabrication involved a 900°C/30 minute phosphorus n^+-emitter diffusion followed by a second high temperature step, which provided excellent SiO_2 emitter surface passivation, aluminum back surface field (Al-BSF) formation, and hydrogen passivation of defects via forming gas anneal (FGA). High quality front contacts were formed by photolithography and a double layer anti-reflection coating (ARC) was applied. Then in 1999, the highest mc-Si cell efficiency (19.8%) was reported by the University of New South Wales using 1.2 Ω-cm, 260 μm thick, Eurosolare cast mc-Si in conjunction with passivated emitter, rear locally-diffused (PERL) solar cell technology [32]. This technology involves multiple high temperature and photomask steps to achieve a phosphorus diffused selective emitter, local boron-doped back surface field, excellent front and back SiO_2 passivation with point contacts on the rear, front and back photolithography contacts, and a sophisticated honeycomb

textured surface also formed by photolithography. The solar cell processes necessary to achieve these world record efficiencies involve over 16 hours of manual labor and include multiple energy consuming high temperature steps that are clearly inappropriate for high-volume, high-throughput production. However, these results demonstrate that low-cost Si materials are capable of exceeding the 18% efficiency target set by the PV Roadmap if high-efficiency features are included in the solar cell design. The challenge in Si PV is to incorporate solar cell design features which raise the cell efficiency while using high-volume, high-throughput manufacturing technologies and low-cost materials.

Today, commercial mc-Si solar cell efficiencies lie in the range of 12-15%, but research is under way to improve these efficiencies. Sharp Solar, the world leader in sales of PV modules, announced the highest efficiency manufacturable mc-Si solar cell (16.7%) in 2000 using a high-volume solar cell fabrication process [33]. This process involved chemical texturing of a cast mc-Si substrate in a NaOH/IPA solution to reduce surface reflection, followed by phosphorus n^+-emitter diffusion in lateral quartz tube. The emitter was capped with a SiN_x:H film deposited by PECVD which serves as a single layer anti-reflection coating, a surface passivation dielectric, and a source of hydrogen for bulk defect passivation. Finally, front and rear contacts were screen-printed and co-fired. While this result demonstrates that cast mc-Si substrates can be used to achieve high-efficiency cells (>16%) using a manufacturable process, the cast mc-Si substrate is not the most cost-effective for PV. A major component of mc-Si module fabrication is the wafering of ingots, which results in a kerf loss that can be greater than 50% of the ingot.

3.2 Ribbon silicon: A promising material for cost-effective photovoltaics

Ribbon silicon is a promising alternative material for cost effective Si PV because the production cost of the Si substrate is less than that of wafers from mc-Si cast ingots or CZ boules. In ribbon Si growth, substrates for solar cell fabrication can be grown directly from the melt, eliminating the need for ingot slicing. Ribbon silicon materials have been under development since 1967 and currently five ribbon silicon materials are pursued for photovoltaics. Ribbon Si technologies provide an intermediate path between thin film PV technologies, which have a lower substrate cost and lower cell efficiency, and CZ and mc-Si ingot wafer technologies, which yield slightly higher efficiencies at a higher cost. Table 2 [9] shows a cost breakdown of module fabrication for CZ, directionally solidified mc-Si, and edge-defined film-fed growth (EFG) Si, a ribbon silicon material. The EFG

Table 2. Breakdown of module fabrication cost for a 500 MWp manufacturing scenario using screen-printing technology [9]. A June 30, 1997 exchange rate of 0.886 Euro/USD was applied.

Material	Crystallization	Wafering	Solar Cell Fab.	Module Assembly	Mod. Power	Cost ($/W)
CZ	0.7	0.24	0.13	0.35	85.6	1.42
Directionally solidified mc-Si	0.32	0.25	0.12	0.34	86.9	1.03
EFG ribbon Si	0.32	0	0.12	0.36	81.5	0.80

ribbon silicon growth technique reduces the cost of crystallization and wafering by 44% and 66% when compared to directionally solidified mc-Si and CZ materials. Though the EFG Si module produces slightly less power, the cost advantage achieved in crystallization and wafering still brings the total cost per Watt peak to below $1/Wp for a 500 MW production line.

While ribbon materials offer the potential for cost reduction, challenges that ribbon Si materials face include material quality and throughput. Table 3 [34] shows the defect and impurity levels for ribbon silicon materials and other Si PV materials for comparison. The growth of ribbon Si materials results in high impurity segregation in the melt, C or O incorporation from the crucible, die, and/or supporting materials, and a high dislocation density in the range of 10^5-10^6/cm^2. EFG Si and String Ribbon Si are both grown from graphite crucibles, which results in a high carbon incorporation in the ribbons. Carbon can be a harmful impurity in Si and may form SiC precipitates near grain boundaries in ribbon silicon, increasing grain boundary recombination [35]. Ribbon materials are more susceptible to metal impurity segregation than Czochralski growth because there is a confined interface-melt volume without forced convection stirring. Impurity segregation in the crucible is particularly troublesome in long growth runs that require melt replenishment. The equilibrium segregation coefficient for most transition metal impurities in Si, k_o, is about 10^{-5} [34]. It has been shown that the effective segregation coefficient during ribbon Si growth, k_{eff}, is between k_o and 10^{-5} for EFG [36], Dendritic Web [34], and String Ribbon [34]. For RGS and Silicon Film, impurity transport away from the interface is inhibited resulting in a $k_{eff} \leq 1$ [34]. The throughput characteristics for the commercial ribbon materials are shown in Table 4, with

a projection of the number for growth furnaces that will be required for 100 MW/year module production [37]. Much effort is underway at the industry level to improve the throughput of ribbon silicon materials, which is expected to lower the capital cost of installed capacity and the direct labor cost. At the same time, improvement of the efficiency of laboratory-scale and manufacturable ribbon silicon solar cells, shown in Table 5, suggests that there is potential for improvement of commercial products based on these materials. The approach that each ribbon technology has taken to balance the tradeoff between throughput and material quality is presented in the following sections.

Table 3. Defect levels and carbon and oxygen impurity levels in commercial Si PV materials [34].

Material	Resistivity (Ω-cm)	Carbon (cm^{-3})	Oxygen (cm^{-3})	Dislocation Density (cm^{-2})
Czochralski	1-3 p-type	0.5-2.5 $x10^{17}$	0.1-2$x10^{18}$	500
Directionally solidified mc-Si	1.5 p-type	<5$x10^{17}$	<2.5$x10^{17}$	1$x10^{5}$
Thin film a-Si	intrinsic	10^{16}-10^{18}	10^{16}-10^{18}	--
EFG	2-4 p-type	10^{18}	<5$x10^{16}$	10^{5}-10^{6}
String Ribbon	1-3 p-type	4$x10^{17}$	<5$x10^{16}$	5$x10^{5}$
Dendritic Web	5-30 n-type	Not detected	10^{18}	10^{4}-10^{5}

Table 4. Comparison of furnace performance for commercial ribbon Si growth technologies [37].

Method	Pull Speed (cm/s)	Width (cm)	Thickness (μm)	Throughput (cm^2/min)	Furnaces per 100 MW
EFG	1.65	10	250-350	165	100
String Ribbon	1-2	5-8	100-300	5-16	1175
Dendritic Web	1-2	5-8	75-150	5-16	2000
RGS	600-1000	12.5	250-350	7,500-12,500	2-3

Table 5. Ribbon Si solar cell efficiency for cells made using laboratory-scale, manufacturable, and commercial processes.

Ribbon	Laboratory scale cell efficiency (%)	Manufacturable cell efficiency (%)	Commercial cell efficiency (%)
EFG	18.2	15.9	14
String Ribbon	17.8	15.9	13.7
Dendritic Web	17.3	14.5	13-15
Silicon Film	16.6	--	--
RGS	12.5	10.1	--

3.2.1 Edge-defined film-fed grown Si

The edge-defined film-fed growth (EFG) technique was first developed by Labelle and Mvalasky of Tyco Labs. in 1965 to grow crystalline ribbons of sapphire and then silicon. In 1974, Tyco Labs. joined Mobil to form Mobil Solar Energy Company to commercialize EFG Si for photovoltaics. Today EFG Si is the most technologically mature silicon ribbon and is in full commercial production by RWE-Schott Solar with an annual capacity expected to reach 20-25 MW by 2004 [38] in Billerica, MA with additional capacity installed in Alzenau, Germany. In the EFG growth process shown in Figure 13 [34], an octagon-shaped capillary graphite die is lowered into the Si melt. Liquid Si rises to the top of the die and is contacted by a Si seed crystal. The liquid spreads across the surface of the die as the seed is pulled upward, and freezes on the solid

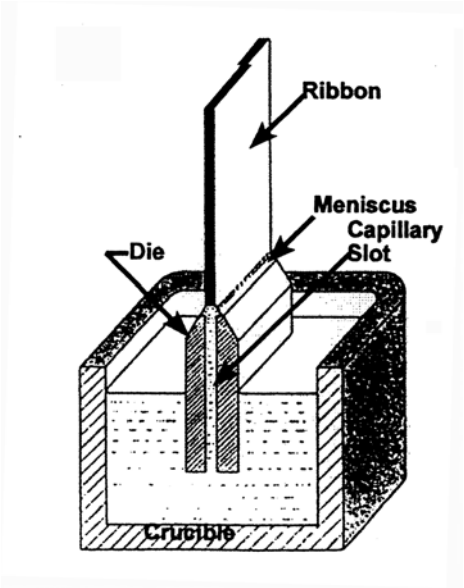

Figure 13. Growth of silicon by the edge-defined film fed growth (EFG) technique [34].

seed. More liquid Si is drawn into the die as the seed is withdrawn so that the growth process may continue. Currently, octagon-shaped tubes with 10 cm sides are grown to a height of 5.4 m with an average wall thickness of 300 μm with continuous melt replenishment. The growth rate of EFG is 1.65 cm/s resulting in a throughput of 165 cm^2/min of ribbon Si as shown in Table 4 [37]. The threat of contamination during EFG growth is high due to direct contact between the large surface of the graphite die and molten Si. Dies also suffer from erosion and must be replaced before ribbon thickness becomes non-uniform. After growth, 10 cm x 10 cm wafers are cut from the octagon shaped tube using a laser scribe. It should be noted that this laser scribing process introduces microcracks near the edges of EFG wafers that requires a Si etch step to improve wafer yield during solar cell manufacturing. Although the use of the die to grow the octagon shaped crystals has increased the throughput of 300 μm EFG ribbon, coupling between temperature and capillary variables creates difficulty in the growth of thin octagon shaped EFG ribbons. In spite of the high defect density in EFG, Georgia Tech reported an cell efficiency of 18.2% using laboratory scale processing including photolithography defined, metal evaporated contacts in 2003 [39]. Georgia Tech also reported the highest efficiency manufacturable EFG cell in 2003 with an efficiency of 16.1% [40]. Today, the average EFG production cell efficiency at RWE-Schott Solar is 14%.

3.2.2 Dendritic Web Si

Dendritic Web growth was developed originally developed by Seidensticker of Westinghouse Electric Corp. in 1962 for GaAs crystals and adapted by Dermatis and Faust, also of Westinghouse Electric Corp., in 1967 for Si crystal growth. Dendritic Web Si modules are in production at Ebara Solar Inc. with an annual production capacity of one megawatt in 2002. The growth of Dendritic Web Si proceeds directly from the melt without the need for foreign support materials as illustrated in Figure 14 [34]. Growth is initiated when a dendrite seed makes contact with the supercooled melt, and spreads laterally to form a button. The button is pulled from the melt at a rate of one to two cm/min. and two dendrite arms grow into the supercooled melt to support a film of molten silicon between them. The molten silicon between the dendrites solidifies into (111) oriented Si with a thickness of about 100 μm. The width of the ribbon is controlled by the separation of the supporting dendrites [34] and can be maintained at 6 cm resulting in a growth rate of 10 cm^2/min. However, precise temperature of the melt control within a few tenths of a degree is vital for uninterrupted growth [37]. After growth, the dendrites are cut from the edges of the ribbon and can be recycled. Though Dendritic Web is essentially a single crystal material, there are twin boundaries oriented parallel to the ribbon surface and a dislocation density of 10^{14}-10^{15}/cm^2. Georgia Tech reported the highest efficiency Dendritic Web solar cell with an efficiency of 17.3% in 1996 using laboratory scale processes [41] and 14.5% using manufacturable processing technologies [42]. Commercial Dendritic Web cells are based on the PhosTop technology with

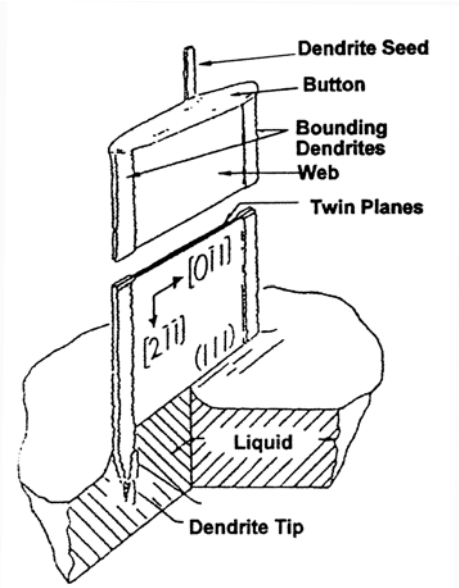

Figure 14. Growth of Dendritic Web silicon

efficiencies in the range of 13-15% and feature an n-type Dendritic Web substrate, Al-doped p^+ emitter, and P-diffused front surface field and [43].

3.2.3 Ribbon growth on substrate

The concept for ribbon growth on substrate (RGS) was introduced by Bleil in 1969 and Si ribbon growth by the RGS technique was developed in 1990. Currently RGS growth is in developmental phases at ECN with support from Deutsche Solar. Research in RGS growth is focused on reducing costs by pulling ribbons at a rate of 600 cm/min. with a throughput of 7,500 cm^2/min [44]. This high pull speed is achievable because growth proceeds from an inclined, wedge-shaped solid liquid interface in which the crystallization and crystal pulling direction are perpendicular as illustrated in Figure 15 [44]. The wedge-shape solid-liquid interface increases the crystallization rate by allowing efficient extraction of the latent heat of solidification during ribbon growth. In

RGS growth, the wedge-shaped melt interface is achieved by placing a shaping die, which contains the melt and defines the width of the ribbon, on a moving substrate. As the substrate is pulled, the Si melt solidifies forming a ribbon adhering to the substrate with a thickness of 250-350 μm. RGS ribbons are characterized by columnar grains comparable to the ribbon thickness oriented perpendicular to the ribbon surface. RGS silicon has a higher density of defects compared to vertically grown ribbon and leads to a very low carrier lifetime of 0.4 μs and a low J_{sc}. Implementing remote-plasma hydrogen passivation and mechanical V-texturing, the University of Konstanz was able to achieve cell efficiencies as high as 12.5% on RGS Si. RGS cell efficiencies as high as 10.1% have been achieved using an industrial type screen-printing process [44]. While progress has been impressive, the very low as-grown lifetime continues to limit cell performance, making RGS non-competitive with conventional ribbon silicon materials.

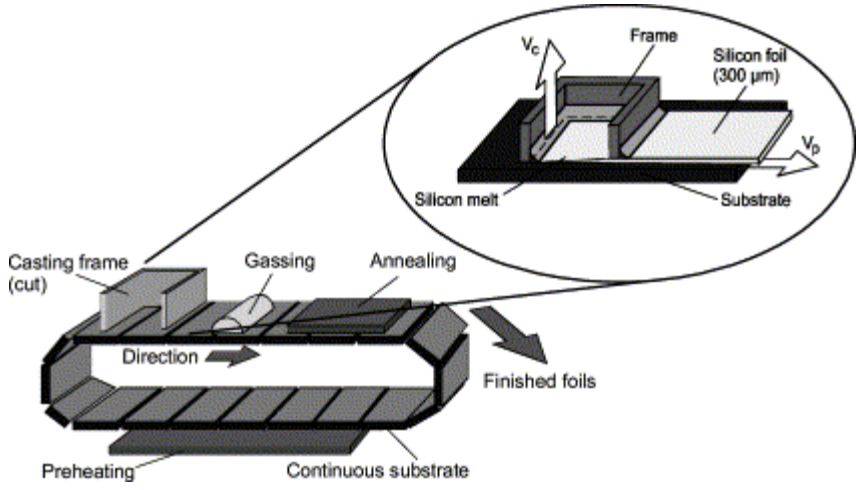

Figure 15. Horizontal growth of RGS silicon on conveyer belt. Insert shows a large wedge-shape crystallization front [44].

3.2.4 Silicon-Film

Silicon-Film was developed by Barnett at the University of Delaware in 1984 and bears more resemblance to thin film deposition rather than the above silicon ribbon growth technologies. The Silicon-Film technology is under development at AstroPower, Inc. under the trade name APex^{TM}, where much of the material growth and solar cell fabrication technology is guarded. AstroPower, Inc. has developed a growth machine capable of producing 15 MW of 200 mm-wide sheet material per year [45]. Like RGS, Silicon-Film is a horizontal growth technique that is supported by a foreign substrate such as steel or quartz and is performed at 800°C-1000°C [46]. As a result, high growth rates are achievable and are expected to enable high-throughput manufacturing. Before Silicon-Film growth, the substrate is coated with a metallurgical barrier layer such as SiC to prevent contamination of the Silicon-Film by impurities in the substrate. Silicon-Film is a saturated solution based growth process similar to liquid phase epitaxy [47]. The growth process is initiated by solution wetting of the substrate, followed by nucleation of crystals, non-impinging crystal growth, and finally film crystal growth. In spite of the SiC barrier coating, the growth substrate is an obvious source of contamination. In fact, Fe, W, Al, Mo, and Ti have been found in the Silicon Film at high levels. However, impurity concentration has not correlated with bulk lifetime, possibly due to impurity segregation near C precipitates that show high recombination strength. The potential of the Silicon Film material has been demonstrated by a 1-cm^2, laboratory-scale solar cell with an efficiency of 16.6% [48]. Limited published data show that the efficiency of commercial solar cells made on the Silicon Film material is as high as 80% that of

Czochralski Si solar cells due to the presence of defects and a high level of impurity contamination [45].

3.2.4 String Ribbon Si

String Ribbon Si was originally developed by the Sachs of MIT and given the name edge-stabilized ribbon (ESR). Evergreen Solar Inc. introduced commercial production of String Ribbon Si modules in 1994 and today, has an installed annual capacity of 3 MW. The growth of String Ribbon Si is uniquely equipped to meet the challenges of thin, high-throughput ribbon growth with low stress and for this reason String Ribbon is the focus of this research. The key component of the growth of String Ribbon Si is the use of two strings composed of a refractory material that define the width of the ribbon and provide edge stabilization. The growth of String Ribbon Si, illustrated in Figure 16, proceeds directly from the melt and is supported by the two strings, which are fed through a graphite crucible containing molten Si [49]. Molten Si wets the strings as they pass through the crucible. The strings support the meniscus and the ribbon and provide edge stability by relaxing the temperature control requirement in the melt to 5°C, greater than that for EFG or Dendritic Web [50]. String Ribbon growth has incorporated tunable afterheaters to modify the cooling profile and avoid the thermal stress produced by a thermal gradient of 500°C/cm near the melt-solid interface [49]. The tunable afterheater has allowed for an increase of the growth speed by 50% and has facilitated the growth of 100 μm thick ribbons with low stress [49]. The thickness of the ribbon is controlled by the pull rate, surface tension, and heat loss from the sheet. Careful control of the growth has allowed ribbon thickness as low as 5 μm to be grown, though the material was stressed and buckled. The theoretical limit to the growth rate is 7 cm/min, but the

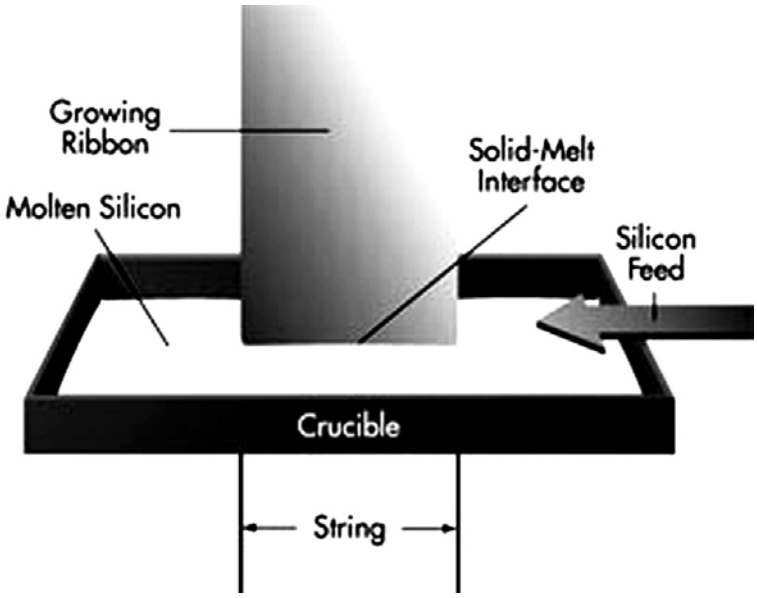

Figure 16. Growth of String Ribbon Si [49].

practical limit is one to three cm/min to prevent fracture of buckling of the ribbon [37]. After ribbon growth, 8 cm x 15 cm wafers are cut using a specially developed laser that does not create microcracks in the wafers and eliminates the need for post-growth damage removal. The strings on the edges of String Ribbon Si serve as a nucleation site for grains with high angle grain boundaries that propagate about 2 mm into the wafer. The central regions of the ribbon consist of millimeter or centimeter size grains that extend for many centimeters along the growth direction [50]. These large grains contain coherent twins along <112> directions in the (111) plane and have an average dislocation density of 5 x 10^5 cm/s found in dislocation loops, networks, and uniformly distributed slip dislocations [51]. To improve the throughput of String Ribbon Si growth, Evergreen Solar has

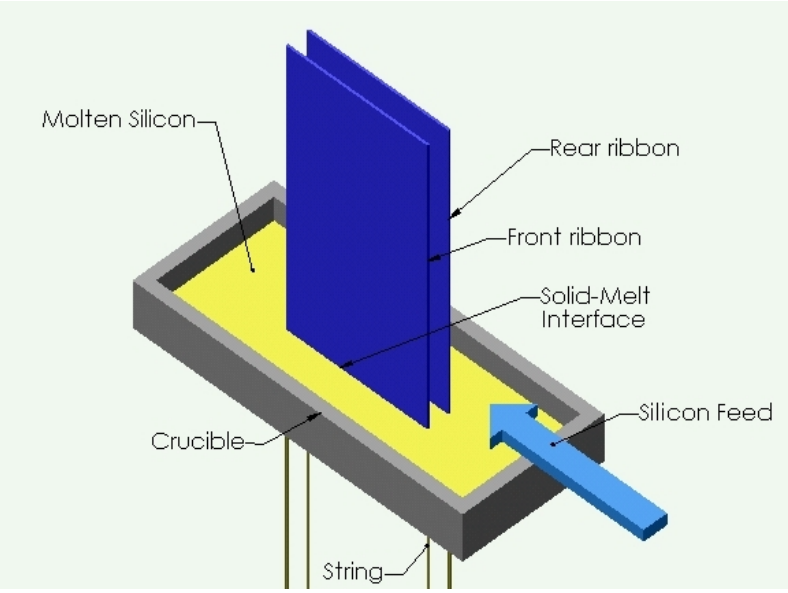

Figure 17. Simultaneous growth of two ribbons of String Ribbon Si by the Gemini technique, currently in production at Evergreen Solar. Image courtesy of Evergreen Solar.

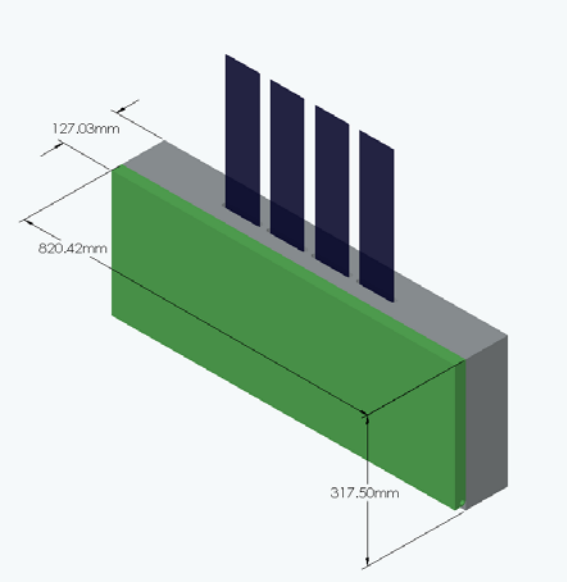

Figure 18. Simultaneous growth of four ribbons of String Ribbon Si by the Quad method, currently in under development at Evergreen Solar. Image courtesy of Evergreen Solar.

developed a technique for multiple ribbon growth termed Gemini and illustrated in Figure 17. In the Gemini technique, two ribbons are grown back to back from one crucible at a rate of 2.5 cm/min and a width of 8 cm. Evergreen Solar has several Gemini furnaces in operation and expects the Gemini technique to reduce consumable costs for ribbon growth by nearly a factor of two while boosting production to 10-14 MW per year by 2004 [52]. Evergreen Solar is also perusing the so-called Quad method, shown in Figure 18, for further cost reduction and throughput enhancement. While this technique is still under development, it has been demonstrated on a ribbon growth machine utilizing an extremely narrow crucible with a width of only 2 cm. Current estimates are that the Quad technique will reduce the number of furnaces needed for a 100 MW factory by about 60% [52]. In 2003, Georgia Tech reported the highest efficiency String Ribbon solar cell with an efficiency of 17.8% using laboratory scale processes and 15.9% using manufacturable processing technologies as a part of this research. Commercial String Ribbon solar cells have an average efficiency of 12.3-12.6% [53].

3.3 A roadmap for high-efficiency ribbon silicon solar cells

While the growth of String Ribbon silicon makes it an attractive material for low-cost silicon photovoltaics, crystallographic defects and impurities limit the as-grown minority carrier lifetime in the material to one to ten microseconds. To assess the impact of the as-grown lifetime on solar cell performance, simulations shown, in Figure 19, were performed using PC1D [54], a one-dimensional solar cell simulation program, with the inputs in Table 6. The simulation inputs include a 300 μm thick 3 Ω-cm p-type substrate,

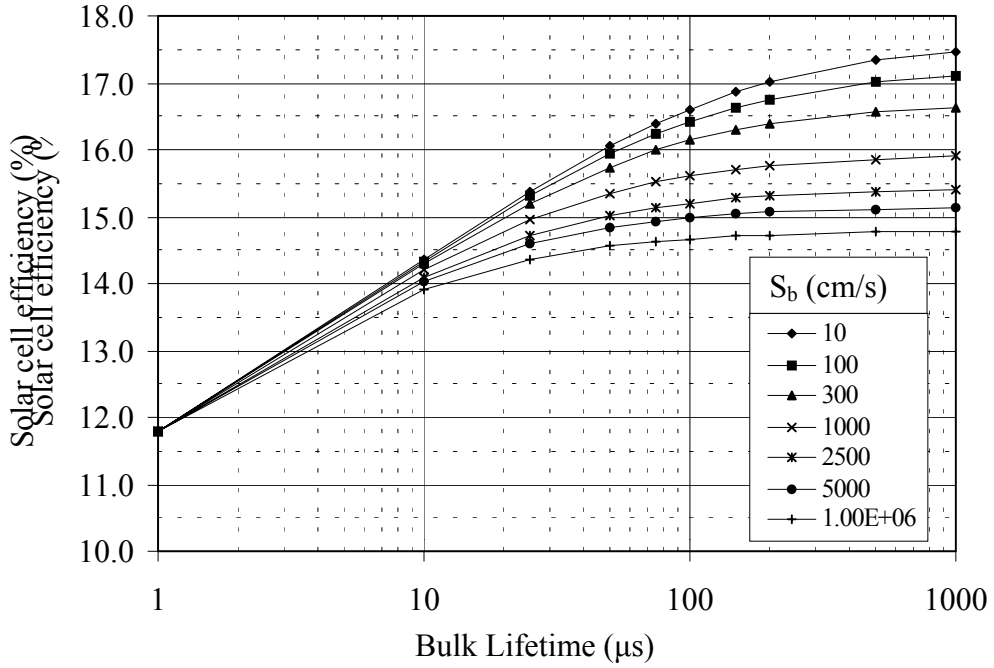

Figure 19. Effect of bulk lifetime and back surface recombination velocity (S_b) on the efficiency of a 300 μm thick, 3 Ω-cm, p-type solar cell.

Table 6. Input parameters for solar cell simulation shown in Figure 19.

Solar cell parameter	*PC1D* input
Base resistivity	3 Ω-cm
Thickness	300 μm
Emitter doping	40 Ω/sq., erfc
Front surface recombination velocity	35,000 cm/s
R_{shunt}	10,000 Ω-cm^2
R_{series}	0.8 Ω-cm^2
J_{o2}	1 x 10^{-8} A/cm^2
Front gird coverage	7%
Anti-reflection coating	n = 2.03 , t = 78 nm
R_b	90% diffuse

a well-passivated 40 Ω/sq. emitter, high-quality electrical contacts resulting in a FF of 0.78, front contact coverage of 7 %, and a single–layer ARC. The results of the simulations indicate that the as-grown lifetime in String Ribbon silicon is not suitable for >16% efficient screen-printed solar cells. However, cell efficiency will increase sharply to 14.4% to 15.4% as the lifetime increases to 25 μs at which point, the back surface recombination velocity, S_b, begins to significantly impact solar cell efficiency. If the lifetime is enhanced further to 150 μs, the simulation indicates that cell efficiencies of 15.0% to 16.6% can be achieved if S_b is in the range of 5000 cm/s to 100 cm/s. It is important to note that there is a marginal benefit of lifetime enhancement after 50 μs for cells in which $S_b \geq 1000$ cm/s, and the 16% efficiency level cannot be reached in these cells. High-efficiency cells can be achieved if the bulk lifetime is in excess of 75 μs, and S_b is less than or equal to 300 cm/s. Therefore, in order to achieve high efficiency ribbon silicon solar cell efficiencies, the first priority is to develop impurity gettering and defect passivation techniques that can improve the minority carrier lifetime to over 75 μs. In the next section, impurity gettering and defect passivation techniques will be reviewed in order to design the appropriate treatments to enhance the lifetime in ribbon silicon.

3.4 Gettering and passivation of defects and impurities

Several techniques have been developed to improve the carrier lifetime in mc-Si, including hydrogen passivation of defects and phosphorus and aluminum gettering of impurities. The best material lifetime enhancement techniques are those that can be performed during solar cell fabrication steps without adding to the cell processing cost. Phosphorus diffusion and aluminum alloying already play an important role in silicon

solar cell processing through the formation of the P-doped n^+ emitter and Al-doped back surface field. Thus, P and Al gettering can be performed during solar cell fabrication. In this section, the mechanisms of P and Al gettering of impurities will be described. Hydrogen passivation of defects has also been demonstrated in silicon solar cells and is attractive because it can be performed at low temperatures. Hydrogen can be incorporated in the solar cell during the deposition and anneal of SiN_x:H films by PECVD. SiN_x:H films are also used in a solar cell for anti-reflection coating and surface passivation. A review of hydrogen passivation of deep levels is presented in this section along with the diffusion and solubility of hydrogen in silicon.

3.4.1 Al and P gettering of impurities in silicon

Gettering is the process of extracting impurities from active regions of the device and localizing them in inactive region. The impurity gettering process involves the release of impurities from the device region, the diffusion of impurities away from the active device region, and the capture of the impurities in the inactive device region. Phosphorus gettering is facilitated by the formation of extended defects around SiP precipitates in heavily phosphorus-doped regions. The extended defects around the SiP precipitates act as sinks for metallic impurities. In addition, silicon self-interstitials are formed during the growth of SiP. These self-interstitials play an important role in the kick-out mechanism, in which substitutional impurities such as gold exchange lattice position with self-interstitials and diffuse rapidly through interstitial sites. Aluminum gettering is driven by the segregation coefficient of metal impurities in the liquid aluminum alloy. Impurities are incorporated in the Al alloy or the BSF region after solidification. Phosphorus and aluminum induced gettering have proven to be effective

gettering treatments, resulting in increase in the minority carrier diffusion length in the base region of the solar cell. Phosphorus and aluminum gettering require no additional processing steps and result in the incorporation of impurities in heavily doped regions of the solar cell where Shockley-Read Hall recombination has little influence on the minority carrier lifetime. Phosphorus gettering can be performed during phosphorus emitter diffusion and Al gettering can be performed during Al-BSF formation.

The release of impurities from device region and their diffusion to inactive device regions is a thermally activated process. As a result, effective phosphorus and aluminum gettering treatments must be performed at temperatures in the range of 800-1000°C for several hours. The gettering of impurities that segregated at dislocations or in precipitates in the bulk of the device can be even more difficult. Simulations by Tan et al. in Figure 20 [55] show the variation in normalized lifetime in Si with Al gettering

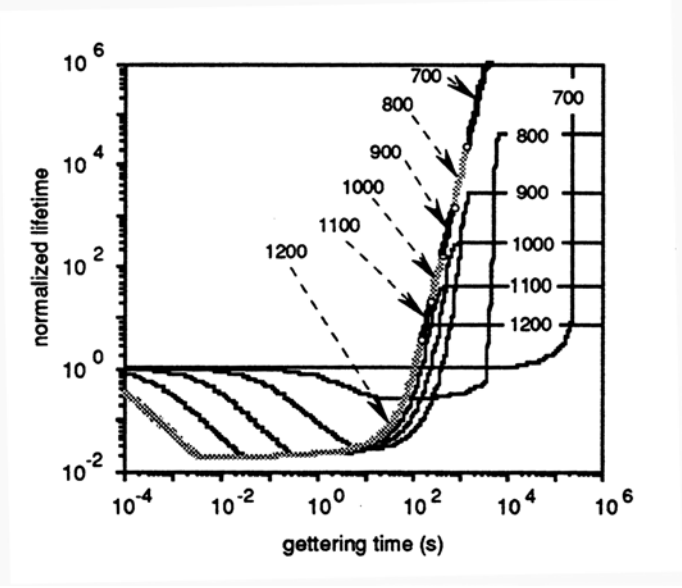

Figure 20. Change in the normalized lifetime during Al gettering in the presence of Fe precipitates. Initial decrease in lifetime is due to an increase in Fe_i during Fe precipitate dissolution [55].

time in the presence of precipitated iron. When gettering temperature is above 700°C, the lifetime decreases due to the dissolution of Fe precipitates and an increase in the Fe_i concentration in the bulk, which act as recombination centers. Only when the gettering time is increased to $>10^3$ s and the iron precipitates have been dissolved does lifetime begin to increase because of gettering of iron at the back surface. This example shows that gettering techniques performed at high temperatures can be complex in the presence of precipitated metals whose dissolution can reduce lifetime, unless the dissolved impurities are gettering out of the bulk into the surface regions.

3.4.2 Hydrogen passivation of defects and impurities in silicon

Hydrogen passivation of deep level defects and impurities in silicon solar cells is technologically viable because hydrogen is present during many device processing steps including deionized water rinse, contact annealing, plasma etching, and thin film deposition. Compared to impurity gettering treatments, hydrogenation of defects can be performed at low temperatures (400°C) for short times because of the high diffusivity of atomic hydrogen in Si. Low temperature hydrogenation processes avoid the interaction of defects with impurities and precipitates that complicate high temperature gettering steps. De Kock et al. at Bell Labs were the first to observe the hydrogen passivation of defects in Si in 1975 [56]. They found that hydrogen introduced during growth decreased the electrical activity of swirl defects in single crystal Si. In 1976, Seager and Ginely found that exposure of polycrystalline Si to atomic hydrogen plasma passivated grain boundaries in the material [57]. Still there were no reports of hydrogen passivation of defects in crystalline silicon solar cells until 1982 when Hanoka of Mobil Solar sent EFG Si samples to Sandia National Laboratories for H passivation from a Kaufman ion source.

Their electron beam induced current images showed that H passivated grain boundaries and enhanced solar cell efficiency by more than 1% absolute in EFG silicon [58].

3.4.2.1 Hydrogen passivation of deep levels in Si

Hydrogenation treatments of silicon solar cells are targeted at the passivation of dangling bond defects found at external surfaces, certain metal impurities, grain boundaries, and dislocations. Dangling bond centers in Si give rise to levels in the forbidden gap that serve as intermediate states for electron hole pair recombination. The bonding of hydrogen to a Si dangling bond forms an electrically inactive bonding state in the valence band and an electrically inactive anti-bonding state in the conduction band. Hydrogen passivation has proven to be effective in reducing the recombination activity of many crystalline defects in silicon including swirl defects [56] and grain boundaries [57] to depths of 200 μm [58]. Hydrogen also passivates many deep energy levels introduced by the isolated metal impurities and metal complexes, though the exact mechanism for passivation is not well understood. Generally, it is believed that hydrogen passivation of metal impurities renders the impurity electrically inactive by forming a stable impurity-H bond or by rearranging the defect structure [59]. An example of hydrogen passivation of a metal impurity is illustrated in Figure 21 [60], which shows the DLTS peak due to a Au-donor level in p-type Si before (Figure 21 (a)) [60] and after hydrogen passivation from a plasma source (Figure 21 (c)) [60]. The peak amplitude or defect concentration decreases significantly after exposure to atomic hydrogen from the plasma source at 300°C. Figure 21 (b) [60] shows that hydrogen passivation during an anneal in H_2 at 300°C was unable to passivate Au because molecular hydrogen is not the species responsible for defect passivation. Table 7 [59] lists the metal impurities that can and

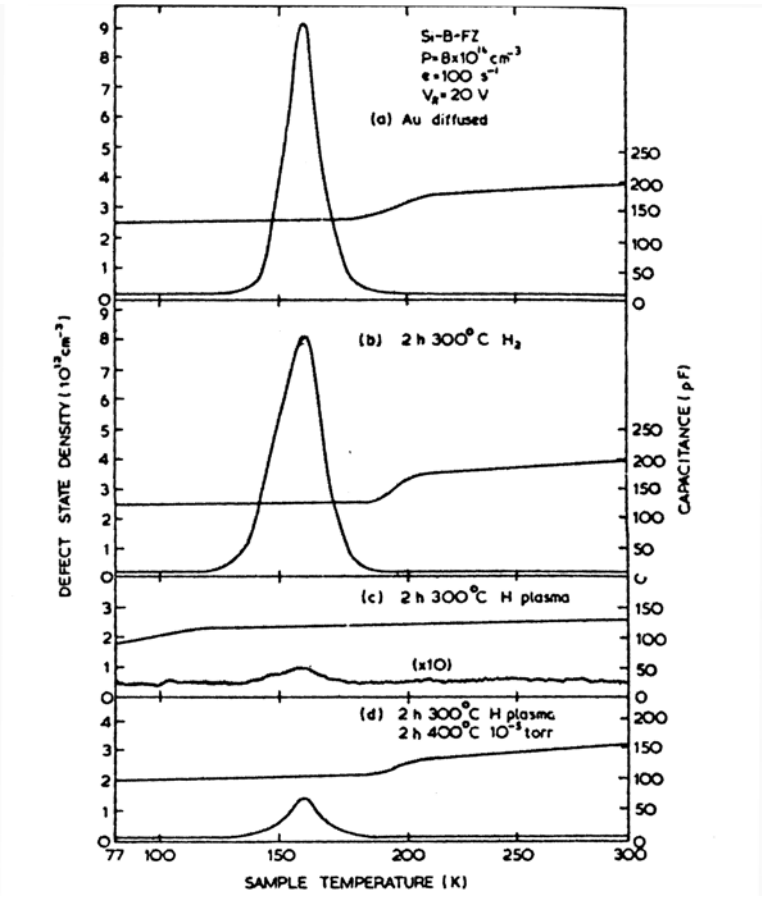

Figure 21. Capacitance transient spectra from Au-diffused p-type Si showing (a) electrically active Au-donor level; (b) no H passivation after anneal H_2 for 2 hours at 300°C; (c) passivation of Au during H plasma exposure for 2 hours at 300°C; (d) partial reactivation of Au-donor level after vaccum anneal at 400°C for 2 hours [60].

Table 7. Metal impurities that can be passivated by hydrogen and their reactivation energy [59].

	Metal	Defect level	Reactivation Energy (eV)
Metal impurities passivated by atomic hydrogen	Au	E_v+0.35 eV E_c-0.54 eV	2.3
	Ag	E_v+0.29 eV E_c-0.54 eV	2.2
	Pd	E_v+0.32 eV E_c-0.22 eV	2.4
	Cu complexes	E_v+0.20 eV E_c+0.35 eV E_v+0.53eV	2.5
	Ni complexes	E_v+0.18 eV E_v+0.21 eV E_v+0.33 eV	2.5
	Cr	E_v+0.30 eV	
	quenched Fe	E_v+0.30 eV	1.5
	diffused Fe	E_v+0.32 eV	1.5
Metal impurities not passivated by atomic hydrogen	Fe_i	E_v+0.40 eV	
	Ti	E_v+0.31 eV	
	V	E_c-0.50 eV	

cannot be passivated by hydrogen. The most notable level that cannot be passivated is Fe_i, which is a known "lifetime-killer" in Si. Therefore, if Fe_i is the lifetime limiting defect in silicon, phosphorus or aluminum gettering must be performed first before hydrogen passivation can provide lifetime enhancement.

Figure 21 (d) [60] shows that annealing of hydrogen passivated Au at 400°C in a vacuum causes partial reactivation of the donor level, demonstrating that hydrogen passivation of defects is not thermally stable. The activation energy for H dissociation from the defect-hydrogen bond is dependent on the temperature of the anneal as shown in (21) [61].

$$\boldsymbol{E_D = kT} \ln\left[\frac{\mathbf{1}}{\tau\upsilon} \ln\left(\frac{\boldsymbol{N_o}}{\boldsymbol{N}}\right)\right] \tag{21}$$

where τ is the anneal time, ν is the dissociation frequency, N_o is the initial density of defect-hydrogen complexes, and N is the density of defect-hydrogen complexes after annealing. The activation energy for H dissociation for many metal impurities is given in Table 7 [58]. It has been shown that prolonged annealing (>20 min) of hydrogenated Si samples breaks the Si-H bond when the anneal temperature is above 500°C [62] and has an activation every of 2.0-2.5 eV. The thermal instability of the hydrogen passivation makes hydrogen retention an important issue, during as well as after the hydrogenation process. All of the heat treatments must be designed for maximum hydrogen retention during solar cell processing.

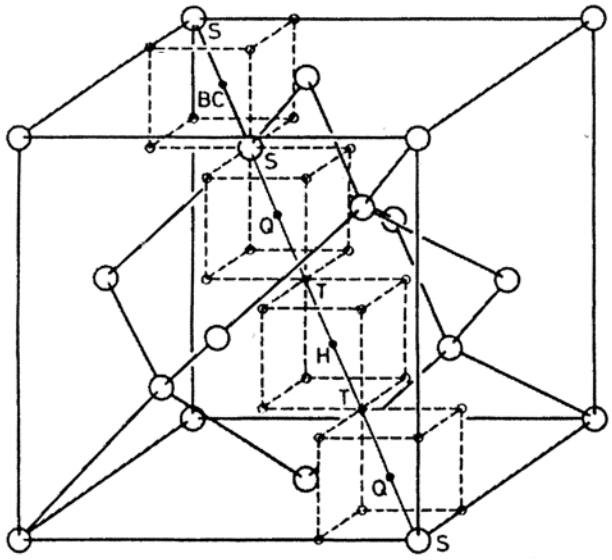

Figure 22. Unit cell of Si illustrating the substitutional site (S), bond center site (BC), antibonding site (Q), tetrahedral interstitial site (T), hexagonal interstitial site [63].

3.4.2.2 Solubility and diffusivity of hydrogen in silicon

Hydrogen exists in both the molecular (H_2) and atomic (H) form in silicon, though only H contributes to defect passivation [59]. Isolated H_2 is the most stable state of hydrogen in silicon at low temperatures and occupies the tetrahedral interstitial site (T) in Si shown in Figure 22 [64]. H can be found in three charge states: neutral (H^0), positively charged (H^+), or negatively charged (H^-). The charge state of hydrogen can change through electron exchange with the Fermi level [64]. As a result, the charge state depends on the location of the Fermi level. H^- and H^+ are the dominant forms of hydrogen in n- and p-type Si respectively. Both H^0 and H^+ are found in the bond center

(BC) site, shown in Figure 22. The additional electron diminishes tendency for H^- to interact with host atoms and causes H^- to maximize its distance from host atoms, positioning it in the T site [64].

Van Wieringen and Warmoltz have determined the solubility of hydrogen in silicon over the temperature range of 970°C to 1200°C given by [65]

$$S_H = 2.4x10^{21} \exp\left(\frac{-1.88ev}{kT}\right)[cm^{-3}] \qquad (22)$$

Extrapolation of (19) to 300°C yields a value of 10^5 cm^{-3}. Ichimiya and Furuichi [66] showed that the low temperature (400°C-500°C) solubility could be significantly higher than predicted by (19), and found a low temperature solubility of $2x10^7$ cm^{-3} at 300°C. However, neither finding considers the effect of hydrogen trapping at defects that can control hydrogen incorporation. It has been shown that dislocations can enhance the solubility of hydrogen in Si at 800°C by three orders of magnitude [67].

The high diffusivity of hydrogen in Si enables low-temperature hydrogenation treatments to be effective throughout the thickness of a solar cell. The diffusivity of hydrogen in silicon as measured by Van Wieringen and Warmoltz (VWW) for temperatures in the range of 970-1200°C, and often extrapolated to lower temperatures, is [65]

$$D_H = 9,4x10^{-3} \exp\left(-\frac{0.48eV}{kT}\right) cm^2 s^{-1} \qquad (23)$$

Figure 23 shows a calculation of the depth to which hydrogen will diffuse at 740°C based on the VWW diffusivity and the $d=(Dt)^{-1/2}$ relation. Astonishingly, hydrogen can diffuse

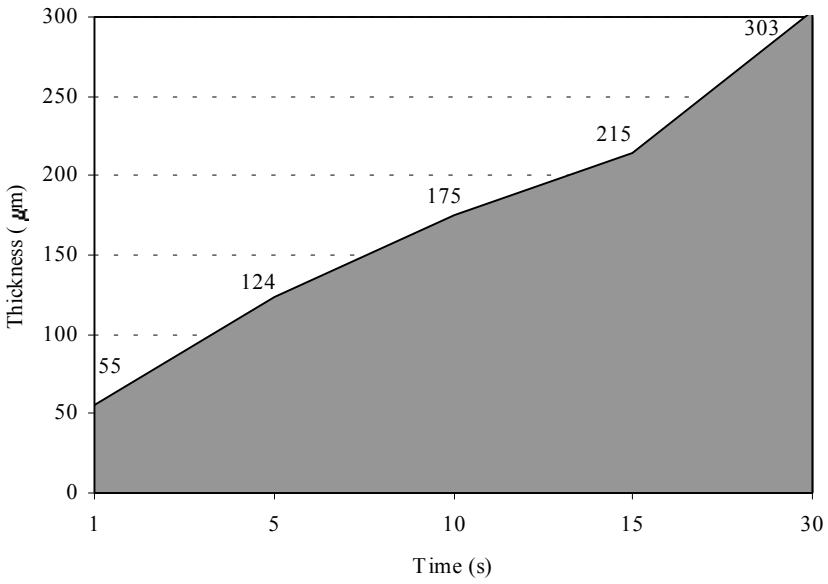

Figure 23. Calculation of the depth of hydrogen diffusion as a function of anneal time at 740°C based on VWW diffusivity. Hydrogen diffuses through the wafer thickness in only 30 s.

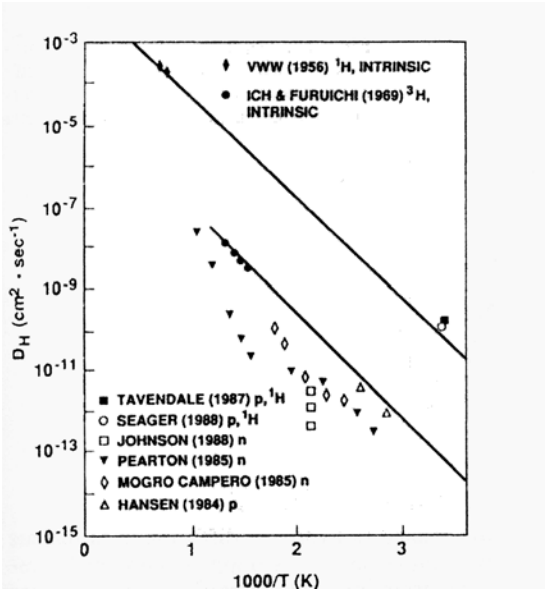

Figure 24. Comparison of experimentally measured H diffusivities in Si. Low temperature diffusivity deviates from extrapolation of VWW relation due to H_2 molecule formation and H trapping [59].

through the entire thickness of a conventional silicon solar cell in only 30s! However, experimental measurements of hydrogen diffusion at lower temperatures have found lower hydrogen diffusivity, as shown in Figure 24 [59] explained by two effects. First, at low temperatures, the bonded forms of hydrogen (H_2 and Si-H) are dominant. The activation energy for diffusion of H_2 in Si is 2.7 eV making H much more mobile than H_2, as illustrated by the ratio of their respective diffusion coefficients in Table 8 [68]. Further impeding the transport of hydrogen at low temperatures is the trapping of hydrogen by ionized acceptors and other defects. At high temperatures, the bonded forms dissociate and H dominates, increasing effective diffusivity of hydrogen. At temperatures greater than 300°C, most of the diffusion is by H^0, which is not trapped by ionized acceptors. Additionally slower hydrogen diffusion in n-type Si, has been attributed to molecule formation [69].

Table 8. Ratio of the diffusion coefficients for H and H_2 at various temperatures [68].

Temperature (K)	D_H/D_{H_2}
300	1.2×10^{42}
500	1.8×10^{25}
750	6.8×10^{16}
1000	4.3×10^{12}
1250	1.3×10^{10}
1500	2.6×10^{8}

Table 9. Distribution of H_2 and H in Si [68].

Total Hydrogen Content (cm^{-3})	$[H_2]/[H]$ at 300 K	Temp. at which $[H_2]/[H] = 1$ (°C)
1.5×10^{14}	1.6×10^{9}	626
1.5×10^{15}	5×10^{9}	748
1.5×10^{16}	1.6×10^{10}	892
1.5×10^{17}	5×10^{10}	1075

Table 9 [68] shows the relative amounts of molecular and atomic hydrogen in silicon at room temperature and the temperature at which H_2 and H are in equal concentration. At room temperature H_2 outnumbers H by a factor of 1.6×10^{9} - 5×10^{10}. Even at 748°C, typical for solar cells processing, the concentration of H_2 is equal to that of H when the total hydrogen content is 1.5×10^{15} cm^{-3}. The presence of H_2 in Si in high concentrations indicates that molecule dissociation into H is needed to provide more effective defect passivation. Recent molecular dynamics calculations have shown that hydrogen reacts with point defects in silicon. While H_2 is stable in crystalline silicon, H_2 spontaneously dissociates when placed inside a vacancy cluster, releasing 4.0 eV according the following equation [70]

$$V + H_2 \rightarrow \{V, H, H\} + 4.0\,eV. \tag{24}$$

The release of 4.0 eV is associated with the formation of Si-H bonds and the reduction of the strain associated with the original defect. This reaction predicts that when rapidly diffusing V's encounter interstitial H_2, they will dissociate the molecule. At temperatures

above about 500 K, the interaction can release two H interstitials and the energy released can be kinetic, allowing H to escape the defect and diffuse independently.

Experimental observation of the diffusion profile of H in Si has been unsuccessful due to the low mass of hydrogen and the presence of H residue in the sample chamber. Therefore, hydrogen diffusion profiles in Si are inferred from deuterium diffusion profiles measured by SIMS. Deuterium shows no chemical difference to hydrogen, but its diffusion coefficient is lower by a factor of $2^{-1/2}$ due to the difference in mass between deuterium and hydrogen. Figure 25 [71] shows that surface damage produced by mechanical polishing enhances the deuterium profile in EFG Si. The enhanced diffusion profile is believed to be the result of the spontaneous dissociation of H_2 by vacancies generated by surface damage as predicted by (24). Other factors that increase the

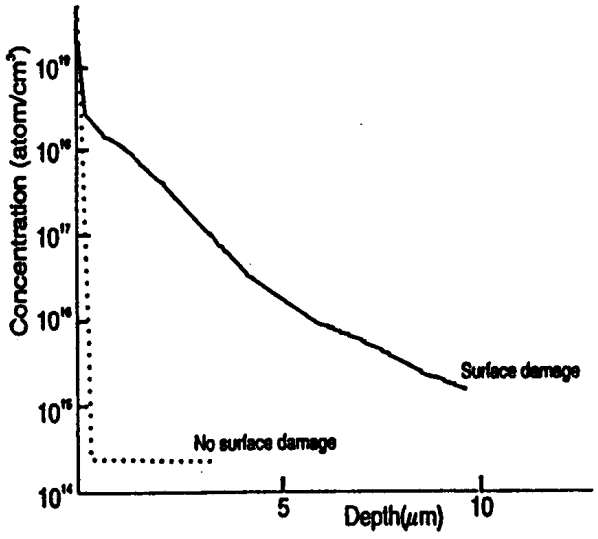

Figure 25. Enhancement of the deuterium profile in edge-defined film-fed grown Si due to surface damage measured by SIMS [71].

vacancy concentration include high growth speed and high carbon concentration [72] and are also expected to enhance the diffusion of hydrogen and incorporation of hydrogen in silicon. In addition, a higher penetration depth for deuterium during plasma annealing has been found in low oxygen content silicon ribbon [73]. This observation suggests that hydrogen should diffuse rapidly in String Ribbon silicon, which has a reasonably high growth rate, high carbon content, low oxygen content, grain boundaries and dislocations.

3.4.2.3 Hydrogen passivation of defects in Si through the anneal of PECVD SiN_x:H films

Incorporation of hydrogen in Si has been achieved by many methods including exposure to H_2 gas during crystal growth, hydrogen ion beam bombardment, hydrogen plasma exposure, annealing in forming gas, and the deposition and anneal of PECVD SiN_x:H films applied to the surfaces of Si wafers. Unfortunately, most of the hydrogenation techniques developed in the 1970s were not compatible with high–volume, high-throughput solar cell manufacturing. Hydrogen passivation by ion beam bombardment is performed on individual samples at a base pressure of 1×10^{-5} Torr before the chamber is back filled with hydrogen gas, making this process non-manufacturable [74]. Hydrogen passivation by low temperature hydrogen plasma anneal [75,76,77,78] or forming gas anneal (5-10% H_2) [79] has improved the performance of low-cost Si solar cells, but requires treatments of 30-240 minutes.

The concern about the manufacturability of hydrogenation were erased in 1982 when Morita et al. [80] of Toshiba showed that simple and rapid deposition of SiN_x:H films by PECVD enhances the grain boundary photoresponse in cast mc-Si wafers. Subsequently, SiN_x:H films have proven to be suitable for AR coatings and provide surface passivation.

More recently, comparative studies performed at IMEC have shown a 1.6% absolute cell efficiency enhancement when a PECVD SiN_x:H film is used in some mc-Si solar cells [81]. The efficiency enhancement is due to the multiple performance enhancing features that SiN_x:H films offer for solar cells including bulk defect passivation, surface defect passivation, and an anti-reflection coating.

An RF-induced plasma is used during the deposition of SiN_x:H by PECVD, to transfer energy to the reactant gases allowing film deposition at low temperatures (<500°C) with high deposition rates (~20 nm/min). SiN_x:H films are deposited by the reaction of dissociated, ionized, and excited species of SiH_4 and NH_3, created by electron impact in the plasma. In the case of N-rich silicon nitride, an ammoniosilane precursor ($Si(NH_2)_{n\leq4}$ is adsorbed on the surface as a result of the following reaction [82]

$$SiH_4 + 4NH_3 \rightarrow Si(NH_2)_4 + 4H_2 \quad (25)$$

On the surface of the growing film, the ammonia gas desorbs from the ammoniosilane precursor as follows [81]

$$Si(NH_2)_4 \rightarrow Si_3N_4 + 8NH_3 \quad (26)$$

Because of the presence of hydrogen in SiH_4 and NH_3, there is a substantial amount of hydrogen in Si-H and N-H bonds of SiN_x:H that is detectable by Fourier transform infrared spectroscopy (FTIR). The bonded hydrogen content in SiN_x:H has been found to be as high as 2×10^{22} cm^{-3}, about 75% of which is bound to Si [83]. A higher deposition temperature promotes NH_3 evolution and reduces the content of bonded nitrogen and hydrogen [82]. Hydrogen evolves from SiN_x:H films during thermal treatment above

400°C and is marked by a decrease in the area under the Si-H and N-H peaks in the SiN_x:H FTIR spectrum.

Two common PECVD reactors are the conventional parallel plate reactor and the horizontal tube reactor. Both types of reactors are investigated in this research. In the radial parallel plate reactor, RF power is typically delivered at a frequency of 13.56 MHz to the upper electrode, while the bottom electrode on which the samples are placed, is grounded. These reactors can be heated to temperatures up to 300-400°C and operated at pressures in the range of 0.1 to 5 Torr. Introducing and removing gases either from the periphery/center or center/periphery achieves radial flow of reactant gases. Throughput is an issue for parallel plate reactors and no more than four 100 mm wafers can be coated in one run with a batch time of 15 minutes, including a five-minute temperature stabilization period. For this reason, parallel plate reactors are only useful for laboratory-

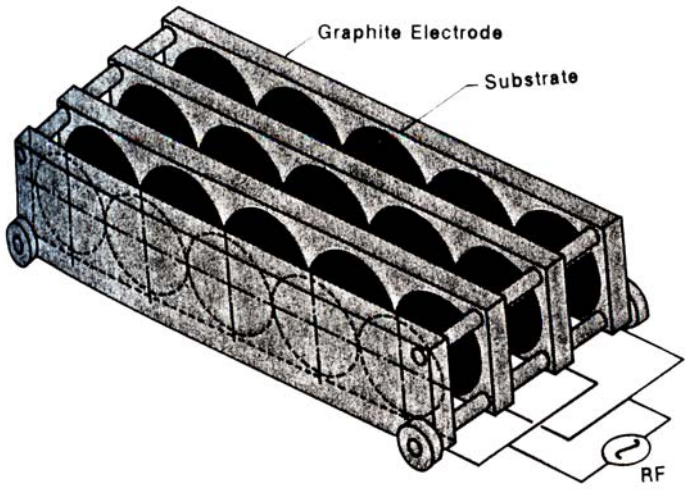

Figure 26. Graphite boat that serves as the substrate holder and electrodes in a horizontal tube PECVD reactor [84].

scale studies for photovoltaics and are not found in commercial solar cell manufacturing lines. In horizontal tube PECVD reactors, samples are loaded on specially designed boats with vertically or horizontally oriented graphite plates as shown in Figure 26 [84]. The plates are stacked parallel to one another with alternate plates serving as ground and power while the plasma is generated between them with an excitation frequency in the range of 50 to 450 kHz. The boat also consists of electrical contacts to connect the plates to an RF power supply and wheels to aid the loading on unloading of the boat from a radially heated quartz tube. Horizontal tube reactors have a higher throughput than parallel plate reactors and can coat 120, 100 mm wafers in one run with a batch time of 40 minutes, including 20 minutes for temperature stabilization. Thus PECVD SiN_x:H films may be deposited using a low frequency (50-450 kHz) or high frequency (13.56 MHz) plasma excitation. The average ion energies in low frequency plasma deposition are higher than those found in a high frequency plasma deposition and leads to hydrogen implantation and damage to the Si surface. The SiN_x:H-induced hydrogen passivation is particularly effective in a "fire-through" process in which the Ag and Al electrodes are screen-printed onto the Si substrate after SiN_x:H film deposition. During a subsequent contact sintering anneal, hydrogen is released from the SiN_x:H film and is available for the passivation of defects in the Si substrate. A model for H diffusion has been proposed by Sopori et al. [85] to incorporate process-induced traps for H created by plasma damage. In this model, H is stored in traps near the surface after SiN_x:H film deposition. H is freed from the traps states during a post-deposition anneal when the de-trapping rate exceeds the trapping rate.

CHAPTER 4

Development of an Al-enhanced, Silicon Nitride-induced Low-cost Bulk Defect Hydrogen Passivation Treatment

While the growth of String Ribbon Si makes it an attractive material for low-cost silicon photovoltaics, the as-grown minority carrier lifetime in the material is typically 1-10 μs. The results of the solar cell simulations shown in Chapter 3 clearly indicate that, for a 300 μm device, the as-grown lifetime in String Ribbon silicon is not suitable for high-efficiency (>16%) screen-printed solar cells, and there is only a small impact of back surface passivation. However, the simulations in Figure 19 indicate that the cell efficiency will increase sharply to 15.3 % as the lifetime increases from 1 μs to 25 μs, followed by slow but gradual enhancement in efficiency up to 16.9 % for a lifetime of 150 μs and S_b=100 cm/s. Therefore, to fabricate high-efficiency screen-printed devices on String Ribbon Si, impurity gettering and defect passivation techniques that can improve the minority carrier lifetime in the material without significantly raising the cost must be developed and understood. The aim of this phase of the study is to raise the

lifetime in String Ribbon Si to at least 25 μs using manufacturable impurity gettering and defect passivation techniques. In Chapter 3, it was shown that the gettering of impurities could improve the lifetime if gettering is performed at high temperatures. However, Figure 3-8 showed that prolonged gettering (one hour) is required to enable the dissolution of metallic precipitates. Unfortunately, solar cell manufacturers cannot afford lengthy, energy intensive processing steps that limit the throughput necessary for low-cost manufacturing. Therefore, the rapid and manufacturable gettering techniques that are employed in this study include phosphorus gettering using a liquid spin-on dopant, and Al gettering using a screen-printed Al layer. The heat treatments are performed in an industrial-type belt furnace. The effectiveness of the gettering treatments is evaluated by lifetime measurements before and after each treatment using the QSSPC technique described in Chapter 2. It was also shown in Chapter 3 that hydrogen passivation could be performed at low temperatures for short times due to the high diffusivity of hydrogen in Si. During solar cell manufacturing, hydrogen in available for defect passivation during PECVD SiN_x:H film deposition and subsequent anneal. In this study, hydrogen passivation of defects in String Ribbon Si is investigated using a PECVD SiN_x:H film as the source of hydrogen followed by heat treatment in a belt furnace to drive hydrogen into the substrate. In Chapter 3 it was shown that hydrogen can interact with point defects in Si indicating that there may be synergistic interactions during solar cell processing steps that introduce point defects, altering the effectiveness of hydrogenation from SiN_x:H. For this reason, the effectiveness of PECVD SiN_x:H hydrogenation individually and in combination with phosphorus and Al gettering in String Ribbon silicon is evaluated in this chapter. To investigate the release of hydrogen from PECVD

SiN_x:H films and subsequent passivation defects in String Ribbon Si, a combination of FTIR measurements of PECVD SiN_x:H films and QSSPC bulk minority carrier lifetime measurements are used.

4.1 Minority carrier lifetime enhancement from P and Al gettering of String Ribbon Si

Phosphorus and aluminum gettering are often performed in a conventional tube furnace and their gettering mechanisms have been reviewed in Chapter 3. The phosphorus gettering treatment investigated in this section involves the application of a liquid spin-on dopant followed by an anneal in a belt furnace. Prior to dopant application, samples were cleaned using the series of solutions shown in Appendix A. After spin-on dopant application, substrates were dried at 200°C for two minutes on a hotplate and annealed in a lamp-heated belt furnace (*Radiant Technology Corp. LA-310*) for six minutes in air at a set-point temperature of 925°C to obtain the target sheet resistance of 45 Ω/sq. After diffusion, the phosphorus-doped glass layer was etched in dilute HF and substrates were again cleaned. Al gettering was performed using a thick film of Al screen printed to the back surface of String Ribbon substrates using a commercially available Al paste (*Ferro FX 53-038*). Then substrates were dried on a hotplate for two minutes at 200°C and annealed in a belt furnace for two minutes in air at a set-point temperature of 850°C. After heat treatment, the Al layer and underlying p^+ Al-doped layer were removed by chemical etching. All substrates were cleaned prior to the post-process lifetime measurement. Lifetime measurements were made using the QSSPC

technique with samples immersed in a solution of 70 mg of I_2 in 250 mL of methanol. Lifetime values were recorded at an injection level of 1 x 10^{15} cm^{-3} to avoid recording erroneously high recombination lifetimes at lower injection levels caused by shallow traps [29]. Four lifetime measurements were made at different locations on each ~4 in^2 sample and the mean lifetime value was used to characterize the bulk lifetime of the entire substrate.

Figure 27 shows that the lifetime improvement in String Ribbon Si after the rapid and manufacturable P and Al gettering treatments. The short P gettering alone at 925°C was only able to increase the lifetime from 8.5 μs to 10.5 μs and Al gettering performed at 850°C for two minutes raised the lifetime to 18.3 μs from 9.7 μs. The lifetime improvement provided by individual P and Al gettering treatments does not meet the initial minimum target of 25 μs, hence additional lifetime enhancement is required.

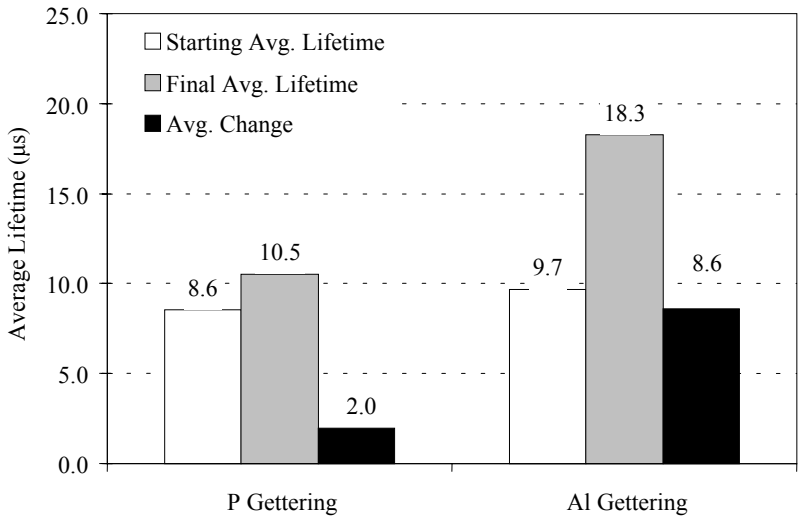

Figure 27. Effectiveness of P and Al gettering and treatments.

However, the lifetime improvements achieved by the individual gettering steps are noteworthy considering that the P gettering step also forms the n^+-emitter compatible with current screen-printed solar cells, and the Al gettering step forms an effective Al-doped BSF at no additional cost.

4.2 Lifetime enhancement due to hydrogen passivation of defects in String Ribbon Si from the anneal of a high-frequency PECVD SiN_x:H film

PECVD SiN_x:H films deposited at 200°C -300°C have a hydrogen concentration between 1.3 x 10^{22} and 2.0 x 10^{22} cm^{-3} [86], and have been shown to provide efficient bulk and surface hydrogen passivation when annealed [87,79]. Many studies claim that the release of hydrogen from the PECVD SiN_x:H film into the silicon substrate and subsequent passivation of bulk defects during thermal anneal is responsible for enhancement in multicrystalline Si (mc-Si) solar cell performance [79, 88-92]. In this section, the release of hydrogen from a PECVD SiN_x:H film during anneal in a belt furnace is measured by FTIR. Subsequently the release of hydrogen is correlated with the increase in lifetime in String Ribbon.

4.2.1 Temperature dependence of the release of hydrogen from PECVD SiN_x:H films

SiN_x:H films were deposited on the front surface of float zone Si wafers for FTIR analysis of the hydrogen content in PECVD SiN_x:H films. SiN_x:H films were deposited

at 300°C using a direct, parallel plate PECVD reactor operating at 13.56 MHz with a flow rate of 320 and 1.55 sccm for SiH_4 (2% in N_2) and NH_3 respectively. The SiN_x:H films had a thickness of 860 Å and a refractive index of 1.94. After SiN_x:H deposition, selected float zone Si samples were annealed in a tube furnace at 400°C in forming gas (10% H_2 in N_2) and in a belt furnace with set-point temperatures of 730°C and 850°C in air. The actual wafer temperature for these belt furnace heat treatments is revealed in Appendix B. Room temperature FTIR measurement and analysis was performed on each float zone Si sample after the heat treatments.

The FTIR spectra in Figure 28 show that upon post-deposition anneal of the PECVD SiN_x:H film, the bonded hydrogen content in the film, proportional to the total area under

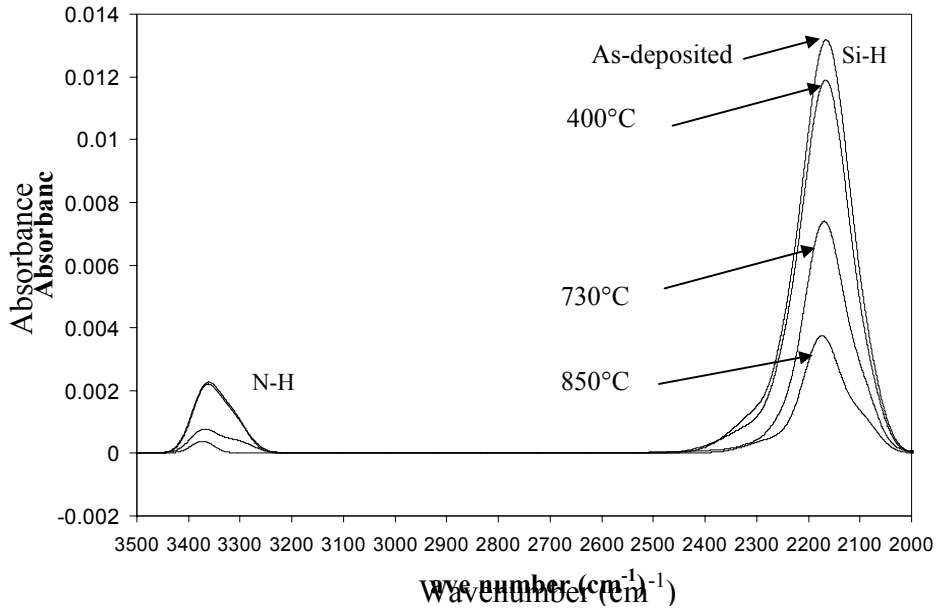

Figure 28. FTIR spectrum of PECVD SiN_x:H films after post-deposition anneals.

the Si-H and N-H peaks, decreases as the anneal temperature is increased. Calculation of the bonded hydrogen content was performed using the methodology shown in Ref. 83. The total bonded hydrogen content in the as-deposited high-frequency (13.56 MHz) PECVD SiN_x:H film was found to be $2.7x10^{22}$ cm^{-3} which decreased by a factor of 4.3, 2.1, and 1.2 for the 850°C, 730°C, and 400°C anneals respectively. This indicates that more hydrogen is released from the film as the anneal temperature is increased. If the degree of defect passivation depends only on the release of hydrogen from the SiN_x:H film, one would expect the passivation effect to increase as the anneal temperature is increased. However, this is not the case as shown in the next section.

4.2.2 Effect of the release of hydrogen from SiN_x:H on lifetime enhancement

To establish the effect of the release of hydrogen from SiN_x:H on defect passivation in the underlying String Ribbon substrate, the lifetime of String Ribbon substrates were measured after post-deposition anneal in the belt furnace. Because there is some variability in the as-grown lifetime in various String Ribbon samples, the average of four lifetime measurements, taken on different regions of each sample, was measured before and after the passivation treatments in this section. SiN_x:H films were deposited on both sides of String Ribbon samples using the process described in Section 4.2.1 and annealed at temperatures in the range of 600°C - 850°C. Figure 29 illustrates the effect of the post-deposition anneal temperature on the bulk passivation of String Ribbon samples with and without SiN_x:H. Samples coated with SiN_x:H had an average as-grown lifetime of 13.2 μs, while samples without SiN_x:H had an average as-grown lifetime of 3.2 μs. Due to the variability in the as-grown lifetime of String Ribbon samples, the relative change in

lifetime (τ_{final} - $\tau_{as\text{-}grown}/\tau_{as\text{-}grown}$ x 100) that results from PECVD SiN_x:H-induced hydrogenation is plotted in Figure 29 as a function of the post-deposition anneal temperature. For all anneal temperatures investigated, the relative change in lifetime for samples annealed without SiN_x:H is small with respect to the change in lifetime for samples annealed with SiN_x:H. Therefore, the difference between the two curves in Figure 29 is attributed to SiN_x:H-induced hydrogen passivation of bulk defects. The lifetime measurements in Figure 29 indicate that with SiN_x:H, defect passivation increases as the post-deposition anneal temperature approaches 725°C commensurate with the decrease in the bonded hydrogen content in the SiN_x:H film with temperature shown in Figure 28. This result supports the hypothesis that the degree of hydrogen passivation is dependent on the amount of hydrogen released from the SiN_x:H film up to

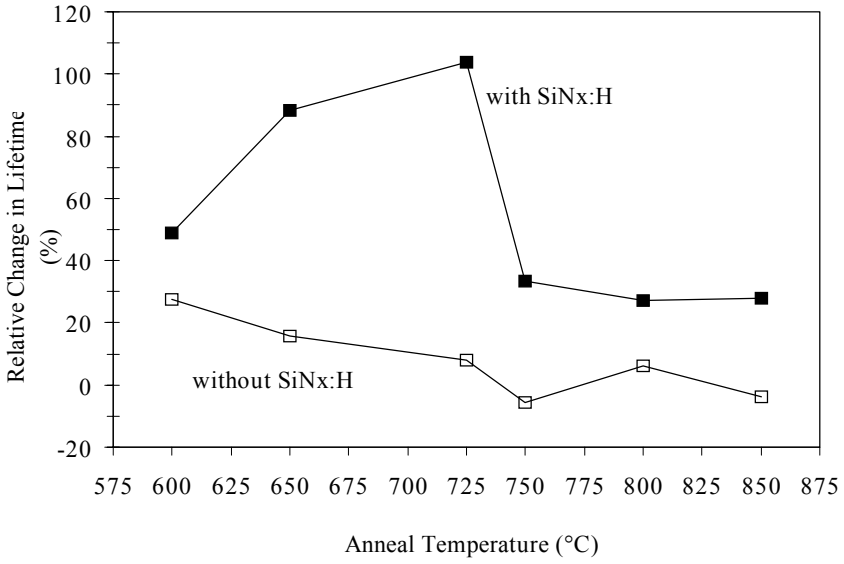

Figure 29. Defect passivation from post-deposition anneal of PECVD SiN_x:H.

725°C. However, the hypothesis fails above 725°C because of desorption of hydrogen from defects, as discussed in the next section.

4.2.3 Competition between the release of hydrogen from the SiN_x:H film and the retention of hydrogen at defects

Figure 29 shows that at anneal temperatures between 600°C and 725°C, the relative improvement in lifetime is greater than 50%, while in the temperature range of 750°C-850°C, the relative improvement drops to near 30%. It should be noted that the degree of defect passivation from the anneal of SiN_x:H films, without prior Al or phosphorus treatments, is highly material dependent due to the variety of defects in different Si PV materials [93, 94]. The dramatic decrease in the effectiveness of hydrogen passivation above 725°C may be due to the high temperature instability of hydrogen at defect sites in silicon. Since hydrogen is known to diffuse out of silicon above 500°C during prolonged anneals [62], SiN_x:H-induced hydrogenation may be governed by the thermal budget (time and temperature) of the post-deposition anneal. The degree of hydrogen passivation of silicon defects should be proportional to the release of hydrogen from the SiN_x:H film and the out diffusion of hydrogen from the defect during the anneal cycle as well as the retention of hydrogen at defect sites in silicon.

4.3 Al enhanced SiN_x:H-induced hydrogenation of defects

To further enhance the lifetime of String Ribbon Si and investigate the interaction of the hydrogenation process with phosphorus and Al gettering, combinations of phosphorus and Al gettering with SiN_x:H hydrogenation using a 850°C post-deposition anneal were

investigated. Though Figure 29 indicates that there is little bulk passivation from the SiN_x:H post-deposition at 850°C, this anneal temperature was chosen so that Al gettering, the formation of a high quality Al-BSF, and defect hydrogenation can be simultaneously. The lifetime enhancement provided by various combinations of P and Al gettering and

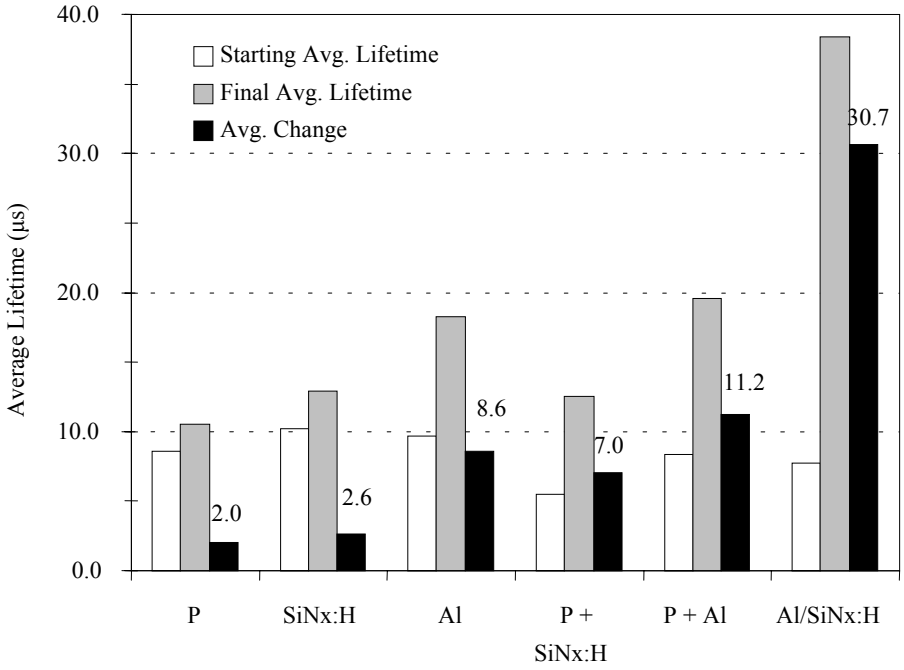

Figure 30. Effectiveness of the combination of gettering and hydrogen passivation treatments.

SiN_x:H-induced hydrogen are shown in Figure 30 along with the effect of individual treatments. The combination of phosphorus gettering and SiN_x:H hydrogenation at 850°C improves the lifetime by 7 µs, which is nearly equal to the sum of the enhancement provided by individual phosphorus gettering and hydrogenation treatments. A similar additive effect is observed in the combination of phosphorus and Al gettering in

which the lifetime improved by 11 μs. Still the 25 μs threshold is not exceeded by any of the above combinations. In contrast, a noteworthy average lifetime of 38 μs, an improvement of 30 μs, is observed when the PECVD SiN_x:H hydrogenation treatment and Al gettering treatment are combined in one heat treatment at 850°C for two minutes. This improvement in lifetime is far greater than the sum of the 850°C SiN_x:H hydrogenation and Al treatments alone, suggesting that there may be a positive synergistic interaction between the hydrogenation from the front surface and the Al alloying process occurring simultaneously at the back surface of the substrate.

4.4 Proposed model for the Al enhanced hydrogenation of defects

The above gettering and passivation study indicates that SiN_x:H-induced hydrogenation of String Ribbon Si is most effective when it occurs simultaneously with backside Al alloying. A three step physical model, illustrated in Figure 31, is proposed to describe the observed Al alloying-aided hydrogenation based on recent theoretical calculations of hydrogen and vacancy interactions and the solubility of hydrogen in the Al-Si melt. The results in Figure 28 and Figure 29 showed that hydrogen released from the SiN_x:H film passivates defects in String Ribbon silicon during a post-deposition anneal at temperatures below 725°C when anneal time is two minutes. This is depicted in Figure 31 (a). The data in Figure 31 also indicated that during higher temperature anneals (>725°C), the retention of hydrogen at defect sites in String Ribbon Si must decrease since the SiN_x:H-induced passivation is significantly reduced. This is depicted

in Figure 31 (b). In contrast, as shown in Figure 31 (c), Al-Si alloying can promote hydrogenation of defects by enhancing the dissociation of hydrogen molecules and the migration of atomic hydrogen deep into the bulk Si. Three mechanisms that may contribute to the Al-enhanced hydrogen passivation are the interaction of hydrogen with vacancies generated during Al-Si alloying, the prevention of hydrogen out diffusion by Al, and the segregation to hydrogen toward the Al-Si melt. During the Al-Si alloying, Si is dissolved in the Al melt, generating defects such as voids [95] and vacancies in Si, the latter of which can rapidly diffuse through silicon. These vacancies are now available to participate in the dissociation of molecular hydrogen into rapidly diffusing atomic hydrogen. In a perfect Si lattice, hydrogen is proportioned nearly equally between the molecular and atomic species at high temperatures (> 626°C) [68]. Estreicher's recent ab initio tight binding molecular dynamics calculations have shown that the H_2 molecule is stable in a perfect Si lattice, but disassociates into atomic hydrogen in the presence of vacancies or interstitials [70]. Dissociation is important because atomic hydrogen is more mobile in silicon than the molecular species by a factor of 10^{10} to 10^{12} at 850°C [68] and atomic hydrogen is responsible for defect passivation. Grain boundaries may further assist the diffusion of hydrogen [58], though hydrogen may not be retained at grain boundaries during prolonged annealing at high temperatures. In addition to promoting dissociation, vacancies may also enhance the transport of atomic hydrogen in Si. Theoretical calculations have shown that the binding energy of hydrogen to vacancies (V_n^0) is high, 3 to 3.5 eV greater than the binding energy of hydrogen at the bond center [96]. This affinity of hydrogen to vacancies can increase the flux of hydrogen in silicon.

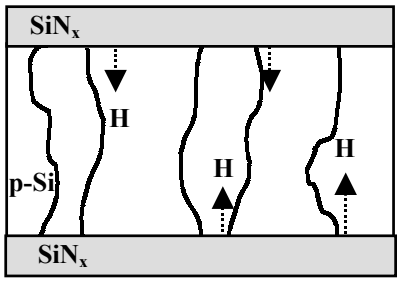

(a)

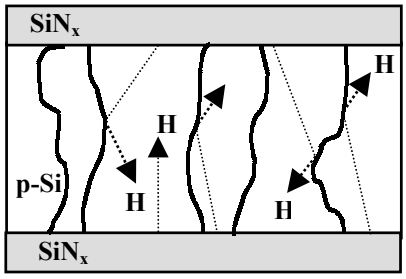

(b)

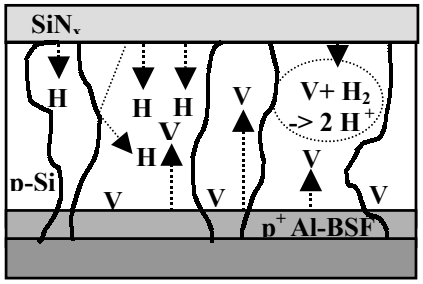

(c)

Figure 31. A schematic representation the of three step model for SiN_x:H-induced defect passivation depicting: (a) the release of hydrogen during SiN_x:H anneal, (b) the retention probability of hydrogen at defects during high temperature SiN_x:H anneal, and (c) vacancy induced dissociation of molecular hydrogen and vacancy and segregation enhanced migration of atomic hydrogen.

The flux of hydrogen atoms can be described in terms of a chemical potential as shown in the equation below [97]

$$J_H = -M_H C_H \frac{\partial \mu_H}{\partial x} \tag{27}$$

where J_H is the flux of hydrogen into the wafer, M_H is the mobility of atomic hydrogen, C_H is the concentration of atomic hydrogen, and μ_H is the chemical potential of atomic hydrogen in the wafer. In the absence of vacancies, the chemical potential gradient is dictated by the concentration gradient. In the presence of vacancies, the attraction of hydrogen to vacancies at the backside of the wafer may increase the chemical potential gradient, and as shown by (27), increasing the flux of hydrogen in the silicon. In this model backside Al alloying generates vacancies, which enhance the dissociation of molecular hydrogen into mobile atomic hydrogen and increase the driving force for the migration of atomic hydrogen in the material, enabling and promoting the passivation of defects deep in the material. At this time, no direct evidence of alloying induced vacancy generation in Si can be provided. Therefore other models SiN_x:H-induced hydrogenation cannot be ruled out.

The high solubility of hydrogen in the Al melt could provide an additional driving force of hydrogen diffusion in Si. The solubility of hydrogen in an Al-Si melt can be determined from the activity and activity coefficient of hydrogen as [98]

$$[wt\%H]^{AlSi(l)} = a_H / f_H \tag{28}$$

where a_H is the activity of hydrogen in the aluminum melt and f_H is the activity coefficient of hydrogen in the Al-Si melt. Equation 29 gives the activity coefficient of hydrogen in an Al-Si melt [98]

$$\log_{10} f_H = e_H^{Si}[wt\%Si] + r_H^{Si}[wt\%Si]^2 \quad (29)$$

where e_H^{Si} and r_H^{Si} are the first and second order interaction coefficients, respectively. The temperature dependence of the interaction coefficients are given by [98]

$$e_H^{Si} = \exp\left(\frac{609.31}{T} - 4.5708\right) \quad (30)$$

$$r_H^{Si} = -9.000\times10^{-7}T + 4.257\times10^{-4} \quad (31)$$

where T is the temperature in K. The activity of hydrogen is equal to its concentration in the pure Al melt. Anyalebechi [99] determined an empirical expression for the temperature dependence of hydrogen solubility in the pure Al melt given by

$$\log_{10}[wt.\%H]^{Al(l)} = \frac{-2691.96}{T} - 1.32 \quad (32)$$

through a combined linear regression analysis of the published enthalpy and entropy data for hydrogen in the pure Al melt. Equations (29) through (32) can be used together to calculate the solubility of hydrogen in an Al-Si melt of any composition. The composition of Si in the melt at 850°C is given by the Al-Si phase diagram and is equal to approximately 30 wt%. Figure 32 shows the calculated of the solubility of hydrogen in

an Al Si melt with 30 wt.% Si based on (25) through (29), the solubility of hydrogen in Si from (33) [65], and the segregation coefficient, k, of hydrogen in the Al-Si melt given by (34).

$$[H]^{Si} = 2.4x10^{21} \exp\left(\frac{-1.88ev}{kT}\right)[cm^{-3}] \tag{33}$$

$$k = [H]^{AlSi(l)} \Big/ [H]^{Si} \tag{34}$$

Figure 32 shows that the solubility of hydrogen in the Al-Si melt is 2.7 x 10^{18} cm^{-3} and the solubility of hydrogen in Si given by is 9.4 x 10^{12} cm^{-3} at 850°C. This results in a segregation coefficient for H in the Al-Si melt of 2.9 x 10^{5}, comparable to that for Co,

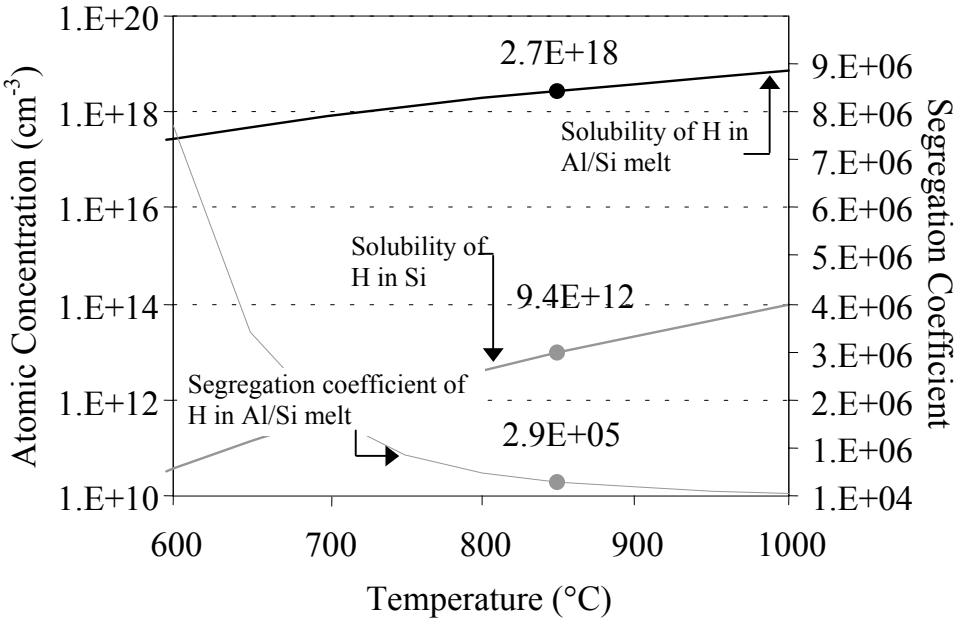

Figure 32. The segregation coefficient of H in the Al-Si melt (30 wt% Si) calculated from the solubility of H in Si and Al-Si melt.

which has a lower bound of 10^4 [100], and Fe, where $k=10^6$ [101]. In Al gettering, the high segregation coefficient for metal impurities in the Al-Si melt provides the driving force for impurity diffusion. The segregation coefficient for Fe has been shown to provide sufficient driving force for the gettering of Fe as deep as 400 μm in Si [101]. If hydrogen transport in Si is analogous to the segregation of transition metal impurities in the Al melt during Al gettering, then the high segregation coefficient of hydrogen in the Al-Si melt provides an additional driving force for the flux of hydrogen deep in Si. Therefore the synergistic effect of SiN_x:H-induced passivation in the presence of Al could result from the interaction of vacancies and hydrogen in Si and the high solubility of hydrogen in the Al-Si melt. Vacancies enable the dissociation of H_2 into highly mobile H and enhance the chemical potential gradient for H in Si. Deep transport of hydrogen in Si may also be promoted by the high segregation coefficient of hydrogen in the Al-Si melt. Al-Si alloying enables hydrogen passivation of defects at high temperatures, even though retention hydrogen to defect sites decreases. In the three step physical model in Figure 31, passivation is dependent on the release of hydrogen from the SiN_x:H film, the retention of hydrogen at defect sites, and the presence of Al on the back of the wafer.

4.5 Conclusions

This study shows that commercially viable gettering and hydrogen passivation treatments investigated in this study are effective in improving the bulk lifetime of String Ribbon silicon substrates. The solar cell simulation in Figure 19 indicates that the lifetime improvement of 30 μs achieved in this chapter should be sufficient for the

fabrication of low-cost, high efficiency (>15%), screen-printed solar cells if S_b is less than 1000 cm/s. The three step physical model proposed in Figure 31 summarizes the results of this study. The model demonstrates that hydrogen defect passivation from PECVD SiN_x during a post-deposition anneals depends on three processes: i) the release of hydrogen from the PECVD SiN_x film; ii) the retention of hydrogen at defect sites in silicon; and iii) Al alloying at the back surface of the wafer. In this chapter, PECVD SiN_x:H films were deposited with a plasma excitation frequency of 13.56 MHz at a temperature of 300°C. FTIR measurements of this film on float zone Si wafers showed that the bonded hydrogen content (Si-H and N-H) in film is $2.7x10^{22}$ cm^{-3} after deposition. After heat treatment, the bonded hydrogen content decreases by a factor of 4.3, 2.1, and 1.2 for the 850°C, 730°C, and 400°C anneals respectively. This indicates that more hydrogen is released from the film as the anneal temperature is increased. When SiN_x:H coated String Ribbon Si samples were annealed for hydrogenation, greater than 50% improvement in the lifetime was observed at anneal temperatures between 600°C and 725°C due to hydrogen passivation of defects. The observed defect passivation is commensurate with the decrease in the hydrogen content in the SiN_x:H film measured by FTIR. When the anneal temperature is increased to 750°C-850°C, the relative improvement drops to near 30% due to the low retention of hydrogen at defects.

When the PECVD SiN_x:H-induced hydrogenation and Al gettering treatments were combined in one heat treatment at 850°C for two minutes, a noteworthy average lifetime improvement of 30 μs was achieved. This improvement in lifetime is far greater than the sum of the SiN_x:H hydrogenation and Al treatments alone suggesting that there may be a positive synergistic interaction between the hydrogenation from the front

surface and the Al alloying process occurring simultaneously at the back surface of the substrate. The synergistic effect of SiN_x:H-induced passivation in the presence of Al could be the result of the interaction of vacancies and hydrogen in Si and the high solubility of hydrogen in the Al-Si melt. As a result, the combination of hydrogenation and Al gettering effectively improved the lifetime in String Ribbon silicon beyond 30 μs even though the retention of hydrogen at defects in silicon is low at high temperatures.

CHAPTER 5

Improved Understanding and Implementation of SiN_x:H-induced Hydrogenation for High-efficiency String Ribbon Solar Cells

In the previous chapter, it was shown that the simultaneous anneal of a screen-printed Al layer on the back and a PECVD SiN_x:H film on the front after phosphorus gettering, can improve the spatially averaged lifetime in String Ribbon to over 30 μs, which is required to achieve >15 % efficient cells. To describe the Al-enhanced SiN_x:H-induced hydrogenation, a physical model was proposed in which defect passivation is governed by the release of hydrogen from the SiN_x:H film, Al-Si alloying on the back of the wafer, and the retention of hydrogen at defect sites. During this anneal, hydrogen is released from the SiN_x:H film and passivates defects in the String Ribbon substrate. The role of Al in this process be could two-fold. First Al-Si alloying generates vacancies in Si that dissociate molecular hydrogen into atomic hydrogen, and may enhance the diffusion of hydrogen in silicon. Second, the formation of an Al-Si melt may promote H transport in Si because of the high segregation coefficient of H in the melt. In this study, two experimental strategies that validate the proposed model are investigated, and lead to the implementation of Al-enhanced hydrogen passivation to fabricate manufacturable String

Ribbon solar cells. To assess the impact of Al on hydrogenation, the effect of Al coverage of the back surface is investigated. A reduction of the Al coverage is of technological importance. While beneficial for lifetime enhancement, full Al rear coverage causes thin (100 μm) String Ribbon Si wafers to bow up to five millimeters during alloying at 850°C. However, the bowing of thin wafers can be avoided by depositing Al in a grid pattern resulting in partial coverage of the back surface. Partial coverage of the rear also permits bifacial solar cell designs where the Si surface between the Al grid may be passivated with by dielectric films. The proposed model for hydrogenation postulates that hydrogen passivation is dependent on the retention of hydrogen during the anneal. This suggests that rapid cooling may improve hydrogen passivation. To further understand the role of hydrogen retention, the impact of improved hydrogen retention by rapid cooling after the hydrogenation anneal is investigated in this study for increased defect passivation. Rapid cooling is achieved in a rapid thermal processing (RTP) system in which cooling rates up to 50°C/s can be realized. The impact of partial Al coverage of the back surface and rapid cooling will be evaluated by QSSPC measurement of the lifetime in String Ribbon Si.

Solar cell fabrication using RTP has been explored to reduce the thermal budget of solar cell processing and hence reduce processing costs. In this study, RTP will be used to implement rapid cooling during solar cell fabrication after screen-printed contact firing to improve the retention of hydrogen in String Ribbon solar cells. It has been shown that firing of screen-printed contacts in an RTP system can result in a contact resistance as low as 10^{-5} Ω-cm^2 [102], though the resulting fill factor (FF) was only 0.724 on multicrystalline silicon, presumably due to junction leakage. Recently, the Design of

Experiment technique has been implemented to optimize a rapid thermal firing (RTF) process resulting in FF as high as 0.782 on Cz Si and 0.774 on multicrystalline Si [103]. However, the influence of rapid cooling during RTF on the bulk defect passivation of mc-Si solar cells, if any, was not identified. In this study, the impact of RTF, with fast heating and cooling rates, performed after the simultaneous Al-BSF formation and SiN_x:H hydrogenation anneal is investigated for improved defect passivation and contact quality in String Ribbon Si solar cells. To assess the impact of RTF on solar cell performance, solar cells are also fabricated with a lamp heated belt furnace contact firing scheme, characterized by slow heating and cooling rates.

5.1 Impact of partial Al coverage on Al-enhanced SiN_x:H-induced defect passivation

The effect of reduced Al area rear coverage on Al-enhanced SiN_x:H-induced hydrogenation is investigated to eliminate bowing of thin wafers while achieving defect passivation. The results of this study also confirm the importance of Al in SiN_x:H-induced hydrogenation. Figure 33 shows the lifetime enhancement as a function of rear Al coverage after SiN_x:H/Al anneal at 850°C/2 min in a belt furnace followed by cooling at a rate of 6°C/s. Samples shown in Figure 33 had a spatially averaged as-grown lifetime in the range of 2.0-3.8 μs. Full coverage (100%) of the rear surface by Al results in an average relative change in lifetime of String Ribbon Si by 219%. This lifetime enhancement is larger than expected based on the exponential fit of the data points in Figure 33. This discrepancy in the lifetime enhancement is likely due to differences in

the as-grown spatially averaged lifetime and the defect distribuition in among the samples of the two experiments. The lifetime enhancement drops dramatically to 80% when the Al area coverage is reduced to 75%, which illustrates the importance of Al in the hydrogenation process. According to the model for Al-enhanced hydrogenation, the reduction in Al coverage reduces the amount of Al-Si alloying and thus the dissociation and migration of atomic hydrogen is reduced. The lifetime enhancement decreases monotonically as the Al coverage decreases from 75% to 0%. While partial Al coverage reduces hydrogenation, 100 μm thick String Ribbon samples do not bow during Al-Si alloying when the Al coverage is reduced to 75% or below.

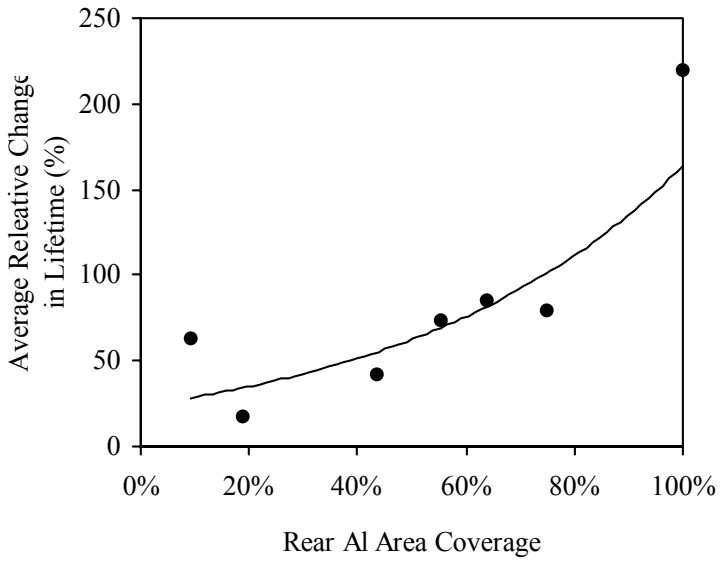

Figure 33. Impact of Al area coverage on Al-enhanced SiN_x-induced hydrogenation at 850°C/2 min with a cooling rate of 6°C/s. The spatially averaged as-grown lifetime was in the range of 2.0-3.8 μs.

5.2 Effect of the cooling rate on SiN_x:H-induced hydrogenation

In this section, the impact of improved hydrogen retention by rapid cooling after the hydrogenation anneal for increased bulk defect passivation is investigated. The spatially averaged relative improvement in the lifetime of String Ribbon samples, with a spatially averaged as-grown lifetime of 2.9 μs, is measured as a function of the cooling rate after the post deposition anneal of the SiN_x:H film with and without Al in a rapid thermal processing (RTP) system. The cooling rate plotted in Figure 34 is determined by measuring the time required for the sample temperature to decrease to 300°C from 850°C (curves (b) and (c)) or 700°C (curve (a)). Figure 34 shows that the spatially averaged relative improvement in lifetime is about 40% for all cooling rates for rapid thermal firing (curve a) performed at 700°C for one second. In this process, the lifetime enhancement is probably limited by the release of hydrogen from the SiN_x:H due to the relatively short, low temperature anneal . When the anneal temperature and time are increased to 850°C and two minutes, the spatially averaged relative change in lifetime increases with the cooling rate after anneal even when no Al is present on the back (curve (b)). This suggests that the ability to retain hydrogen at defect sites in Si can be improved by increasing the cooling rate after the anneal. The spatially averaged relative change in lifetime increases for all cooling rates when Al is present on the back (curve (c)) due to Al-Si alloying. When Al is present on the back, vacancies generated during Al-Si alloying and formation of an Al-Si melt increase the flux of hydrogen in Si, which results in significant defect passivation. Figure 34 also shows that the Al-enhanced hydrogenation process is less sensitive to the cooling rate (curve (c)). The increased flux,

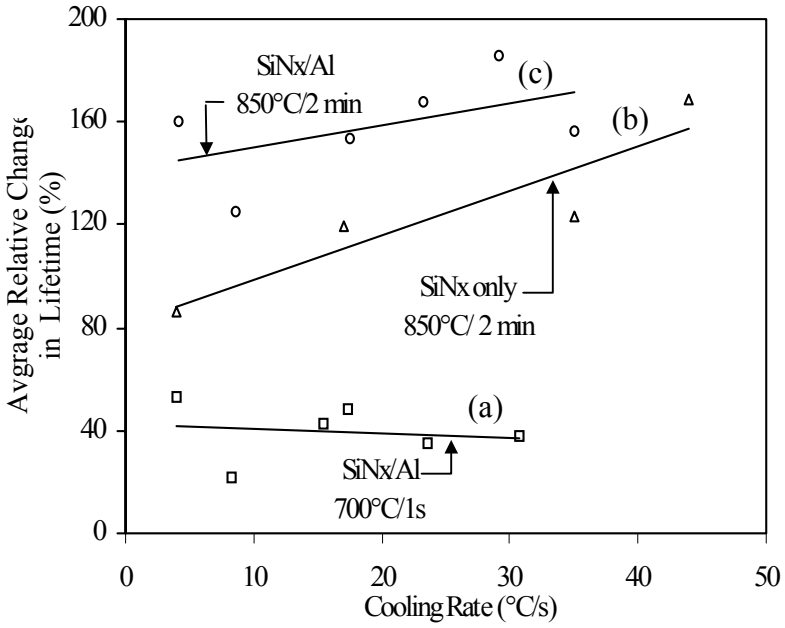

Figure 34. Impact of rapid cooling on SiN_x:H-induced hydrogenation. The spatially averaged as-grown lifetime was 2.9 μs.

or supply, of hydrogen in Si due to Al-Si alloying reduces the dependence of the passivation process on the retention of hydrogen.

5.3 Implementation of SiN_x:H-induced hydrogen passivation to fabricate high-efficiency, manufacturable String Ribbon Si solar cells

In this study, RTF is investigated for improved defect passivation and contact quality in String Ribbon Si solar cells. Solar cell fabrication begins with sample cleaning, described in Appendix A, followed by phosphorus emitter diffusion that is performed at a temperature of ~960°C in a belt furnace using a commercially available spin-on liquid

dopant (*Filmtronics P507-6%*) to achieve a sheet resistance of 35-45 Ω/sq. A SiN_x:H film is deposited on the front surface and serves as an anti-reflective coating (ARC), a surface passivation dielectric, and a source of hydrogen for bulk defect passivation. After SiN_x:H deposition, Al paste (*Ferro53-038*) is screen-printed to the back surface of all samples, baked, and annealed in a belt furnace at a set-point temperature of 850°C for two minutes providing hydrogenation and forming an aluminum back surface field (Al-BSF). A silver paste (*Ferro 3349*) is screen-printed in a grid pattern onto the front surface of all samples and baked. RTF is performed on selected samples at 700°C for one second with a cooling rate of 40°C/s in an RTP system to sinter the Ag contacts. For comparison, Ag sintering is performed on selected samples in a lamp heated belt furnace, with a setpoint temperature of 730°C for 30 seconds and a cooling rate for 4°C/s. During this belt furnace firing the sample temperature reaches a peak temperature of 700°C for 2.7 s. String Ribbon solar cells are analyzed by illuminated IV measurement, light beam induced current (LBIC) mapping of spectral response, and light-biased internal quantum efficiency (IQE) measurements.

5.3.1 Efficiency distribution of String Ribbon solar cells with RTF and belt furnace fired contacts

Figure 35 shows the efficiency distribution of 93 String Ribbon cells with RTF with a cooling rate of 40°C/s or belt furnace contact firing with a cooling rate of 4°C/s. The solar cell efficiencies shown in Figure 35 were measured using a calibrated String Ribbon Si solar cell that was measured at Sandia National Labs. While there is a wide distribution in the cell performance in both schemes, RTF is clearly superior with an average cell efficiency of 13.8%, an improvement of 1.2% absolute higher than

conventional belt furnace contact firing. QSSPC measurement on finished solar cells showed that the lifetime was 25-30 μs after RTF. It has recently been shown by Rohatgi et al. [104] that the performance of EFG Si solar cells improves by 1.4% absolute due to RTF. The highest efficiency cell made with RTF had an efficiency of 14.7%, while the highest efficiency cell made with belt furnace firing had an efficiency of only 13.4%. This difference in efficiency is the result of differences in J_{sc}, V_{oc}, and FF, shown Table 10, indicating that RTF improves the contact quality, minority carrier diffusion length, and possibly the rear surface passivation in String Ribbon devices. The impact of the FF enhancement provided by RTF is illustrated by Figure 36, which shows the FF distribution for 93 String Ribbon solar cells with RTF and belt furnace firing schemes.

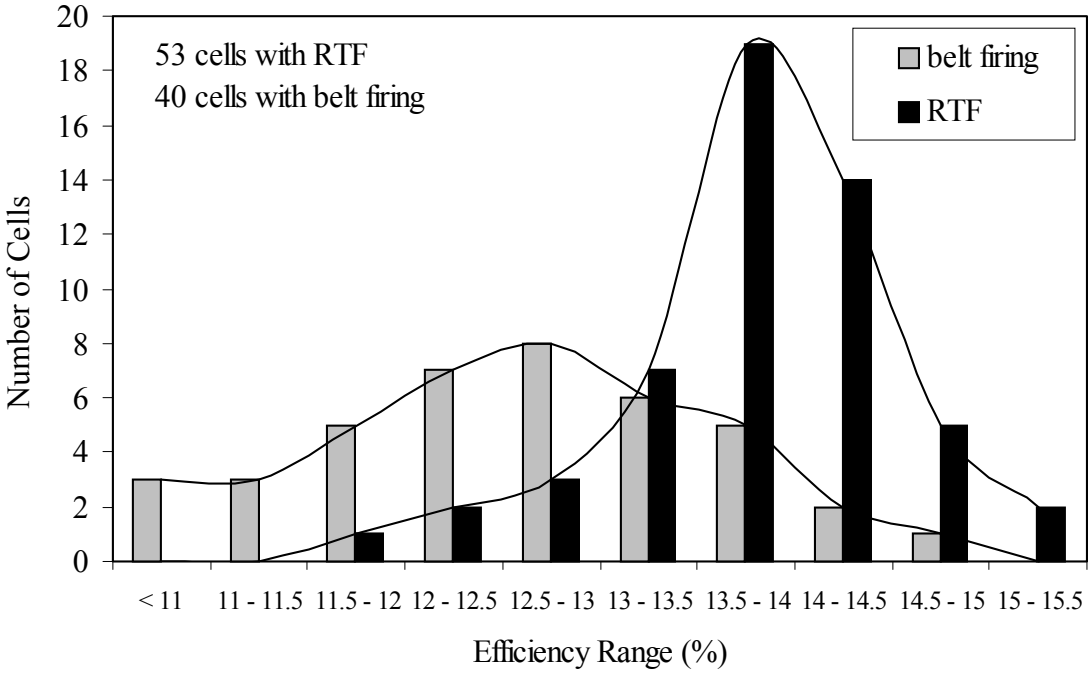

Figure 35. Efficiency distribution of String Ribbon cells with RTF and belt furnace front contact firing.

Table 10. Average String Ribbon cell efficiency for belt furnace contact firing and RTF.

Contact Firing	V_{oc} (mV)	J_{sc} (mA/cm^2)	FF	Eff. (%)
RTF	576	31.4	0.763	13.8
belt furnace	562	30.1	0.746	12.6

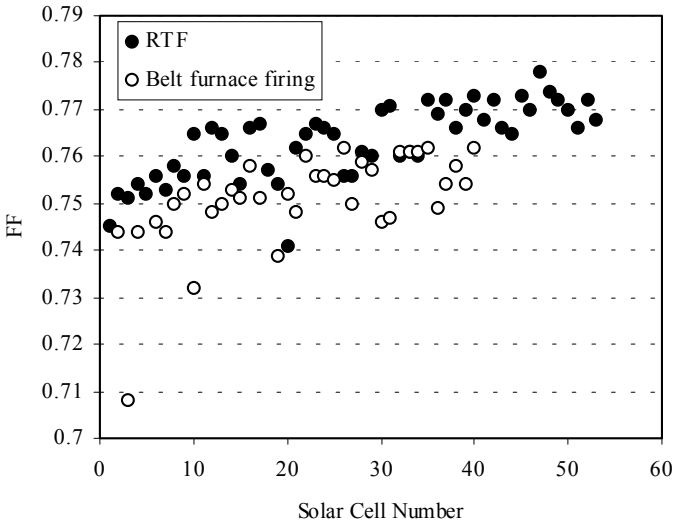

Figure 36. Distribution of FF for String Ribbon solar cells with RTF and belt furnace fired Ag contacts.

5.3.2 Comparison of the effective minority carrier diffusion length in String Ribbon cells with RTF and belt fired contacts

LBIC and light biased or differential IQE analysis were performed on cell b3-4 and cell 18-1, fired in the belt furnace and RTP respectively, in order to evaluate the effective diffusion length in these cells. These cells were selected for analysis because their efficiency is similar to the average efficiencies of cells fired with RTF and belt furnace firing shown in Table 10. LBIC scans were performed using the PVSCAN 5000 system with a 905 nm laser to scan each cell. Hemispherical reflectance and differential spectral response measurements were performed by focusing the one mm diameter, chopped monochromatic beam on the areas of the solar cells identified by LBIC analysis shown in Figure 37. The response in these areas was approximately equal to the average response for the entire cell. Differential spectral response [105] measurements were biased by steady illumination with white

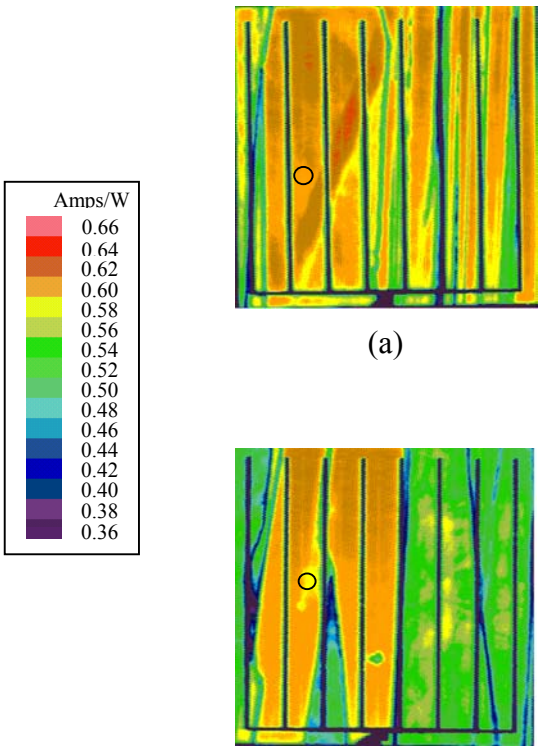

Figure 37. LBIC map of (a) cell 18-1 with RTF and an average spectral 0.53 A/W, and (b) cell b3-4 fired in the belt furnace with an average spectral response of 0.50 A/W. Circled areas indicate the location of the monochromatic beam during differential spectral response and hemispherical reflectance measurements.

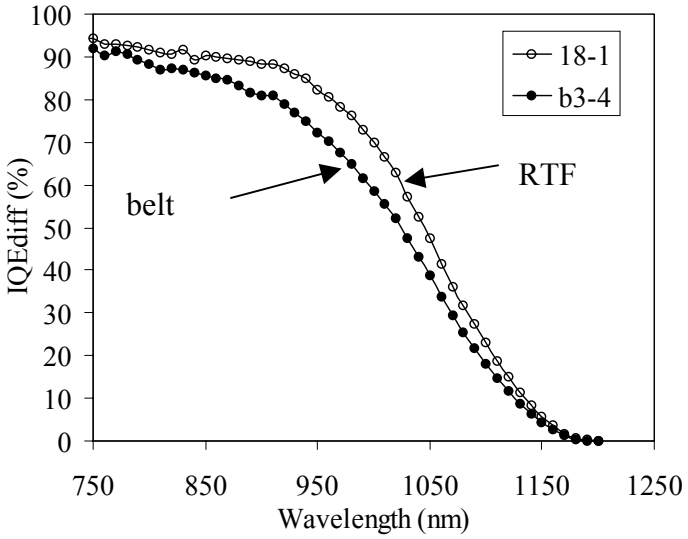

Figure 38. Long wavelength differential IQE of cells with RTF and belt furnace contact firing.

light. The long wavelength differential IQE of two cells, shown in Figure 38, indicates that cells with RTF have a higher response than those fired in the belt furnace, supporting the theory that RTF improves bulk by improving hydrogen retention and may improve the rear surface passivation in String Ribbon solar cells. The effective diffusion length, L_{eff}, in these four cells was determined by the well-known relation shown below using tabulated absorption coefficient, α, data and measured IQE data in the wavelength range of 800-900 nm.

$$\frac{1}{IQE} = 1 + \frac{1}{\alpha L_{eff}} \qquad (35)$$

L_{eff} values for the two cells analyzed, shown in Table 11, indicate that cell 18-1 with RTF has a higher effective diffusion length, as expected based on the IQE data in Figure 38. An estimate of the bulk diffusion length (L_{bulk}) in these cells was determined by

assuming a low rear surface recombination velocity (S=200 cm/s), which has been measured on 2 Ω-cm float zone silicon solar cells with a similar screen-printed Al-BSF [106]. Table 11 shows that the minimum bulk diffusion length in average regions of cell b3-4 fired in the belt furnace is 197 μm and 411 μm for cell 18-1 fired with RTF. This result supports the theory that rapid cooling during RTF may improve the retention of hydrogen at defects and promote hydrogen passivation.

Table 11. Results of L_{eff} analysis and L_{bulk} estimate for cells fired in the belt furnace and by RTF.

Cell	Firing	Efficiency (%)	L_{eff} (μm)	Minimum L_{bulk}* (μm)
b3-4	belt furnace	12.8	212	197
18-1	RTF	13.8	544	411

* - Denotes estimate value

5.3.3 Analysis of electrical activity of defects in String Ribbon solar cells with RTF and belt fired contacts

LBIC scans were made on cells taken from consecutive sections of the ribbon to identify differences in defect activity due to contact firing. After the SiN_x:H/Al hydrogenation at 850°C, cell 16-1 was subjected to RTF while cell 1-3 underwent

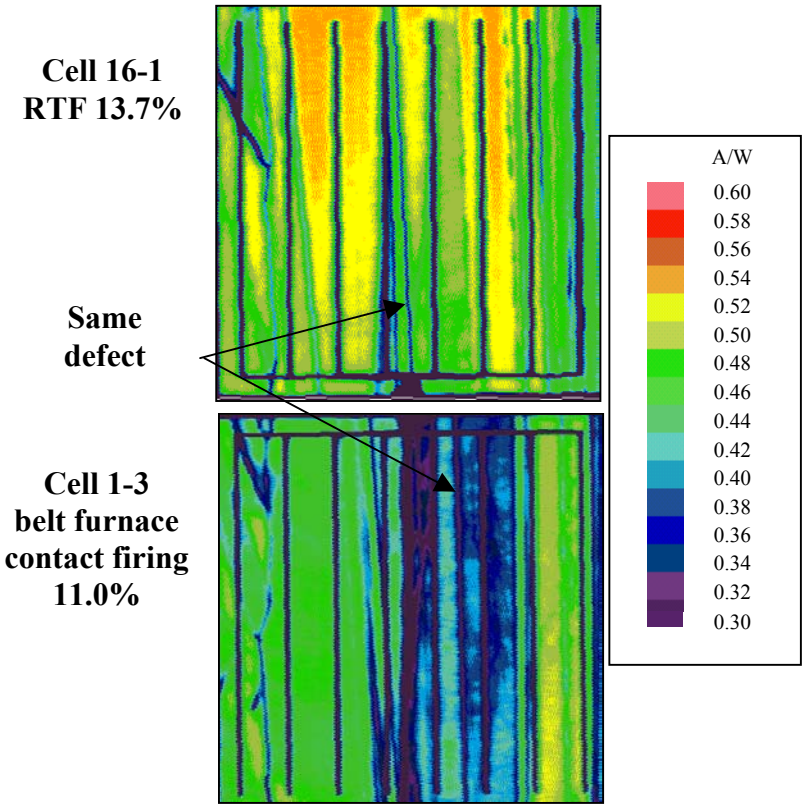

Figure 39. LBIC maps of String Ribbon solar cells from the same ribbon showing improved passivation of intergrain and intragrain defects by RTF.

belt contact firing. The LBIC maps of these cells, shown in Figure 39, demonstrate that these cells have similar crystallographic defect structures. The LBIC response reveals that intragrain regions improve from 0.58 A/W to 0.64 A/W due to RTF. Figure 39 also shows a defect whose activity decreases as the defect extends from cell 1-3 into cell 16-1. The reduced electrical activity of defects and the improvement in average cell efficiency (13.8% vs. 12.6%) suggest that RTF is more effective in retaining the hydrogenation introduced during the 850°C simultaneous Al/SiN_x:H anneal. In accordance with our model, these results suggest that the fast cooling rate associated with RTF improve the retention of hydrogen after the initial Al-enhanced SiN_x:H-induced hydrogenation. The slow ramp rates in belt furnace contact firing result in dehydrogenation of defects, increasing their electrical activity.

5.4 Conclusions

The results of this study demonstrate the importance of two components of the proposed physical model for SiN_x:H-induced hydrogenation, namely Al-Si alloying and hydrogen retention. While full Al coverage of the backside of samples results in the maximum spatially averaged lifetime enhancement of 219%, it causes 100 μm thick substrates to bow during Al-Si alloying. Partial Al coverage eliminates wafer bowing, but decreases the spatially averaged lifetime enhancement to 80% and validates the importance of Al during hydrogenation. This study also showed that the SiN_x:H-induced defect passivation can be improved by rapidly cooling samples after the hydrogenation anneal even when no Al is present on the back. Rapid cooling increases the retention of hydrogen at defects, improving defect passivation. RTF improves String Ribbon cell

efficiency by 1.2%, on average, over slower belt furnace contact firing. The efficiency improvement is the result of improved J_{sc}, V_{oc}, and FF. Based on our model for Al-enhanced hydrogenation, the improved bulk defect passivation during RTF is due to the fast cooling rate after the firing, which improves the retention of hydrogen at defects in the material. LBIC mapping and L_{eff} analysis of long wavelength differential IQE data confirm that RTF improves bulk and possibly surface passivation. An estimate of the minimum bulk diffusion length ranges from 99-197 μm for belt furnace fired cells to 247-411 μm for RTP fired cells. LBIC analysis also identified a reduction of the electrical activity of defects supporting the idea that RTF is more effective in retaining the hydrogenation introduced in the 850°C simultaneous Al/SiN_x:H anneal. The difference is largely attributed to a long contact firing time and slower cooling rate (4°C/s) during the belt process used in this study, which increases the dehydrogenation of defects.

CHAPTER 6

Investigation of the Deposition Conditions of SiN_x:H to Maximize Defect Passivation

In Chapter 5, the proposed model for SiN_x:H-induced hydrogenation was experimentally validated by demonstrating the importance of Al alloying during hydrogenation and the positive impact of rapid cooling. Rapid cooling was implemented using RTP to fabricate manufacturable String Ribbon solar cells with efficiencies as high as 14.7%. While this is a noteworthy achievement, the efficiency is still below the targeted cell efficiencies of 16-17%. The solar cell simulations in Figure 19 indicate that additional cell performance enhancement up to 16 % is possible with further lifetime improvement up to 75 μs if S_b is 100 cm/s to 300 cm/s. In this chapter, the proposed model for hydrogenation will be further examined to identify direction and means for further lifetime enhancement. One component of the model that has not yet been fully explored is the supply of hydrogen from the deposition and anneal of the PECVD SiN_x:H film. In this chapter, a low-frequency SiN_x:H film will be examined in order to increase the supply of H in the substrate and improve hydrogenation of defects in String Ribbon. The parallel plate PECVD reactor used in the experiments in Chapters 4 and 5 operated at a plasma excitation frequency of 13.56 MHz and had a throughput of fewer than 20

wafers per hour. The horizontal tube reactor design, shown in Figure 26, operates at frequencies below 500 kHz and has a throughput nearly 10 times that of the parallel plate reactor. Excitation frequency is an important parameter in PECVD film deposition and has been used to control the quality of SiN_x:H used as an interlayer dielectric or passivation film in integrated circuit technologies. During low frequency PECVD film deposition, the oscillation of the RF field is slow enough that ions are accelerated in one direction for a longer time and bombard the substrate with a higher energy. It has been shown that mixing high-frequency and low-frequency plasma excitation during PECVD SiN_x:H film deposition improves chemical reactions, increases film density, and changes the state of film stress from tensile to compressive [107]. Of importance to Si solar cells is the ion bombardment during low frequency PECVD, which may increase H incorporation during SiN_x:H deposition, and improve hydrogenation of defects in Si. Ion bombardment also creates surface damage and traps for hydrogen that enable incorporation of H during SiN_x:H deposition [108]. A theoretical model to fit experimental diffusion profiles of H in Si has been developed by Sopori et al. [85]. This model considers the capture of hydrogen at bulk and processing induced surface traps created during SiN_x:H deposition, and the release of hydrogen from traps during heat treatment [85]. In this chapter, the hydrogenation of defects in String Ribbon Si from the deposition and anneal of low and high frequency SiN_x:H films will be studied. To understand the mechanisms during hydrogenation from the two types of nitride films, the release of hydrogen from the nitride films during heat treatment will be measured by FTIR. In addition, secondary ion mass spectroscopy (SIMS) will be used to measure the depth profile of deuterium in Si substrates after nitride deposition from SiH_4 and

deuterated ammonia (ND_3) gases. Deuterium is substituted for hydrogen in this study because deuterium is a stable isotope of hydrogen and has one neutron making its mass two times greater than of hydrogen, enabling its detection by SIMS analysis. The goal of this chapter is to increase the supply of H during hydrogenation and improve defect passivation to enhance the lifetime in String Ribbon to over 80 μs.

6.1 Comparison of defect passivation from low-frequency and high-frequency PECVD reactors

It has been shown that the anneal of high-frequency (13.56 MHz) SiN_x:H films increases the lifetime in String Ribbon to over 30 μs when Al alloying occurs on the back surface. Without Al alloying, the lifetime enhancement after high-frequency SiN_x:H-induced hydrogenation reaches only 12 μs. In this section a SiN_x:H film deposited at low-frequencies is investigated in order to increase the supply of hydrogen and increase the lifetime to 100 μs or higher. To assess the degree of defect passivation, 300 μm-thick, 3 Ω-cm p-type String Ribbon samples were cleaned using the solutions listed in Appendix A. Then, a P diffusion was performed at 893°C in a tube furnace using a $POCl_3$ liquid source to achieve a sheet resistance of 40-45Ω/sq. Sample were cleaned after P diffusion and a PECVD SiN_x:H film was deposited on String Ribbon Si samples using a parallel plate PECVD reactor operating at high-frequency (13.56 MHz) or a horizontal tube PECVD system operating at low-frequency (50 kHz). The relevant

Table 12. Deposition parameters for HF and LF SiN_x:H depositions and in-situ NH_3 plasma pretreatments.

	Deposition Parameter	HF SiN_x:H	LF SiN_x:H
SiN_x:H deposition	Plasma excitation frequency	13.56 MHz	50 kHz
	Temperature	300°C	430°C
	Plasma Power	30 W	150 W
	Pressure	0.9 Torr	2 Torr
	SiH_4 flow rate	320 sccm (2% SiH_4 in N_2)	300 sccm (100% SiH_4)
	NH_3 flow rate	6.0 sccm	300 sccm
	N_2 flow rate	900 sccm	0 sccm
	Deposition time	6.75 min	4.1 min
NH_3 plasma pretreatment	Plasma excitation frequency	13.56 MHz	50 kHz
	Temperature	300°C	430°C
	Plasma Power	250 W	250 W
	Pressure	0.9 Torr	1.5 Torr
	NH_3 flow rate	6.0 sccm	1000 sccm
	N_2 flow rate	900 sccm	0 sccm
	Pretreatment time	2.0 min	2.0 min

parameters for high-frequency (HF) and low-frequency (LF) SiN_x:H deposition are provided in Table 12. To increase hydrogen incorporation in Si, selected samples were subjected to an NH_3 plasma pretreatment performed at low- and high frequency before SiN_x:H deposition. The plasma processing parameters for the NH_3 plasma pretreatment steps before LF and HF SiN_x:H deposition are also given in Table 12. After SiN_x:H deposition, String Ribbon samples were annealed in an RTP system at temperatures in the range of 650-850°C to the drive hydrogen from the SiN_x:H film. To investigate Al-enhanced hydrogenation with LF and HF SiN_x:H, an Al paste (*Ferro 53-038*) was screen-printed on the back of selected String Ribbon wafers before RTP heat treatment. After heat treatment, the Al, n^+, and p^+ layers were removed by chemical etching and samples were cleaned before post-processing lifetime measurement using the solutions listed in Appendix A.

6.1.1 Beneficial effect of in-situ NH_3 plasma pretreatment on lifetime enhancement during low- and high-frequency SiN_x:H-induced hydrogenation

To investigate the effect of an in situ-NH_3 plasma pretreatment step prior to LF and HF SiN_x:H deposition, lifetime measurements were performed after heat treatment of SiN_x:H coated samples with and without pretreatment. After NH_3 plasma pretreatment and SiN_x:H film deposition, Al was printed on the back of all samples. The samples coated with LF and HF SiN_x:H were annealed in RTP at optimum temperatures of 740°C and 800°C respectively. The identification of the optimum hydrogenation anneal temperatures for LF and HF SiN_x:H films is described in Chapter 7. Figure 40 shows that

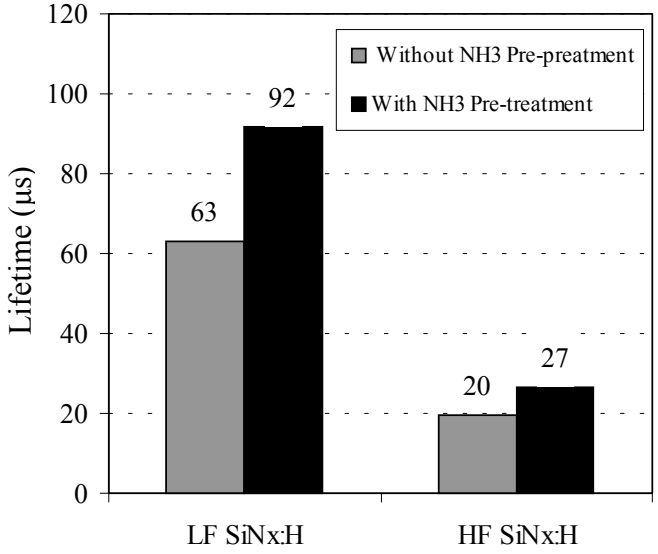

Figure 40. Effect of in-situ NH_3 plasma pretreatment before LF and HF SiN_x:H deposition on lifetime enhancement. The as-grown lifetime was 5 µs.

without pretreatment, LF SiN_x:H-induced hydrogenation increased the lifetime to 63 µs, while anneal of HF SiN_x:H increased the lifetime to only 20 µs. This result indicates that the deposition and anneal of LF SiN_x:H is more effective in passivating defects in String Ribbon. Recently, it has been shown that LF SiN_x:H is more effective than HF SiN_x:H in reducing the recombination activity of defects in mc-Si solar cells [109]. The effectiveness of the LF SiN_x:H hydrogenation may be due to an increased supply of hydrogen in the SiN_x:H film or hydrogen incorporation in Si during SiN_x:H deposition. The hydrogen content in SiN_x:H films and the incorporation of H during PECVD SiN_x:H deposition are analyzed in Sections 6.2 and 6.3. Figure 40 shows that the addition of an NH_3 plasma pretreatment step improves the SiN_x:H-induced lifetime enhancement for both LF and HF SiN_x:H films, but was more beneficial for LF SiN_x:H-induced

hydrogenation. The pretreatment step before LF SiN_x:H deposition improved the lifetime by 29 μs, resulting in a final lifetime of 92 μs. The HF-pretreatment was not as effective and provided a lifetime increase of only 7 μs, and a final lifetime of 27 μs.

6.1.2 Impact of simultaneous Al alloying on low-frequency and high-frequency SiN_x:H-induced hydrogenation

In Chapter 4, it was shown that Al plays an important role in HF SiN_x:H-induced hydrogenation. However Al alloying causes thin wafers (100 μm) to bow, preventing the implementation of Al-enhanced hydrogenation on thin solar cells. Wafer bowing during Al alloying can be eliminated if the Al coverage fraction is reduced to 75%. Unfortunately, as shown in Section 5.1, decreasing the Al coverage fraction also reduces the degree of defect passivation. There is a need to develop an effective defect hydrogenation process that does not require Al, or depend on it strongly. In this section, LF SiN_x:H-induced hydrogenation is studied to determine if Al plays a significant role in hydrogenation. Figure 41 shows the lifetime enhancement from a LF and HF SiN_x:H films with and without Al alloying on the back of String Ribbon wafers. The lifetime after HF SiN_x:H-induced hydrogenation at 800°C without Al was only 9 μs and is consistent with the results in Chapter 4. When Al was present on the back during HF SiN_x:H-induced hydrogen, the lifetime reached 29 μs, once again demonstrating Al-enhanced hydrogenation. Figure 41 shows that hydrogenation during the anneal of LF SiN_x:H film at 740°C increased the lifetime to 91 μs even when no Al is present on the back. When Al is present on the back of the wafer during LF SiN_x:H-induced hydrogenation at 740°C, the lifetime increased to 106 μs. The relatively small difference in the lifetime of samples with and without Al (15 μs) indicates that Al does not play as

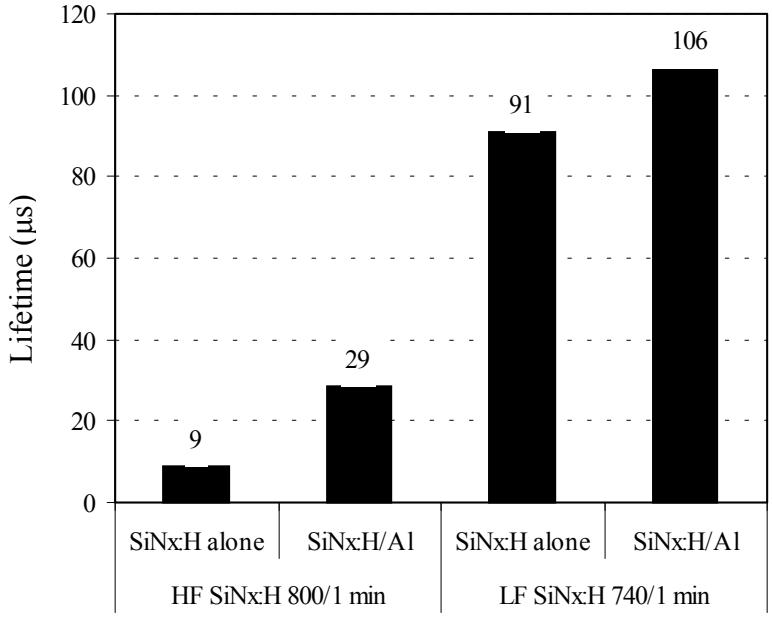

Figure 41. Impact of Al on hydrogenation of String Ribbon Si from low- and high-frequency PECVD SiN_x:H. The as-grown lifetime was 5 μs.

significant a role in hydrogenation from LF SiN_x:H as it does in the case of HF SiN_x:H-induced hydrogenation. In accordance with the proposed model, Al may not play a vital role in hydrogenation if there is a large supply of hydrogen. If LF SiN_x-induced hydrogenation increases the supply of hydrogen in Si, then Al-induced dissociation of molecular hydrogen by vacancies and the enhanced transport of hydrogen in Si may not be required for effective hydrogenation. The results in this section demonstrate that hydrogenation from the LF SiN_x:H film provides an additional lifetime enhancement and is less dependent on the presence of Al, presumably due to an increased supply of hydrogen.

6.2 Quantitative assessment of the release of bonded hydrogen from low- and high-frequency SiN_x:H films

To determine if the enhanced hydrogenation from LF SiN_x:H films is due to a greater supply of hydrogen from SiN_x:H, the release of hydrogen from LF and HF SiN_x:H films was measured by FTIR. Before FTIR measurements, 300 μm-thick, 500 Ω-cm n-type float zone Si wafers were cleaned in the solutions listed in Appendix A. After cleaning, wafers were coated with LF and HF SiN_x:H films as described in Section 6.1.1 using the deposition parameters in Table 12. An NH_3 plasma pretreatment was performed before LF SiN_x:H deposition, while no pretreatment was performed before HF SiN_x:H deposition. A DigiLab FTS 6000 FTIR was used to collect FTIR spectra, and the

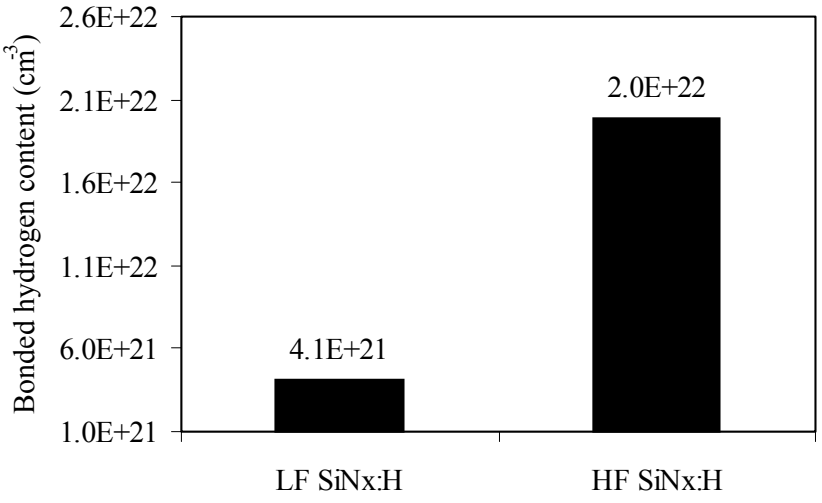

Figure 42. Bonded H content in as-deposited LF and HF SiN_x:H.

DigiLab Win-IR Pro software was used to calculate the area under the Si-H and N-H peaks located at 2160 cm^{-1} and 3350 cm^{-1}, respectively. The total bonded hydrogen content in SiN_x:H films was determined by calculating the Si-H and N-H bond densities as described in Ref. 83. Figure 42 shows that the hydrogen content in HF and LF SiN_x:H films is 2.0 x 10^{22} cm^{-3} and 4.1 x 10^{21} cm^{-3} respectively. This suggests that there is more hydrogen available in HF SiN_x:H for defect passivation, even though the results in Section 6.1 clearly show that LF SiN_x:H-induced hydrogenation is more effective. Figure 43 shows the bonded hydrogen content in HF and LF SiN_x:H films after heat treatment in RTP at temperatures in the range of 650-850°C. After anneal at 600°C, the bonded hydrogen content in HF SiN_x:H films drops to 3.6 x 10^{21} cm^{-3}, a decrease of 82% when compared to the as deposited film. This result indicates that most of the hydrogen in HF

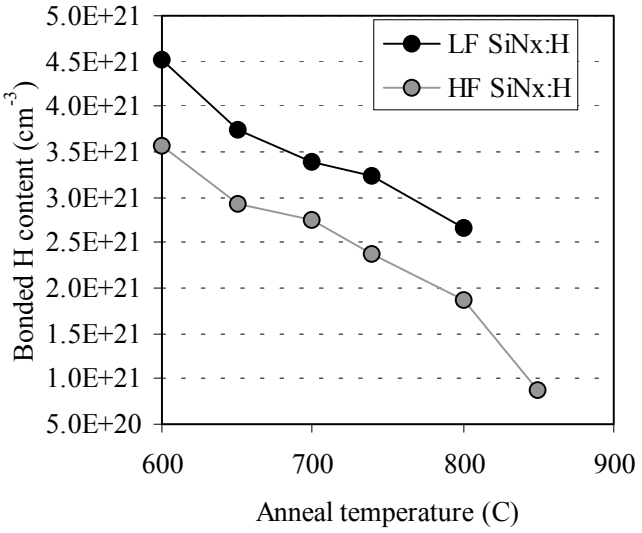

Figure 43. Decrease in the bonded H content in LF and HF SiN_x:H films as a function of anneal temperature. The anneal time was 60 s.

SiN_x:H films is released at or below 600°C and the hydrogen content decreases at a rate of 1 x 10^{21} cm^{-3} for every 100°C increase of temperature. Figure 43 shows that after anneal at 600°C, the hydrogen content in LF SiN_x:H films is essentially unchanged from the as-deposited state. Further increase in the anneal temperature releases of hydrogen at a rate of 9 x 10^{20} cm^{-3} for every 100°C increase of the anneal temperature. These results show that not only is there more hydrogen in HF SiN_x:H after deposition, hydrogen is easily released from this film during the same heat treatment. Thus it must be concluded that the ability of a SiN_x:H film to provide defect hydrogenation cannot be judged solely on the bonded hydrogen content in the nitride film.

6.3 Demonstration of hydrogen incorporation near the Si surface during PECVD SiN_x:H deposition

Section 6.1 showed that LF SiN_x:H-induced hydrogenation is more effective than HF SiN_x:H even though there is less hydrogen released from HF SiN_x:H films. This suggests that there may be an additional source of hydrogen that is responsible for the enhanced bulk defect passivation provided by LF SiN_x:H films. In this section, hydrogen incorporation in Si is measured after LF and HF SiN_x:H deposition by SIMS depth profiling. Deuterated ammonia (ND_3) was substituted for NH_3 during LF and HF SiN_x:H deposition in order to detect deuterium incorporation. SiN_x:H was deposited using LF and HF PECVD on mirror polished, 8 Ω-cm p-type Czochralski Si wafers. After deposition, SiN_x:H films were removed in dilute HF and SIMS depth profiles of deuterium in Si were measured by the Surface Analysis Group at the National Renewable

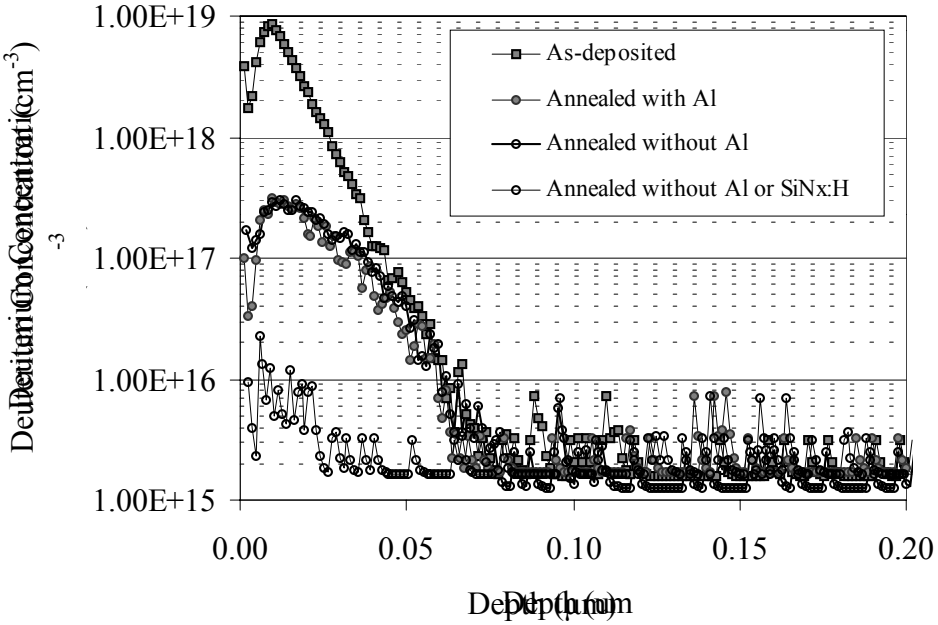

Figure 44. SIMS depth profiles of deuterium in Si after deposition of LF SiN_x:H at 300°C and anneal in RTP at 740°C for 60 s.

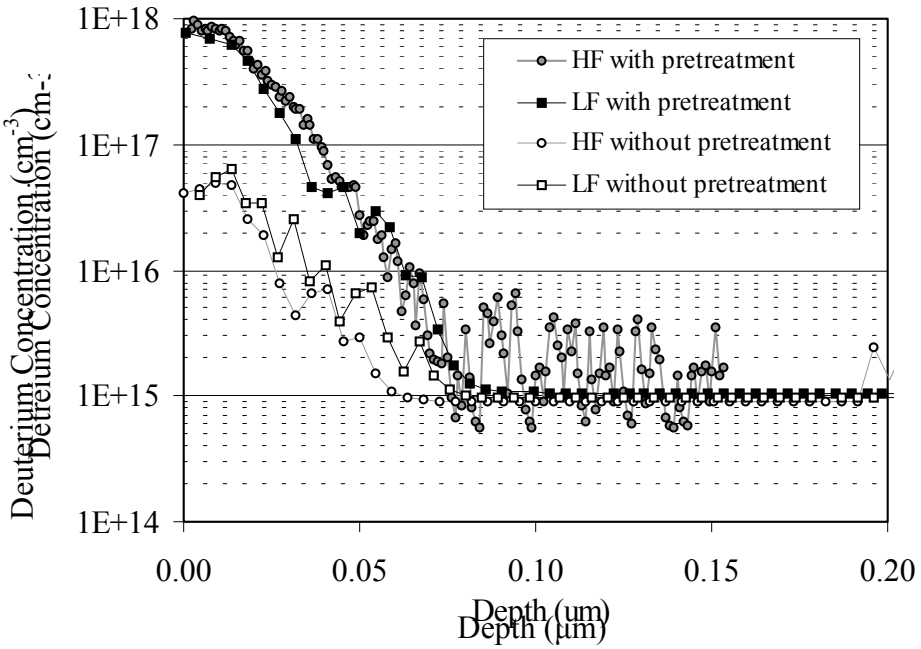

Figure 45. SIMS depth profiles of deuterium in Si after deposition of LF and HF SiN_x:H with and without in-situ ND_3 plasma pretreatment.

Energy Laboratory. Figure 44 shows the deuterium profile in Si measured by SIMS after LF SiN_x:H deposition at 300°C and anneal at 740°C for 1 minute. in RTP. The detection limit for deuterium in these SIMS measurements is approximately 10^{15} cm^{-3}. Figure 44 shows that the deuterium depth profile after deposition at 300°C has a surface concentration of 8 x 10^{18} cm^{-3} and can be detected up to 0.064 μm where the deuterium concentration reaches the detection limit. The detection of deuterium incorporation in Si by SIMS after direct and remote PECVD SiN_x:H deposition from deuterated reactant gases has also been recently reported by Refs. 110 and 111. Ref. 110 reported a deuterium surface concentration of 10^{18} cm^{-3} and an incorporation depth of about 0.10 μm after direct PECVD SiN_x:H deposition. Figure 44 also shows that the anneal at 740°C for 1 minute. reduced the surface concentration of deuterium from 8 x 10^{18} cm^{-3} to 3 x 10^{17} cm^{-3}. This result demonstrates that the hydrogen incorporated during PECVD deposition may act as an additional source of hydrogen. The data in Figure 44 also shows that the presence of Al during the anneal does not result in significant change in the deuterium profile in Si. The inability to detect enhanced deuterium diffusion due to Al may be due to the high detection limit (10^{15} cm^{-3}) of the SIMS measurement. Recently, infrared spectroscopy has been performed on hydrogenated, Pt doped Si to determine the bulk concentration of H in Si after hydrogenation from the HF SiN_x:H film used in this thesis [112]. The latest results show that the H concentration in the bulk of Si is in the range of 1-5 x 10^{13} cm^{-3} [112], and well below the detection limit of SIMS. This result supports the idea that the extent of the deuterium profiles in this section cannot be fully detected by SIMS. Figure 44 also shows the profile of deuterium in a Si wafer in which the SiN_x:H film was removed in dilute HF before heat treatment. The surface

Table 13. Dose and depth of deuterium incorporation in Si after LF and HF SiN_x:H deposition.

Processing Condition	Dose (atoms/cm^2)	Depth (μm)
HF SiN_x:H without pretreatment	1.11×10^{11}	0.064
LF SiN_x:H without pretreatment	1.30×10^{11}	0.080
HF SiN_x:H with pretreatment	1.87×10^{12}	0.079
LF SiN_x:H with pretreatment	1.63×10^{12}	0.090

concentration of deuterium in this sample after heat treatment is only 2×10^{16} cm^{-3}, which is more than an order of magnitude lower than in the other samples that were annealed with the SiN_x:H coatings. This indicates that SiN_x:H prevents the out diffusion of hydrogen during heat treatment. Figure 45 shows the deuterium profile in Si under HF and LF SiN_x:H films deposited with and without NH_3 plasma pretreatment. Figure 45 shows that in spite of the different plasma excitation frequencies during deposition, there was only a small difference in the incorporation of deuterium in Si during LF and HF SiN_x:H depositions. In both HF and LF SiN_x:H depositions, the surface concentration of deuterium was 4×10^{16} cm^{-3}. Table 13 shows that the dose of deuterium in Si after deposition from LF SiN_x:H was slightly higher (1.30×10^{11} cm^{-2}) than the dose after HF SiN_x:H (1.11×10^{11} cm^{-2}). The lifetime enhancement provided by LF SiN_x:H-induced hydrogenation without pretreatment shown in Figure 40 may be only partly explained by the higher dose of hydrogen during LF SiN_x:H deposition. Also contributing to LF SiN_x-induced hydrogenation is deeper hydrogen incorporation that is expected during LF

SiN_x:H because deposition is performed at a higher temperature (430°C). The data in Figure 45 shows that the addition of an ND_3 pretreatment increases deuterium incorporation resulting in a surface concentration of 8 x 10^{17} cm^{-3} for both HF and LF SiN_x:H films. The pretreatment also increases the dose of deuterium in Si to 1.87 x 10^{12} cm^{-2} and 1.63 x 10^{12} cm^{-2} for HF and LF SiN_x:H respectively. Therefore the lifetime enhancement of 29 μs provided by NH_3 pretreatment before LF SiN_x:H deposition, shown in Figure 40, is attributed to enhanced hydrogen incorporation which increases the supply of hydrogen. NH_3 plasma pretreatment before HF SiN_x:H deposition also enhances H incorporation as shown in Figure 45. However, Figure 40 shows that NH_3 plasma pretreatment before HF SiN_x:H deposition resulted in a lifetime enhancement of only 7 μs. The small lifetime enhancement from NH_3 pretreatment before HF SiN_x:H deposition and anneal cannot be predicted from the SIMS data in Figure 45 and may be due to the lower deposition temperature (300°C) that prevents deep H incorporation, undetectable by SIMS .

6.4 Conclusions

The results presented in this chapter show that LF SiN_x:H-induced hydrogenation increases the lifetime in String Ribbon to 92 μs and 62 μs with and without in situ NH_3 plasma pretreatment, respectively. It is shown that LF SiN_x:H is more effective than HF SiN_x:H-induced hydrogenation in passivating defects in String Ribbon because HF SiNx-induced hydrogenation results in a lifetime of only 29 μs. However, FTIR measurements of SiN_x:H films showed that there is more bonded hydrogen in HF SiN_x:H after

deposition and this hydrogen is more easily released during heat treatment. Therefore the enhanced hydrogenation from LF SiN_x:H cannot be explained by a larger supply of hydrogen in the LF SiN_x:H film. To identify an additional source of hydrogen to explain the lifetime enhancement, the incorporation of deuterium in Si during SiN_x:H deposition was measured by SIMS. The SIMS depth profile of deuterium in Si had a surface concentration of 8×10^{18} cm^{-3} after LF SiN_x:H deposition at 300°C, and deuterium can be detected up to 0.064 μm. Heat treatment after LF SiN_x:H deposition reduced the surface concentration of deuterium suggesting that the incorporated hydrogen may act as an additional source of hydrogen during LF SiN_x:H-induced hydrogenation. When the SiN_x:H film was removed before heat treatment, the surface concentration of deuterium drops to 2×10^{16} cm^{-3} after heat treatment, suggesting that the SiN_x:H film helps to prevent out diffusion of hydrogen.

The results of the lifetime studies in this chapter also show that the addition of a NH_3 plasma pretreatment step before nitride deposition improves the SiN_x:H-induced hydrogenation for both LF and HF SiN_x:H films. The pretreatment step was more beneficial for LF SiN_x:H-induced hydrogenation, providing an increase in the lifetime of 29 μs and resulting in a final lifetime of 92 μs. The plasma pretreatment increased deuterium incorporation for both HF and LF SiN_x:H films and delivered a dose of deuterium in Si equal to 1.87×10^{12} cm^{-2} and 1.63×10^{12} cm^{-2} for HF and LF SiN_x:H respectively. The small difference in the lifetime of samples with and without Al during (15 μs) indicates that Al does not play a crucial a role in LF SiN_x:H-induced hydrogenation. This result can be explained by the proposed hydrogenation model only if there is a large supply of hydrogen. The lifetime enhancement provided by three

processes cannot be explained on the basis of the deuterium profiles measured in this chapter. First, the SIMS measurements were only able to detect a small difference in the incorporation of deuterium in Si under LF and HF SiN_x:H even though LF SiN_x:H hydrogenation results in a much higher lifetime. Second, NH_3 plasma pretreatment before HF SiN_x:H deposition enhanced the hydrogen profile under the SiN_x:H film, but did not dramatically increase the lifetime. These results may be explained by H incorporation deep in Si that is not detectable by SIMS. Deeper hydrogen incorporation is expected from the deposition of LF SiN_x:H because it is performed at 430°C, while HF SiN_x:H deposition is performed at 300°C. The final process that cannot be explained by the SIMS data in this chapter is Al-enhanced hydrogenation. Al alloying on the back of the wafer during hydrogenation did not alter the deuterium profile within the first 0.1 μm of Si as expected. This may also be a result of the inability to measure the deuterium profile deeper in Si where Al alloying may enhance the transport of deuterium. To detect hydrogen at lower concentrations and support the proposed hydrogenation model, another profiling technique, such the infrared spectroscopy of Pt-H pairs presented in Ref. 112, must be used.

CHAPTER 7

Development of a Rapid Thermal Anneal (RTA) for Enhanced Low-frequency SiN_x:H-induced Hydrogenation and High-efficiency String Ribbon Solar Cells

Chapter 6 showed that SiN_x:H-induced hydrogenation is more effective when the nitride is deposited using low-frequency plasma excitation. Hydrogenation from a low-frequency SiN_x:H film annealed at 740°C for one minute resulted in a lifetime of 92 μs. With this lifetime, the simulations in Chapter 3 indicate that a solar cell efficiency greater than 16% can be achieved if the surface recombination velocity is 300 cm/s or less. In this chapter, the optimum rapid thermal anneal (RTA) temperatures for LF SiN_x:H-induced hydrogenation is determined to understand the hydrogenation mechanism. During low-frequency SiN_x:H deposition, ions in the plasma can follow the RF field and may be accelerated and implanted into the String Ribbon substrate. However during high-frequency film deposition, reactant ions in the plasma are "frozen" with respect to the oscillation of the RF field and are not accelerated and implanted into the String

Ribbon substrate. As a result, low-frequency SiN_x:H deposition may increase the supply of H. The data in Chapter 6 suggests that H in the substrate is redistributed and driven deeper in the substrate during heat treatment. Sopori et al. [85] have proposed a model for the diffusion of hydrogen in Si that includes trapping and de-trapping of hydrogen at defect sites in Si. This model is based on the formation of processing induced traps during PECVD film deposition and hydrogen trapping and de-tramping from these traps. Simulations based on the model of Sopori et al. demonstrate that the incorporated H is released from processing-induced traps near the surface when the sample is annealed [85]. This model along with the model proposed in Chapter 4 will be used to understand the development of an optimum hydrogenation temperature. The optimum hydrogenation temperature may be the result of competition between the supply of H to defects and the retention of H at defects. The optimum hydrogenation temperature is also studied through the fabrication and analysis of String Ribbon solar cells.

String Ribbon solar cells are made with a two-step contact firing scheme in order to obtain optimum hydrogenation and high-quality screen-printed contacts. The performance of these solar cells experimentally demonstrates the importance of lifetime enhancement on cell performance. The optimum hydrogenation anneal temperature is implemented in a two-step contact firing scheme to fabricate high-efficiency String Ribbon solar cells with screen-printed contacts. A room temperature scanning photoluminescence mapping technique is employed to characterize the defect passivation in String Ribbon samples and further support the optimum hydrogenation temperature. Then, RTA of pre-hydrogenated String Ribbon samples is performed to understand the

retention of H at defects. Finally the RTA time is reduced to merge the hydrogenation anneal and Ag contact firing, without significantly reducing the lifetime enhancement.

7.1 Optimization of the RTA temperature for low-frequency SiN_x:H-induced hydrogenation of defects in String Ribbon

This section focuses on the optimization of the RTA temperature for LF SiN_x:H-induced hydrogenation. The objective of the carrier lifetime optimization study in this section is to gain insight on the HF and LF SiN_x:H-induced hydrogenation mechanisms that are at play during RTA at various anneal temperatures. To understand the hydrogenation mechanisms, the lifetimes of String Ribbon samples are measured after HF and LF SiN_x:H-induced hydrogenation at temperatures in the range of 600°C to 900°C. The results of this study are then interpreted with the aid of the proposed model for hydrogenation. Then String Ribbon solar cells are fabricated to demonstrate the significance of lifetime enhancement that results from LF SiN_x:H-induced hydrogenation. A two-step firing scheme is implemented in order to study the effect of hydrogenation in String Ribbon solar cells independent of Ag grid firing. Step 1 provides effective SiN_x:H-induced hydrogenation and is designed to have a fast ramp-up rate (50°C/s) to improve Al-BSF quality, but is not suitable for sintering the Ag contacts. Step 2, also performed in RTP, is designed for optimal Ag contact sintering and high retention of hydrogen at defects introduced in Step 1. In this section, cells benefit from optimized RTP cycles designed for PECVD SiN_x:H-induced hydrogen passivation of bulk defects, good ohmic contacts, and the formation of an effective Al-BSF. Finally in this section,

the reduction of the electrical activity of defects in String Ribbon due to hydrogen passivation is assessed by a room-temperature scanning photoluminescence technique. This measurement is performed before and after LF SiN_x:H hydrogenation on String Ribbon silicon to demonstrate maximum defect passivation at the optimum hydrogenation anneal temperature.

Substrates for the carrier lifetime and scanning photoluminescence studies, and solar cell fabrication were ~300 μm thick, ~3 Ω-cm String Ribbon Si grown by Evergreen Solar. After substrate growth, P diffusion was performed on all samples in a conveyor belt furnace at Evergreen Solar to form the n^+-emitter with a sheet resistance of 45-50 Ω/sq. A LF SiN_x:H film was deposited on top of the n^+-emitter of all samples in commercial low-frequency (kHz range) PECVD at Evergreen Solar with refractive index of 2.0 and thickness of 780 Å. A commercial Al paste (*Ferro FX-53-038*) was printed on the entire backside of all wafers and annealed in a single wafer RTP system at temperatures in the range of 600-800°C. This simultaneous anneal of Al and SiN_x:H involves fast a ramp-up rate (50°C/s) and cooling rate (30°C/s) to promote and enhance PECVD SiN_x:H-induced hydrogen passivation of defects in Si. Samples coated with LF SiN_x:H were annealed at 700°C for one second after hydrogenation to simulate two-step RTP firing. To complete fabrication of solar cells, a grid pattern was screen printed using a commercial Ag paste (*Ferro 3349*) on top of the SiN_x:H AR coating and fired through SiN_x:H rapidly at 700°C for one second in RTP to form ohmic contact to the n^+-emitter. Solar cells were isolated using a dicing saw and annealed in forming gas (10% H_2 in N_2) at 400°C for ~10 min. In order to determine the minority carrier lifetime in finished solar cells, the metallization, SiN_x film, and diffused layers were removed using the solutions

listed in Appendix A. QSSPC lifetime measurements were performed with Si samples immersed in a solution of 70 mg of I_2 in 250 mL of methanol.

7.1.1 Effect of anneal temperature on lifetime enhancement provided by HF and LF SiN_x-induced hydrogenation

The lifetime of String Ribbon substrates after SiN_x:H-induced hydrogenation with Al on the back surface at temperatures in the range of 700-900°C is shown in Figure 46. Samples coated with LF SiN_x:H were annealed at 700°C for one second after hydrogenation to simulate two-step RTP firing. The first observation that can be made from Figure 46 is that LF SiN_x:H-induced hydrogenation is superior to HF SiN_x:H-induced hydrogenation for all temperatures investigated. At 700°C the hydrogenation

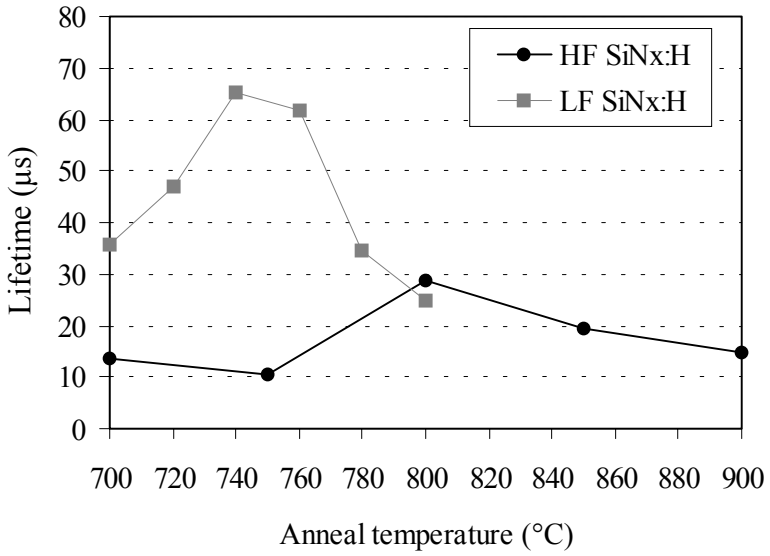

Figure 46. Lifetime enhancement from HF and LF SiN_x:H for hydrogenation anneals performed at 700-900°C. The average as-grown lifetime was 3 µs.

from LF SiN_x:H results in an average lifetime of 35 μs in String Ribbon. As the anneal temperature is increased to 720°C, the average lifetime after LF SiN_x:H-induced hydrogenation increases to 47 μs, and reaches a maximum of 65 μs at 740°C. This increase in lifetime up to 740°C is attributed to the release of H from the SiN_x:H film and from the surface of Si as shown in Chapter 6. Figure 46 also shows that defect hydrogenation from HF SiN_x:H films annealed at 700°C to 750°C results in average lifetimes of only 10-13 μs. The average lifetime increases to a maximum of 29 μs when the anneal temperature reaches 800°C, likely due to the greater release of bonded hydrogen from the HF SiN_x:H film. The increase in the release of bonded hydrogen from HF SiN_x:H was measured by FTIR and plotted in Figure 43. The lifetime decreases after hydrogenation above 740°C and 800°C for LF and HF SiN_x:H-induced hydrogenation respectively. This decrease in lifetime is probably due to the low retention of H in Si at high temperatures, resulting in the dehydrogenation of defects. Dehydrogenation of defects causes the lifetime to decrease to 25 μs and 15 μs after LF and HF SiN_x:H-induced hydrogenation at 800°C and 900°C respectively. The key observations in Figure 46 are: a) both LF and HF SiN_x:H nitride films exhibit an optimum anneal temperature; and b) the optimum anneal temperature is different for the two films.

Figure 46 suggests that there are competing factors in the LF and HF SiN_x:H hydrogenation processes that lead to the optimum hydrogenation temperatures. The optimum hydrogenation temperatures (T^*_{LF} and T^*_{HF}) observed in String Ribbon Si may be the result of competition between the release of H from SiN_x:H and H traps in Si, and the retention of H at defects in Si. The release of H from traps created during solar cell processing is predicted by the model of Sopori et al [85]. This model proposes that H is

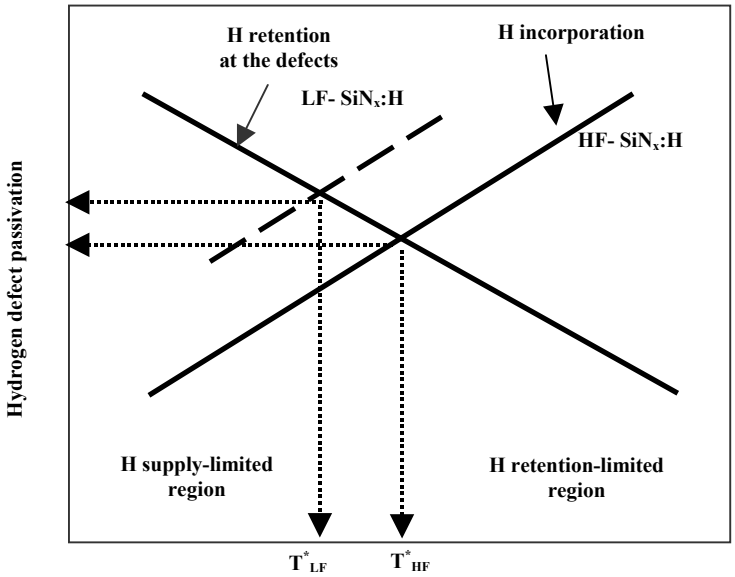

Figure 47. Illustration of the formation of the optimum hydrogenation anneal temperature from the competition between H incorporation and retention.

trapped and "stored" in Si after SiN_x:H deposition. Simulations based on this model show that stored H is released during heat treatment at 800°C and may diffuse throughout the wafer in 10 s when the density of H traps in the bulk is 10^{16} cm^{-3}[85]. The competition between the supply of hydrogen released from the SiN_x:H film and stored in H traps in Si and H retention at defects is illustrated in Figure 47. Hydrogenation from LF-SiN_x:H and HF-SiN_x:H SiN_x films is represented by two H incorporation curves. The incorporation of H from both LF-SiN_x:H and HF-SiN_x:H films increases with anneal temperature because more hydrogen is released from the SiN_x:H film. However, more H may be available in the case of LF-SiN_x if there is larger incorporation of H in Si during SiN_x deposition. At temperatures below the optimum, hydrogenation of bulk defects is limited by the low release of atomic hydrogen from the SiN_x:H film and H stored in Si. As the anneal temperature is increased, more hydrogen is released from the SiN_x:H film

and H traps in Si. Additionally, Al-Si alloying may begin to play a role in hydrogenation as proposed in Chapter 4. Vacancies may be generated by the Al alloying process, and may enhance hydrogenation by increasing the flux of hydrogen into Si and dissociate H_2 into H. Additionally, the high solubility of H in the Al-Si melt may enhance the transport of H deep in Si. However, as shown in Chapter 6, Al plays a small role in LF SiN_x:H-induced hydrogenation, probably due to the increased supply of H. Opposing H incorporation is the retention of H at defect sites in Si. It is well know that H evolves from defect sites in Si at temperatures above 400°C [4.13]. The retention of H at defect sites decreases as the anneal temperature increases and is represented by the gray curve in Figure 47, and may be influenced by the cooling rate after the anneal. The optimum anneal temperature for LF and HF SiN_x:H-induced hydrogenation occur at the intersection of the H retention line and H incorporation lines for LF-SiN_x:H and HF-SiN_x:H. Therefore, the optimum hydrogenation temperature represents a balance between the release of hydrogen from trap sites and the SiN_x:H film and the retention of hydrogen at electrically active defects in Si. The optimum hydrogenation temperature for LF SiN_x:H is lower because Si subsurface damage provides additional source of hydrogen and the defect passivation is strongly limited by the retention.

7.1.2 Assessment of the impact of LF SiN_x:H-induced hydrogenation on String Ribbon Si solar cell performance

In this section, the effect of the hydrogenation anneal temperature will be investigated in String Ribbon solar cells to demonstrate the significance of lifetime enhancement shown in Figure 46. Fabrication of String Ribbon solar cells with co-firing the Al and Ag contacts at temperatures above 700°C damages the junction and reduces the fill factor.

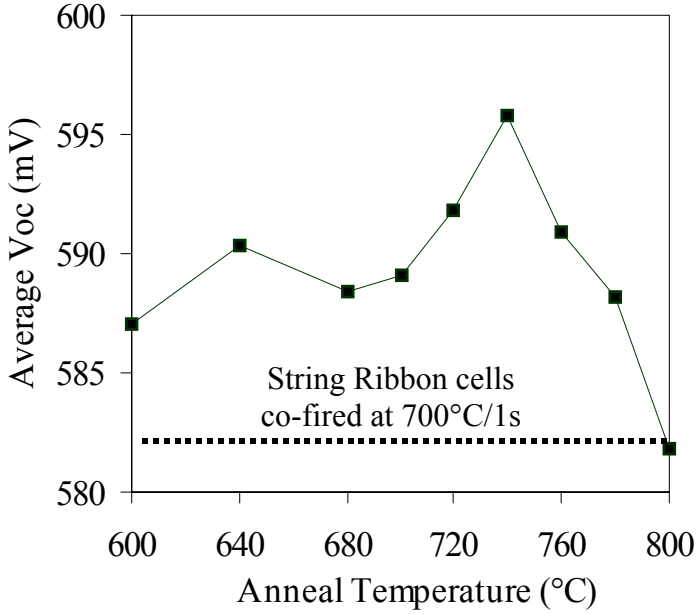

Figure 48. Impact of the LF SiN_x:H hydrogenation anneal temperature on the V_{oc} of screen-printed String Ribbon Si solar cells.

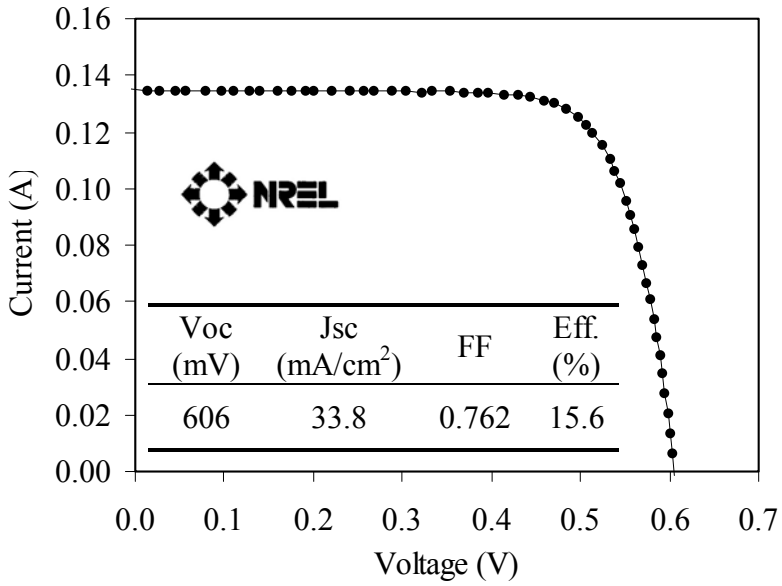

Figure 49. I-V data of the 15.6 %-efficient, 4-cm^2 String Ribbon solar cell with LF SiN_x:H-induced hydrogenation performed at 740°C. Screen-printed Ag front contacts were fired during RTA at 700°C for one second.

Therefore, in order to fabricate String Ribbon solar cells with the optimum SiN_x:H-induced hydrogenation, a two-step firing scheme is implemented. The effect of the RTA anneal temperature on the average V_{oc} of screen-printed 49-cm^2 String Ribbon cells is shown in Figure 48. Figure 48 shows that two-step firing in which the hydrogenation anneal (Step 1) is performed at temperatures in the range of 600°C to 700°C improves the V_{oc} of String Ribbon cells by only 4-7 mV over co-fired cells. As the hydrogenation anneal (Step 1) temperature is increased to 740°C, the average V_{oc} of String Ribbon cells increases to 596 mV, a 13 mV improvement over co-firing. As the anneal temperature is increased further to 800°C, the V_{oc} decreases to 582 mV, a decrease of 1 mV when compared to co-firing. The results in Figure 48 show that the optimum hydrogenation temperature for String Ribbon solar cells is 740°C, consistent with the optimum temperature of LF SiN_x:H-induced hydrogenation shown in Figure 46. This confirms that the lifetime enhancement from LF SiN_x:H is significant and beneficial to String Ribbon solar cell performance. The implementation of the two-step firing scheme with the optimized hydrogenation temperature of 740°C has resulted in 4-cm^2 screen-printed String Ribbon solar cells with efficiencies as high as 15.6% (verified by NREL), as shown in Figure 49.

7.1.3 Analysis of SiN_x:H-induced hydrogenation of defects in String Ribbon by room temperature scanning photoluminescence

Room temperature scanning photoluminescence (PL) is a technique that has been used to assess the electronic quality of mc-Si substrates. In this section, room temperature scanning PL is employed to further characterize and understand defect hydrogenation during LF SiN_x:H-induced hydrogenation. The PL spectrum of mc-Si

wafers at room temperature, under AlGaAs laser excitation, is generally composed of two broad bands: band-to-band emission which shows a maximum at 1.09eV, and a defect band PL observed at ~0.8eV [113]. The intensity of band-to-band emission, I_{bb}, and the defect band, I_{def}, can be expressed as follows [113]

$$I_{bb} = C_1 \times G \times \tau_{eff} / \tau_{rad} \tag{36}$$

$$I_{def} = C_2 \times G \times \tau_{eff} / \tau_{SRH} \tag{37}$$

$$\tau_{SRH} = \left(N_{def} v_{th} \sigma_n\right)^{-1} \tag{38}$$

where C_1 and C_2 are temperature dependent constants, G is the carrier generation rate, τ_{eff} is the effective minority carrier lifetime including surface and bulk contributions, τ_{SRH} is the radiative component of the Shockley-Read-Hall (SRH) lifetime, σ_n is the electron capture cross section, v_{th} is the electron thermal velocity, and N_{def} is the active defect concentration. Equations 36 and 37 show that I_{bb} is proportional the effective lifetime of minority carriers, and I_{def} is inversely proportional to the radiative SRH lifetime. Thus a PL map of a typical mc-Si wafer will show regions of good lifetime as high I_{bb}. I_{def} is localized in low-lifetime regions and gives inverse contrast to I_{bb} and lifetime maps [113]. The defect band has been attributed to luminescence of dislocations decorated with a low level of impurity contamination [114]. The point-by-point ratio of the two PL intensities, $R= I_{def}/I_{bb,}$ at a given illumination intensity is proportional to the concentration of electrically active defects, is given by (39) and is independent of surface or other bulk recombination channels [113].

$$\boldsymbol{R} = \text{constant} \times \boldsymbol{N}_{def} \tag{39}$$

In this study, 56 cm^2 String Ribbon samples were prepared as described in Section 7.1. PL maps of the String Ribbon samples were measured by S. Ostapenko and I. Tarasov at the University of South Florida using an AlGaAs laser diode (λ_{ex} = 804nm) as the excitation source. The PL mapping was performed after SiN_x:H deposition prior RTA, and after RTA at temperature in the range of 640°C to 800°C.

Figure 50 [115], shows the PL maps of I_{bb} (a, b) and I_{def} (c, d) and the R-parameter (e, f) measured on one representative sample, C2, before and after LF SiN_x:H-induced hydrogenation at 740°C for one minute in RTP. Figure 50 shows that I_{bb} and I_{def} increase across the wafer after RTA in sample C2. The increase of both I_{bb} and I_{def} after RTA is attributed to τ_{eff} enhancement, and has also been observed in PL maps before and after EFG solar cell processing [113]. The ratio of the average I_{bb}, I_{def}, and R-parameter for String Ribbon samples before and after RTA at various temperatures is shown in Table 14 [115]. The ratio of I_{bb}, proportional to lifetime enhancement, has a maximum value in samples B2 and C2, which were annealed at 740°C. This maximum is consistent with the maximum lifetime and V_{oc} enhancement also observed at 740°C, shown in Figures 46 and 48.

Figures 50 (e) and (f) [115] show the maps of the R-parameter for sample C2 before and after LF SiN_x:H-induced hydrogenation. It has been shown that the R-parameter is proportional to the concentration of electrically active dislocations in mc-Si [113, 114]. Figure 50 (e) and (f) show that the R-parameter across sample C2 decreases after

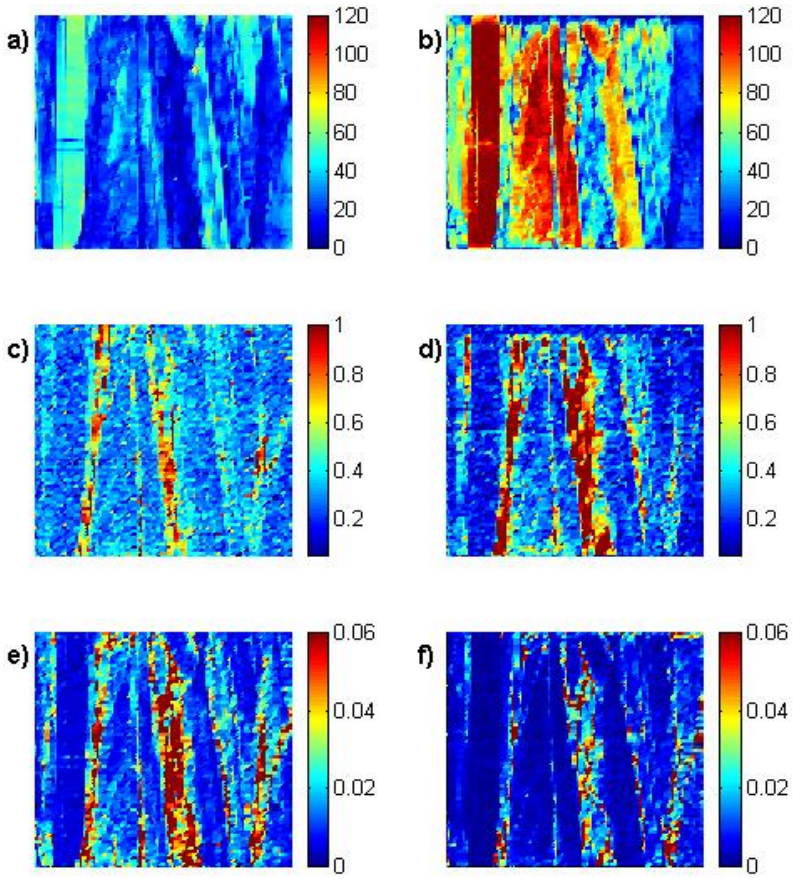

Figure 50. Room temperature PL mapping of (a,b) band-to-band intensity; (c,d) "defect" PL intensity, and (e,f) R-parameter measured before and after RTA at 740°C for 60 s in sample C2 [115].

Table 14. Ratio of average PL intensities measured on LF SiN_x:H coated String Ribbon samples before and after RTA at 640°C, 700°C, 740°C, and 800°C [115].

Wafer ID (RTP temperature)	A1 (640°C)	A2 (640°C)	B1 (700°C)	B2 (740°C)	C2 (740°C)	D1 (740°C)	D2 (800°C)
$\frac{BB(RTP)}{BB(Initial)}$	2.97	2.77	3.42	3.54	3.50	2.68	2.17
$\frac{Def(RTP)}{Def(Initial)}$	1.28	1.16	1.57	1.90	1.15	1.26	1.03
$\frac{R(RTP)}{R(Initial)}$	0.43	0.59	0.39	0.33	0.42	0.44	0.67

hydrogenation at 740°C for 1 minute. A point-by-point ratio of the two PL intensities, $R= I_{def}/I_{bb}$, was calculated and averaged across each sample in Table 14 [115] to quantify the effect of LF SiN_x:H-induced hydrogenation on defect activity. In Table 14, the reduction of the active "defect" concentration after RTA is expressed through the ratio of the average R-parameter before and after RTA. Table 14 shows that the ratio of the average R-parameter before and after RTA decreases for all samples, with the maximum reduction ($R^{RTP}/R^{Initial} = 0.33$) occurring in sample B2, annealed at 740°C. Since the R-parameter is proportional to the active dislocation density, this result indicates that the initial active dislocation density in sample B2 has been reduced by 67% by LF SiN_x:H-induced hydrogenation.

7.2 Optimization of the RTA time during LF SiN_x:H-induced hydrogenation

In Section 7.1, it was shown that the optimum anneal temperature for LF SiN_x:H-induced hydrogenation in String Ribbon is 740°C. The implementation this optimum hydrogenation anneal for high-efficiency solar cells required a two-step RTA firing scheme because prolonged firing of Ag contacts (>10 s) damages the n^+-p junction. If the hydrogenation anneal time can be reduced without degrading the lifetime enhancement, then hydrogenation, Al-BSF formation, and Ag grid firing can be performed in one step. In this section, the RTA time is reduced in an effort to merge hydrogenation, Al-BSF formation, and Ag grid firing. In addition to reducing the number of thermal processing steps, the RTA time has important consequences on hydrogenation. In this section the

effect of anneal time on the retention of hydrogen at defects is studied by lifetime measurements after successive anneals of pre-hydrogenation String Ribbon samples. Then the effect of RTA time during LF SiN_x:H-induced hydrogenation on lifetime enhancement is investigated. Finally String Ribbon solar cells are fabricated with a very short hydrogenation time. The front contacts in these solar cells are applied by photolithography and lift-off evaporation to avoid dehydrogenation of defects during Ag grid firing. To assess the effect of RTA time on defect passivation, 300 μm-thick, 3 Ω-cm p-type String Ribbon samples grown by Evergreen Solar were cleaned using the solutions listed in Appendix A. Then, P diffusion was performed at 893°C in a tube furnace using a $POCl_3$ liquid source to achieve a sheet resistance of 40-45Ω/sq. For solar cells with photolithography-defined contacts, the P diffusion temperature was reduced to achieve a sheet resistance of 80-85Ω/sq. Sample were cleaned after P diffusion and a LF SiN_x:H film was deposited on String Ribbon Si samples using a horizontal tube PECVD system operating at 50 kHz. The relevant parameters for LF SiN_x:H deposition are provided in Table 12. Samples were subjected to an in situ NH_3 plasma pretreatment performed at 50 kHz before SiN_x:H deposition. The plasma processing parameters for the in situ NH_3 plasma pretreatment steps before LF SiN_x:H deposition are also given in Table 12. After SiN_x:H deposition, an Al paste (*Ferro 53-038*) was screen-printed on the back of all String Ribbon samples. String Ribbon samples were annealed in an RTP system at temperature of 740°C for various times in the range of one second to 60 seconds. After heat treatment, the Al, n^+, and p^+ layers were removed by chemical etching and samples were cleaned before post-processing lifetime measurement using the solutions listed in Appendix A.

7.2.1 Effect of RTA on the dehydrogenation of defects and lifetime degradation in String Ribbon silicon in the absence of a supply of hydrogen

In order to investigate the dehydrogenation of defects in String Ribbon in the absence of H supply SiN_x:H, pre-hydrogenated samples were annealed successively for 1s, 10s, and 60s at RTA temperatures in the range of 400°C to 650°C. No SiN_x:H film, n^+ layer, p^+ layer, or Al were present on the samples during the anneals. It should be noted that the SiN_x:H layer on the front and Al layer on the rear of a solar cell may prevent the out diffusion of H during heat treatment. Figure 51 shows the change of the normalized carrier lifetime (τ_f/τ_o) in String Ribbon samples after dehydrogenation anneals. The lifetime degradation in String Ribbon samples during the one second, 10 s and 60 s anneals is attributed to the dehydrogenation of defects. In the case of the 60 s RTA, the normalized lifetime decreases to 0.76 after anneal at 400°C, and falls to 0.10 after anneal at 525°C. This indicates that the hydrogen passivation of defects is not stable above 400°C when the RTA time is 60 s. Figure 51 shows that when the anneal time is reduced to 10 s and one second, two distinct phases of lifetime degradation appear in the range of 400°C to 600°C. This indicates that there may be more than one mechanism that contributes to the dehydrogenation of defects. In the first phase, there is moderate dehydrogenation and the normalized lifetime drops to 0.63 after anneal at 525°C for 10 s. The moderate decrease in lifetime during the first phase may be attributed to dehydrogenation of defects that play a secondary role in limiting the lifetime. When

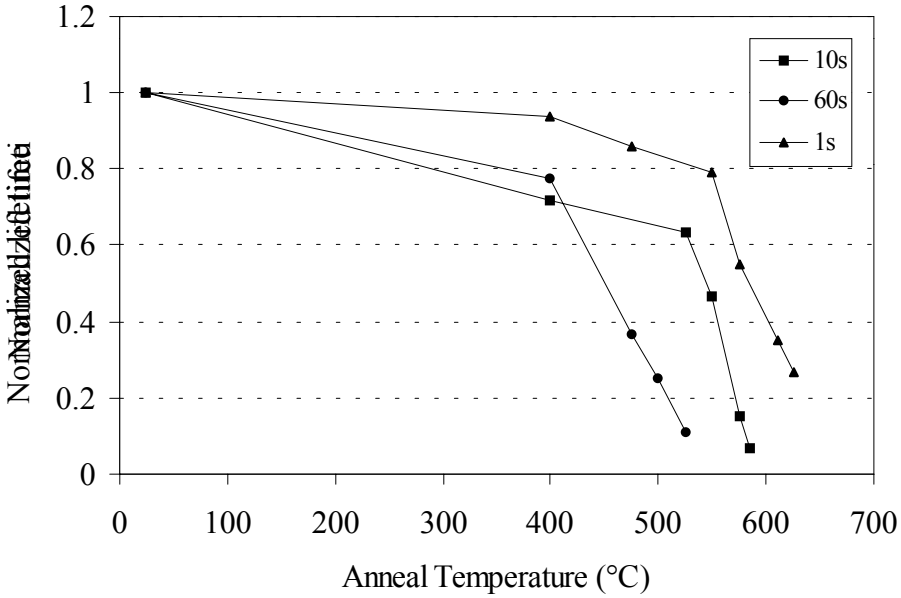

Figure 51. Decrease of the lifetime in hydrogenated String Ribbon during RTA at 400°C to 650° for 1s, 10s, and 60s.

these secondary defects are dehydrogenated, the lifetime does not drop dramatically because the primary defect remains passivated. When the RTA temperature is increased from 525°C to 550°C, a second phase of lifetime degradation begins. The normalized lifetime drops to 0.47 at 550°C for the 10 s anneal, and the dramatic decrease continues to 585°C, where the normalized lifetime reaches 0.07. For the one second anneals, moderate dehydrogenation was observed up to 550°C where the normalized lifetime was 0.79, followed by a dramatic dehydrogenation up to 625°C where the normalized lifetime falls to 0.27. This second phase of lifetime degradation may be attributed to the dehydrogenation of the primary lifetime limiting defect in String Ribbon. The results for the 10 s and one second anneals shown in Figure 51 indicate that dehydrogenation occurs at low temperatures (400-500°C), but does not become severe until temperatures above

525°C when no SiN_x:H is present on the wafer. The data also shows that the onset temperature for severe dehydrogenation increases from 525°C to 550°C when the anneal time is reduced from 10 s to one second. This indicates that hydrogenated defects can tolerate higher temperatures if the anneal time is reduced. This result could prove to be very important in designing the appropriate contact firing cycle for String Ribbon solar cells.

7.2.2 Effect of RTA time on the lifetime enhancement from LF SiN_x:H-induced hydrogenation

The effect of RTA time during LF SiN_x:H-induced hydrogenation at 740°C is shown in Figure 52. In this study, RTA for 60 s at 740°C resulted in an average lifetime of 106 μs. As the anneal time was reduced to 30 s, 20 s, and 15 s, the average lifetime decreases to 81 μs, 67 μs, and 63 μs respectively. When the anneal time was reduced further to one second, the lifetime increased to 93 μs. The decrease in lifetime between 60 s and 15 s may be due to a an imbalance between the supply of H to defects and the retention of H at defects. The study in Section 7.2.1 showed that the hydrogen passivation of defects in Si is highly unstable at temperatures above 550°C even when the anneal time is one second. This indicates that at the optimum hydrogenation temperature of 740°C, the supply of hydrogen should be very high in order to out pace dehydrogenation and result in the excellent defect passivation observed for the 60 s anneal. As the anneal time is reduced from 60 s to 10 s, the rate of the supply of hydrogen to defects may be less than the rate of hydrogen-defect dissociation and the degree of defect passivation decreases. When the anneal time is reduced to five seconds and 1s, the lifetime enhancement increases to 78 μs and 92 μs respectively. This suggests that when the anneal time is

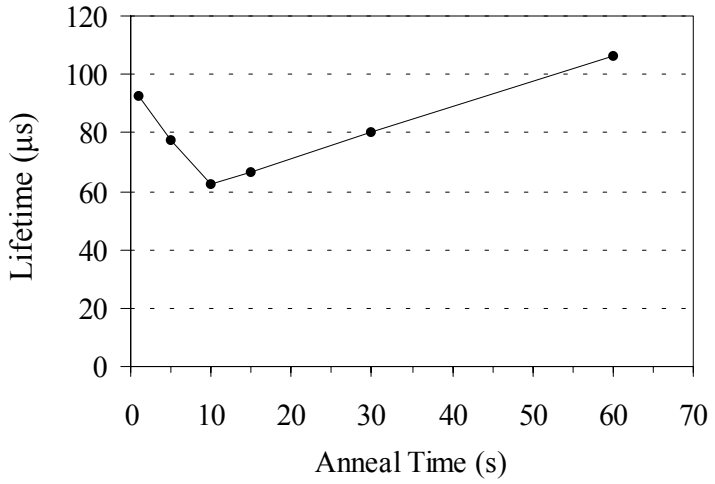

Figure 52. Effect of anneal time on lifetime enhancement from SiN_x:H-induced hydrogenation at 740°C. The average as-grown lifetime was 6 μs.

reduced below five seconds, the retention of H at defects may increase. This results in very effective lifetime enhancement (6 μs to 92 μs) because H retention is high, even though the supply of H may be low during the short RTA (one to five seconds). String Ribbon solar cells with photolithography defined contacts were fabricated to confirm that a short (one second) RTA can result in effective LF SiN_x:H-induced hydrogenation. The use of photolithography-defined front contacts avoids the need for post-hydrogenation heat treatments that may be associated with solar cells made with screen-printed Ag contacts. Figure 53 shows the illuminated current-voltage characteristics of the record-high-efficiency (17.8 %) String Ribbon solar cell verified by NREL. This solar cell was fabricated with LF SiN_x:H hydrogenation performed at 740°C for one second. This solar cell efficiency is consistent with a high bulk lifetime approaching 100 μs, an effective Al-BSF, and a double layer anti-reflection coating for this simple n^+-p-p^+ cell design.

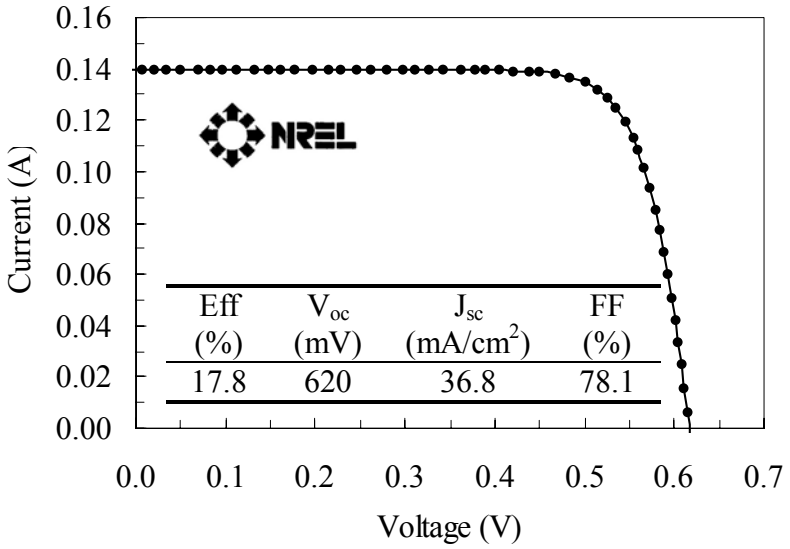

Figure 53. I-V data for the 17.8 %-efficient String Ribbon solar cell with LF SiN_x:H-induced hydrogenation performed at 740°C for one second. Front contacts were formed by photolithography and lift-off evaporation.

7.3 Conclusions

In this chapter, the optimum RTA for LF SiN_x:H-induced hydrogenation of defects in String Ribbon was established in order to understand the hydrogenation mechanism. The optimum hydrogenation anneal temperature may be the result of competition between the supply of hydrogen from the SiN_x:H film and H stored near the Si surface, and the retention of H at defects, as illustrated in Figure 47. In Section 7.1.1, the optimum RTA temperature for HF and LF SiN_x:H-induced hydrogenation in String Ribbon was found to be 800°C and 740°C, respectively. If the supply of H from LF SiN_x:H deposition is greater than that during HF SiN_x:H deposition, the effectiveness of HF SiN_x:H-induced hydrogenation may be limited by the supply of H while, LF SiN_x:H-induced

hydrogenation may be limited by the retention of H, as illustrated in Figure 47. The optimum RTA temperature (740°C) for LF SiN_x:H-induced hydrogenation was implemented in String Ribbon solar cells with screen-printed contacts. Fabrication of String Ribbon solar cells with co-fired Al and Ag contacts at temperatures above 700°C damages the junction and reduces the fill factor. Therefore, String Ribbon solar cells were fabricated with a two-step firing scheme with SiN_x:H-induced hydrogenation performed at the optimum RTA temperature of 740°C. An average V_{oc} of 596 mV, an improvement of 13 mV over co-firing at 700°C/one second, was obtained when the RTA temperature was 740°C for one minute. Room temperature scanning photoluminescence showed that I_{bb} enhancement, proportional to lifetime enhancement, was a maximized in samples annealed at 740^{o}C, consistent with the lifetime and V_{oc} maximum observed in Figure 46 and 48. Reduction of the average R-parameter, which is proportional to the active dislocation density, was maximized in a sample annealed at 740°C and indicates that the initial active dislocation density in the sample was reduced by 67% by LF SiN_x:H-induced hydrogenation.

The effect of the RTA time on LF SiN_x:H-induced hydrogenation was investigated in Section 7.2. The objective of this section was to reduce the hydrogenation anneal time, so that LF SiN_x:H-induced hydrogenation, Al-BSF formation, and Ag grid firing can be performed in one step. Very effective lifetime enhancement (6 μs to 92 μs) was observed even though the supply of H may be low during the short RTA (one second). The high average lifetime achieved during one second RTA at 740°C is attributed to the decrease in dehydrogenation of defects for this short RTA. Record-high-efficiency (17.8%) String Ribbon solar cells with photolithography defined contacts were fabricated to confirm that

a short RTA can result in effective LF SiN_x:H-induced hydrogenation. The results confirm that a high bulk lifetime approaching 100 μs and an effective Al-BSF can be achieved in during LF SiN_x:H-induced hydrogenation at 740°C in only one second.

CHAPTER 8

Fabrication and Analysis of High-efficiency Screen-printed String Ribbon Solar Cells with Single-step Firing Performed in a Conveyer Belt Furnace

Chapter 7 showed that the optimum anneal temperature for LF SiN_x:H-induced hydrogenation is 740°C, which can result in average lifetimes of 90-100 μs in String Ribbon Si. Screen-printed String Ribbon solar cells fabricated with hydrogenation performed at the optimum RTA temperature had a maximum efficiency of 15.6 %, but required a two-step RTA firing scheme. Step 1 was performed at 740°C for one minute for LF SiN_x:H-induced hydrogenation and Al-BSF formation, followed by Step 2, performed at 700°C for one second to anneal the screen-printed Ag front contacts. Chapter 7 showed that heat treatment after hydrogenation at temperatures above 550°C significantly reduces the lifetime due to the dehydrogenation of defects, even if the anneal time is one second. As a result, the optimized hydrogenation achieved in Step 1 may not be retained in the finished solar cell due to dehydrogenation of defects during

Step 2. Chapter 7 also showed that the average lifetime in String Ribbon could be improved to over 90 μs even when the RTA time at 740°C is reduced to one second. This was validated by String Ribbon solar cells with photolithography-defined contacts and LF SiN_x:H-induced hydrogenation performed at 740°C for one second that produced a record-high-efficiency of 17.8% in Chapter 7. This result confirms that the short RTA provides excellent defect hydrogenation and forms an effective Al-BSF. This result also suggests that the two-step firing can be merged into a single rapid thermal treatment that provides hydrogenation, Al-BSF formation, and Ag front contact firing. In addition, single-step rapid firing for screen-printed solar cells reduces processing time and complexity, which should reduce costs. Currently there is no commercially available RTP system for high-volume, high-throughput solar cell manufacturing. Therefore, to improve the manufacturability of screen-printed String Ribbon solar cells, the optimized RTA must be transferred to a commercially available conveyer belt furnace, which is widely used in Si solar cell manufacturing.

The final objective of this thesis is to develop and implement a manufacturable, single-step firing cycle performed in a conveyer belt furnace for LF SiN_x:H-induced hydrogenation, Al-BSF formation, and Ag contact firing. Chapters 5 and 7 showed that increasing the cooling rate above 40°C/s and reducing the anneal time to one second during SiN_x:H-induced hydrogenation in RTP may improve the lifetime enhancement. It has also been shown that the heating rate should be high to promote the formation of a uniform Al-BSF [106]. Therefore, in developing a novel conveyer belt furnace firing cycle, particular attention is paid to selecting the peak temperature, reducing the anneal time, and increasing heating rate and cooling rate. In this chapter, screen-printed String

Ribbon solar cells are fabricated using an appropriate conveyer belt furnace firing cycle. Solar cell characterization and analysis is performed on high-efficiency String Ribbon cells to assess the impact of the back surface recombination velocity on solar cell performance.

8.1 Development of a belt furnace firing cycle for co-firing of the LF SiN_x:H film for hydrogenation, Al-BSF, and Ag front contacts

The goal of this section is to develop a conveyer belt furnace firing cycle to replicate the 740°C/1s RTA that resulted in a lifetime of 92 μs demonstrated in Chapter 7. The conveyer belt furnace used in this thesis has a three heating zones, with lengths of 7.5 inches 15 inches, and 7.5 inches, respectively. Thus the total length of the heating zones in the belt furnace is 30 inches. The furnace is heated by tungsten-halogen lamps mounted above and below the conveyer belt in each of the three heating zones. The furnace temperature is monitored by a thermocouples positioned above the conveyer belt in each of the three heating zones. Automated control of the furnace allows belt speeds of 5 to 120 inches per min (ipm) to be achieved. The setpoint temperatures and belt speed for the five firing cycles (A-E) in this section are shown in Table 15. Uniform setpoint zone temperatures were selected for firing cycles A through D, and the belt speed in each was 80 ipm. Compressed and dried air was circulated through the heating and cooling zones of the furnace. The flow rate of compressed and dried air in each section of the furnace is shown in Table 16. The gas flow rate was unchanged for firing

Table 15. Belt speed and heating zone setpoint temperatures for the five belt furnace firing cycles investigated.

Firing Cycle	Belt speed (inches per minute)	Zone 1 Setpoint Temperature (°C)	Zone 2 Setpoint Temperature (°C)	Zone 3 Setpoint Temperature (°C)
A	80	800	800	800
B	80	815	815	815
C	80	850	850	850
D	80	900	900	900
E	120	955	936	600

Table 16. Flow rate (sccm) of compressed and dried air in each section of the furnace during the five firing cycle investigated.

Firing cycle	Ent. eductor	Ent. baffle	Zone 1	Zone 2	Zone 3	Ex. baffle	Ex. eductor	Plenum	Cooling section
A - D	15	100	110	150	150	100	58	40	100
E	10	25	75	100	100	100	50	40	100

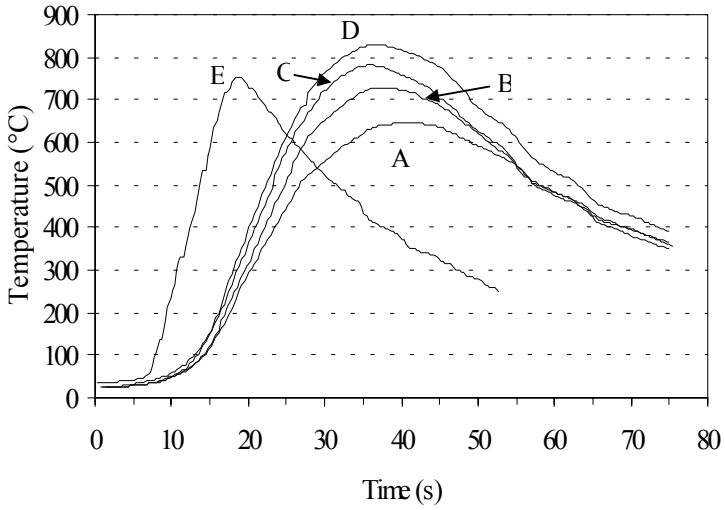

Figure 54. Temperature profile in the belt furnace for firing cycles A through E, described in Tables 15 and 16.

cycles A through D to investigate the impact of changing the zone temperature alone. The temperature measured by the internal thermocouples may differ significantly from the wafer temperature, particularly when the belt speed is high. For this reason, the wafer temperature was monitored by a thermocouple on a test wafer or the conveyer belt for the firing cycles investigated. The furnace temperature profile for firing cycles A through E is shown in Figure 54. Important characteristics of the temperature profiles, including the peak temperature, dwell time near the peak temperature, heating rate, and cooling rate, are summarized in Table 17. The dwell time near peak temperature is equal to the time above 95% of the peak temperature. The heating rate was measured from 100°C to 95% of the peak temperature, and the cooling rate is measured from 95% of the peak temperature to 400°C. Table 17 shows that when the temperature of all zones was increased from 800°C to 900°C (firing cycles A to D), the peak temperature increased

Table 17. Characteristics of the five firing cycles investigated determined from the temperature profiles shown in Figure 54.

Firing cycle	Peak temperature (°C)	Dwell time near peak temperature (s)	Heating rate (°C/s)	Cooling rate (°C/s)
A	645	13	27.0	10.3
B	729	12	34.5	12.4
C	781	11	38.9	13.4
D	831	12	40.7	13.6
E	754	4	68.8	18.7

from 645°C to 831°C, and the heating rate increased from 27.0°C/s to 40.7°C/s. Table 17 also shows that the change in the cooling rate and dwell time near the peak temperature for firing cycles A through D is 10.3°C/s to 13.6°C/s, and 11 s to 13 s, respectively.

Table 18 shows the average FF, R_{series}, and R_{shunt} of 10 String Ribbon solar cells fabrication using firing cycles A and B. Note that the excellent FF (0.779) achieved using firing cycles A and B are suitable for high-efficiency solar cells as shown in Chapter 3. However, as shown in Chapters 5 and 7, these cooling rates and dwell times are not suitable for effective SiN_x:H-induced hydrogenation. Therefore, firing cycle E was developed with a high belt speed (120 ipm) and non-uniform zone temperatures in an effort to increase the cooling rate and reduce the dwell time near the peak temperature

Table 17 shows that the cooling rate and dwell time for firing cycle E was 18.7°C/s and 4 s, respectively. Table 17 also shows that the heating rate for firing cycle E was 68.8°C/s

Table 18. Average FF, series resistance (R_s), and shunt resistance (R_{sh}) achieved using firing cycles A and B in String Ribbon solar cells.

Firing cycle	Setpoint temperature (°C)	FF	Rs (Ω-cm^2)	Rsh (Ω-cm^2)
A	800	0.779	0.66	61884
B	815	0.799	0.72	54645

and the peak temperature was 754°C. Thus, firing cycle E is a suitable match for the 740°C, one second RTA for hydrogenation.

The carrier lifetime of String Ribbon samples was measured after LF SiN_x:H-induced hydrogenation performed in firing cycle E. The average lifetime after hydrogenation in firing cycle E was 77 μs. This demonstrates that effective hydrogenation can be achieved in an industrial-type conveyer belt furnace in only one short heat treatment.

8.2 Fabrication and analysis of record-high-efficiency screen-printed String Ribbon solar cells with co-fired contacts

String Ribbon solar cells were fabricated using a single firing cycle E which should enhance LF SiN_x:H-induced hydrogenation, Al-BSF formation, and provide good ohmic contacts under the Ag grid. As explained in Section 8.1, firing cycle E should improve H retention in the finished solar cell, and reduce the solar cell processing time and complexity. Solar cell fabrication began with sample cleaning, described in Appendix A and P diffusion to form the n^+-emitter on the front surface at 893°C in a tube furnace

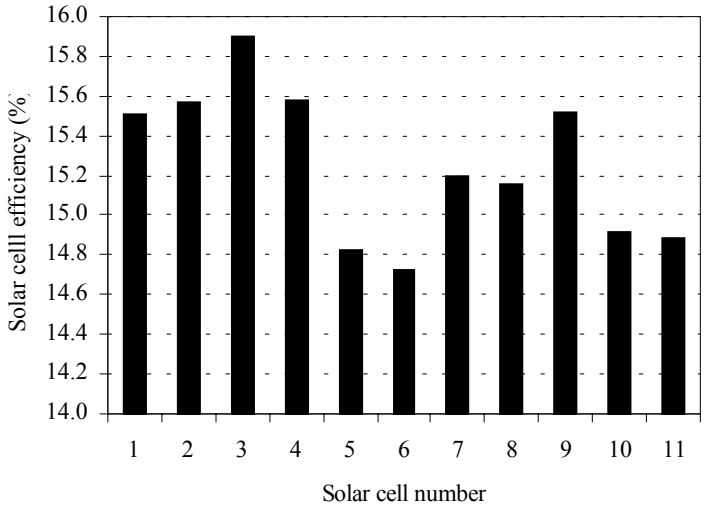

Figure 55. Efficiency distribution of String Ribbon solar cells fabricated with firing cycle E.

using a $POCl_3$ liquid source. A LF SiN_x:H film was deposited by PECVD with in-situ NH_3 plasma pretreatment on the n^+-emitter using the deposition parameters shown in Table 12. A commercially available Al paste (*Ferro 53-038*) was printed on the entire back surface and a commercially available Ag paste (*DuPont 4948*) was printed in a grid pattern on the front. Front and back contacts were co-fired in a conveyer belt furnace (*RTC LA-310*) using firing cycle E described in Tables 15, 16, and 17. Cells were isolated using a dicing saw and annealed in forming gas (10% H_2 in N_2) for 15 minute s. Figure 55 shows the efficiency distribution of 11 4-cm^2-String Ribbon solar cells fabricated with LF SiN_x:H-induced hydrogenation, Al-BSF, and Ag contacts, all provided by belt furnace firing cycle E. The average efficiency of these cells was 15.2%. The lighted I-V curve of the best cell made with firing cycle E and measured by NREL is shown in Figure 56. This cell had a noteworthy efficiency of 15.9%, the highest

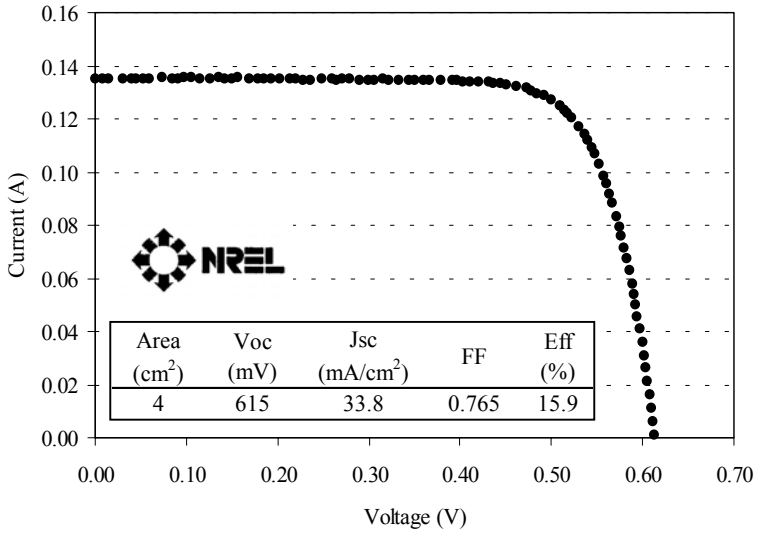

Figure 56. Lighted I-V curve of the highest efficiency String Ribbon solar cell fabricated with firing cycle E for LF SiN_x:H-induced hydrogenation, Al-BSF formation, and Ag grid firing.

efficiency achieved to date on String Ribbon silicon using screen-printed contacts. This cell was characterized by light biased IQE and QSSPC to determine the carrier lifetime and effective surface recombination velocity at the rear surface (S_{eff}). The light biased spectral response of the 15.9%-efficient cell was measured on six different regions of the 4-cm^2 cell. These six measurements were combined with one measurement of the specular reflectance of the cell to calculate six light biased IQE plots. The maximum, minimum, and average of the six IQE measurements in the long wavelength region are shown in Figure 57. For lifetime measurement, the Ag and Al contacts, SiN_x:H film, and n^+ and p^+ layers were removed from the 15.9%-efficient cell after IQE measurement by chemical etching described in Appendix A. The 4-cm^2 cell was cleaved from the ~50-cm^2 String Ribbon wafer to measure the lifetime only in the active area of the device.

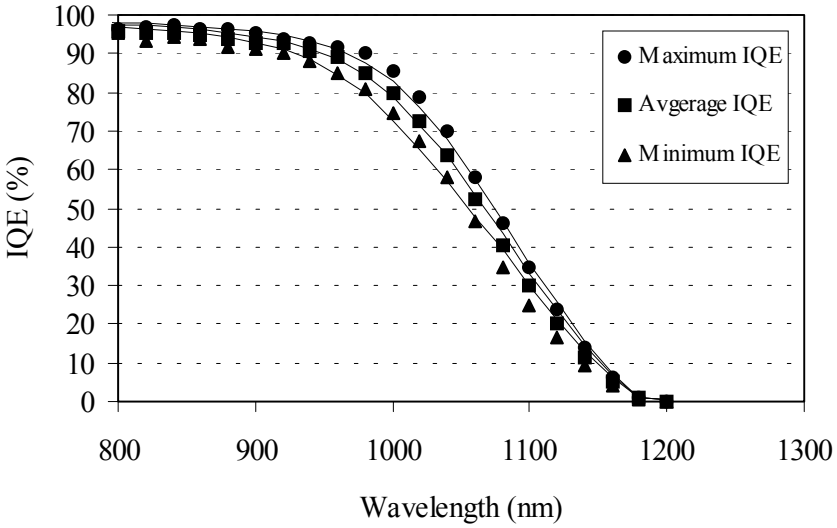

Figure 57. Maximum, minimum, and average of six measurements of the light biased IQE of the 15.9% efficient String Ribbon solar cell. The solid lines are best-fit curves generated by PC1D simulation using parameters listed in Table 18.

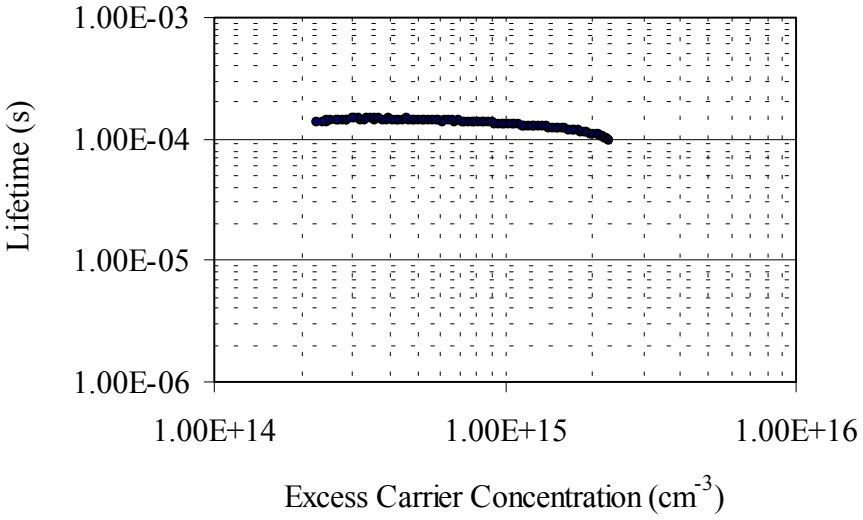

Figure 58. Bulk lifetime in the 15.9%-efficienct String Ribbon solar cell.

The cell was cleaned using the solutions shown in Appendix A and immersed in a solution of 70 mg of I_2 in 250 mL of methanol for surface passivation before lifetime measurement. Figure 58 shows the injection level dependence of lifetime measured on one location of the 15.9%-efficenct cell and indicates that LF SiN_x:H-induced hydrogenation during firing cycle E resulted in lifetime enhancement up to 140 μs. This lifetime value was used to characterize the entire cell and combined with the maximum, minimum, and average of the six light biased IQE measured on this cell, shown in Figure 57, for further analysis of S_{eff}. Figure 57 also shows the simulated IQE curves generated by the PC1D [54] solar cell simulation program. The simulated curves were generated in PC1D by adjusting S_{eff} to fit the maximum, minimum, and average of the measured IQE data, while fixing the bulk lifetime to 140 μs for all three cases. Table 19 shows that the S_{eff} values obtained from PC1D fits to the maximum, minimum, and average IQE plots were 300 cm/s, 1200 cm/s, and 575 cm/s respectively. These S_{eff} values were used to simulate device performance in PC1D to identify which value best represents S_{eff} in

Table 19. S_{eff} values used to simulate the maximum, minimum, and average long wavelength IQE for the 15.9%-efficient String Ribbon solar cell shown in Figure 57. The simulated solar cell performance based on the extracted S_{eff} values is also shown for comparison with the actual solar cell performance.

	τ_{bulk} (μs)	S_{eff} (cm/s)	V_{oc} (mV)	J_{sc} (mA/cm^2)	FF	Efficiency (%)
Actual	140		615	33.8	0.765	15.9
Min. IQE	140	1200	602	33.0	0.765	15.2
Avg. IQE	140	575	609	33.5	0.765	15.6
Max. IQE	140	300	615	33.8	0.765	15.9

the actual device. The simulated J_{sc}, V_{oc}, FF and solar cell efficiency corresponding to the extracted S_{eff} values are also shown in Table 19. The best agreement with the performance of the actual 15.9%-efficienct String Ribbon cell was obtained through PC1D simulation with S_{eff} = 300 cm/s. This result endorses the PC1D-fit method of S_{eff} extraction from the measured IQE data shown in Figure 57. Furthermore, the solar cell simulation in Figure 19 indicates that a surface recombination velocity of 300 cm/s is suitable for solar cell efficiencies in excess of 16%. It should be noted that String Ribbon Si is a spatially non-uniform material. The distribution of solar cell efficiencies shown in Figure 55 might be partly due to a variation of S_{eff} across a String Ribbon wafer. Therefore, large area String Ribbon solar cells fabricated with firing scheme E are not expected to have an S_{eff} value of 300 cm/s across the entire back surface.

8.3 Conclusions

Based on the understanding developed in Chapters 5 and 7, a single-step firing cycle performed in a conveyer belt furnace was developed and implemented in this chapter. This anneal designed to maximize LF SiN_x:H-induced hydrogenation of defects in String Ribbon, has a peak temperature of 740°C, a dwell time below five seconds, and a high cooling rate. The single-step firing cycle includes a fast heating rate to promote the formation of a uniform Al-BSF. Five belt furnace firing cycles were studied by temperature profiling, and the optimum firing cycle (E) had a peak temperature of 753°C, a heating rate of 68.8°C/s, a cooling rate of 18.7°C/s, and a dwell time near the peak temperature of four seconds. String Ribbon samples annealed in cycle E had an average

lifetime of 77 μs, confirming that this anneal is suitable for effective defect passivation. String Ribbon solar cells fabricated with firing cycle E had an average efficiency of 15.2% and a maximum efficiency of 15.9%, which is the highest efficiency to date for String Ribbon solar cells with screen-printed contacts. The bulk lifetime of this cell, measured after removal of the Ag and Al contacts, SiN_x:H film, and n^+ and p^+ layers, was 140 μs . This bulk lifetime was used together with the average, minimum, and maximum of six measurements of light biased IQE from different regions of the cell to extract the S_{eff} of the rear surface using the PC1D solar cell simulation program. The S_{eff} values obtained from PC1D-fits to the maximum, minimum, and average IQE plots were 300 cm/s, 1200 cm/s, and 575 cm/s respectively. These S_{eff} values were used to simulate device performance in PC1D to identify which value best represents the S_{eff} in the actual device. The best agreement with the performance of the actual 15.9%-efficienct String Ribbon cell was obtained through PC1D simulation with S_{eff} = 300 cm/s, endorsing the PC1D-fit method of S_{eff} extraction from the measured IQE data. Thus, firing scheme E not only provides effective defect passivation resulting in an average lifetime of 77 μs, but also forms a high quality Al-BSF with an S_{eff} as low as 300 cm/s. Extensive device modeling is performed in Chapter 9 to show that the 15.9% efficiency achieved in this chapter can be raised to 17-18% through improvements to the FF, back surface passivation, grid line width, the addition of a well-passivated, lightly doped emitter, a cell thickness of 150 μm, and a good optical reflector on the rear surface.

CHAPTER 9

Guidelines for Future Work

While String Ribbon solar cells with efficiencies as high as 15.9% with a bulk lifetime of 140 μs were achieved on 3 Ω-cm material in this thesis, considerable work remains in order to enhance the efficiency to 17-18%. In this chapter, realistic simulations of further solar cell efficiency enhancement are presented to provide guidance for future research. A roadmap is developed using practically achievable parameters that can have a significant impact on efficiency. Justification for the parameters is provided based on the progress made in this thesis and in the literature. Figure 59 shows the progression of solar cell efficiency from the 15.9%-efficienct screen-printed String Ribbon cell, achieved in Chapter 8, up to an efficiency of 17.6% without further lifetime enhancement. The inputs for these simulations are provided in Table 20. Figure 59 shows that FF improvement from 0.764 to 0.783 results in a 0.4% (absolute) increase in efficiency from 15.9% to 16.3%. This efficiency enhancement seems within reach, as FFs of 0.78 in screen-printed String Ribbon cells were achieved in Chapter 8. The next efficiency improvement in Figure 59 is due to a reduction of the back surface recombination velocity, S_b, at the p-p^+ interface. Reduction of S_b below 300 cm/s, which

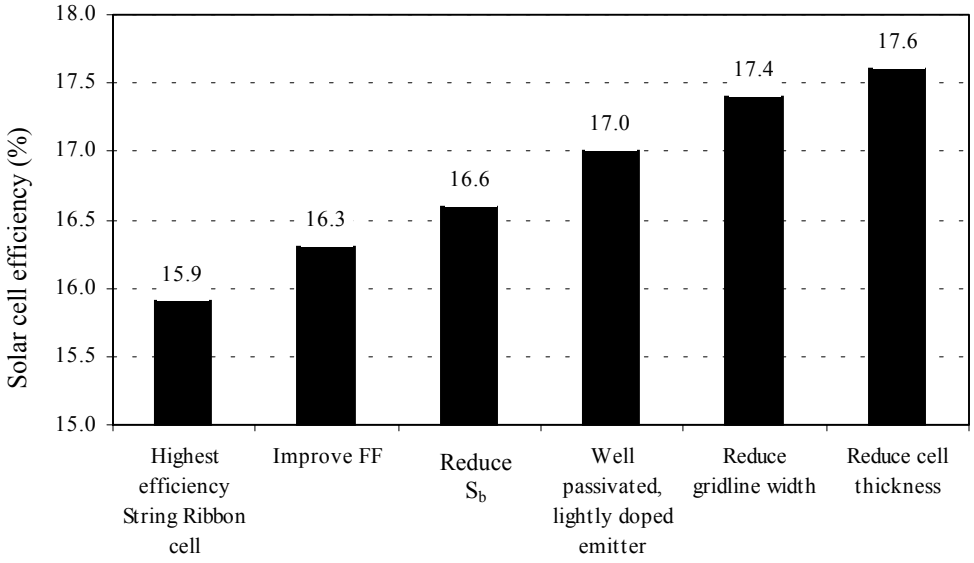

Figure 59. Simulation of planar solar cell efficiency enhancements that result from technology developments. Important simulation inputs are provided in Table 20.

was achieved in the 15.9%-efficient cell, appears to be possible based on extrapolation of (40), which predicts S_b as a function of base doping, N_A, for an 8 μm to 10 μm thick Al-BSF on float zone silicon [116].

$$S_b = 4x10^{-31} N_A^2 + 2x10^{-14} N_A + 25 \tag{40}$$

For 3 Ω-cm material, (40) predicts that the S_b in String Ribbon solar cells could be reduced to a value as low as 128 cm/s, which should drive the efficiency to 16.6%, as shown in Figure 59. Figure 59 shows that the efficiency can be improved to 17.0% through the implementation of a well-passivated (S_f = 7269 cm/s [116]), lightly-doped emitter (100 Ω/sq.). Ohmic contact to high-sheet-resistance emitters has been achieved with a very simple co-firing process, resulting in screen-printed float zone solar cell

Table 20. PC1D inputs for the simulation shown in Figures 59 and 60.

	Highest efficiency String Ribbon cell	Improve FF	Reduce S_b	Well passivated, lightly doped emitter	Reduce gridline width	Reduce thickness
Cell thickness (μm)	300	300	300	300	300	150
Bulk lifetime (μs)	140	140	140	140	140	140
S_b (cm/s)	300	300	128	128	128	128
S_f (cm/s)	35000	35000	35000	7269	7260	7260
ρ_s (Ω/sq.)	40	40	40	100	100	100
N_s (cm^{-3})	3.95×10^{20}	3.95×10^{20}	3.95×10^{20}	1.38×10^{20}	1.38×10^{20}	1.38×10^{20}
Junction depth (μm)	0.305	0.305	0.305	0.299	0.299	0.299
J_{o2} (A/cm^2)	3.0×10^{-8}	1.0×10^{-8}	1.0×10^{-8}	1.0×10^{-8}	1.0×10^{-8}	1.0×10^{-8}
R_s (Ω-cm^2)	0.9	0.8	0.8	0.8	0.8	0.8
Grid Coverage fraction	7%	7%	7%	7%	5%	5%
Rear Internal Reflectance	66% diffuse	66% diffuse	66% diffuse	66% diffuse	66% diffuse	80% diffuse
V_{oc} (mV)	616	616	622	631	632	640
J_{sc} (mA/cm^2)	33.8	33.8	34.1	34.5	35.3	35.4
FF	0.764	0.783	0.782	0.786	0.780	0.777
η (%)	15.9	16.3	16.6	17.0	17.4	17.6

efficiencies as high as 17.5% and FFs above 0.78 [117]. However, excellent emitter surface passivation, used in these simulations, is required to realize the full performance benefit of lightly-doped emitters. Figure 59 shows that the final efficiency enhancement up to 17.4% can be achieved by a reduction of the grid area coverage fraction down to 5%. Reduced grid area coverage may be achieved by reducing the Ag gridline width using emerging technologies such as the Hot Melt screen-printing technique [118]. Further efficiency enhancement up to 17.6% is possible if the cell thickness is reduced 150 μm and the rear surface internal reflectance is increased to 80% with a good optical reflector. Thus, the simulations in Figure 59 show that the lifetime enhancement (up to 140 μs) achieved in this thesis on 3 Ω-cm String Ribbon Si can result in solar cell efficiencies as high 17.6% through the combination of improved FF, reduced S_b, a well-passivated lightly-doped emitter, reduced shadow losses, and a cell thickness of 150 μm with a good reflector on the rear surface.

The simulations in Figure 60 show the effect of base resistivity as a function of bulk lifetime for further efficiency enhancement. The starting point for the simulation is the 17.4%-efficienct, 3 Ω-cm cell, whose PC1D input parameters are provided in Table 20. The S_b for each resistivity curve plotted in Figure 60 was calculated according to (37). Figure 60 reveals that when the bulk lifetime is 140 μs, the efficiency can be increased from 17.4% to 17.6% if the base resistivity is reduced from 3 Ω-cm to 1.0 Ω-cm. However, achieving a bulk lifetime of 140 μs on 1.0 Ω-cm String Ribbon may prove to be quite challenging due to the presence of dopant-defect interactions that tends to reduce the lifetime in low resistivity mc-Si [119]. Figure 60 also shows that solar cell efficiencies of about 17% can still be achieved on 0.5 Ω-cm to 1.0 Ω-cm even if the bulk

lifetime drops to 40 μs. These simulations also demonstrate that if additional lifetime enhancement can be achieved to enable bulk lifetimes in excess of 400 μs, then planar solar cell efficiencies approaching 18% can be achieved on 1 Ω-cm to 3 Ω-cm material. Further efficiency enhancement is possible, if surface texturing or light trapping can be incorporated. Thus future research should focus on developing the above-mentioned designed features in a cost-effective manner to reduce the cost of PV module fabrication below $1/W.

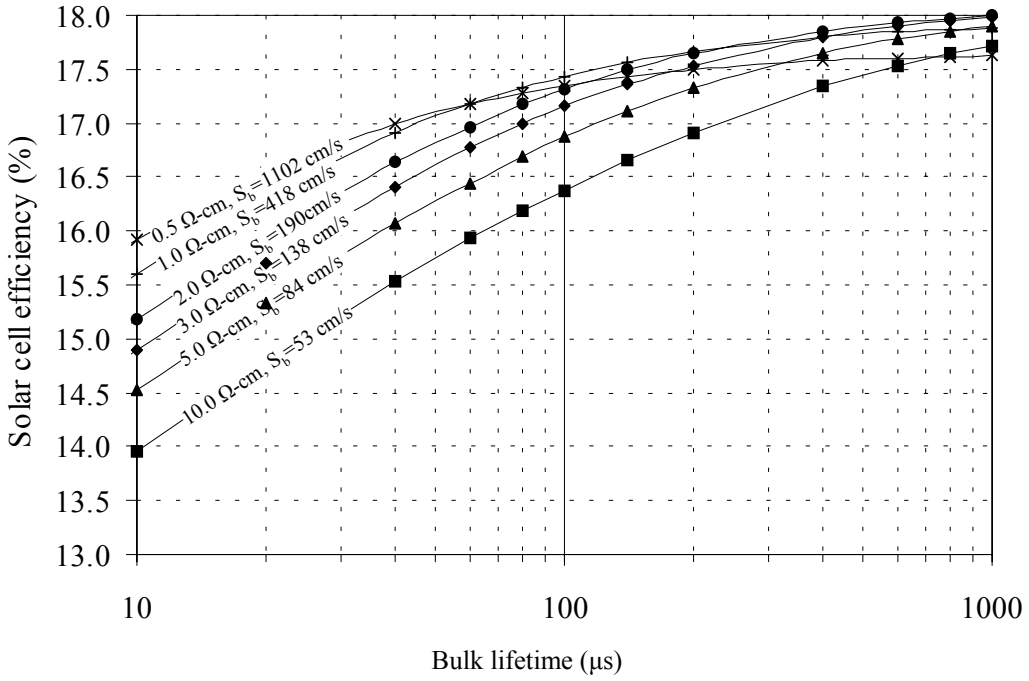

Figure 60. Simulation of the impact of bulk lifetime on planar solar cell efficiency for base resistivities in the range of 0.5 Ω-cm to 10 Ω-cm. Note that S_b varies with base doping according to (40).

APPENDIX A

Sample preparation before lifetime measurement

Al etch solution

2:2:5 HCl:H_2O_2:H_2O for 20 minutes

Ag etch solution

1:1 HNO_3:H_2O for 15 seconds

Cleaning before lifetime measurement or phosphorus diffusion

1. Rinse in DI H_2O for 5 minutes
2. HF:H_2O (1:10) for 1:30 minutes
3. Rinse in H_20 for 3 minutes
4. H_2O:H_2SO_4:H_2O_2 (2:1:1) for 5 minutes
5. Rinse in H_2O for 3 minutes
6. HNO_3:CH_3COOH:HF (15:5:2) for 3 minutes
7. Rinse in H_2O for 3 minutes
8. H_2O:HCl:H_2O_2 (2:1:1) for 5 minutes
9. Rinse in H_2O for 3 minutes
10. HF:H_2O (1:10) for 3 minutes
11. Rinse in H_2O 30 seconds

APPENDIX B

Belt furnace firing profiles

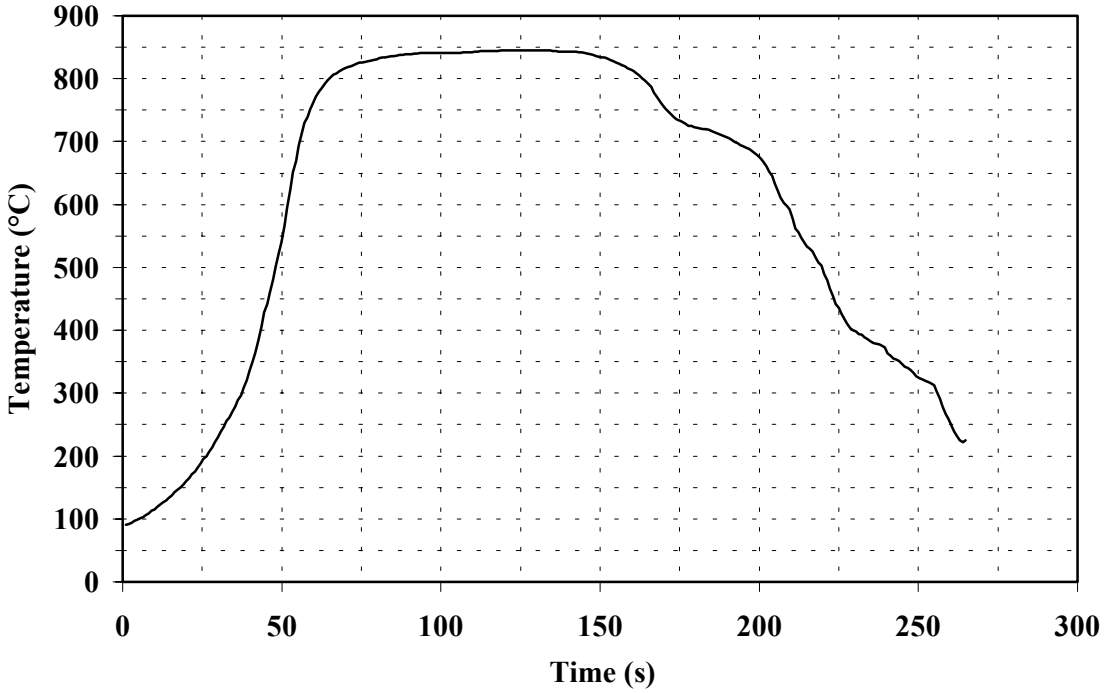

Figure 61.Temperature profile for the conveyer belt furnace firing cycle used for HF SiN_x:H-induced hydrogenation and Al-BSF formation.

Table 21. Set point temperatures and characteristics of the belt furnace firing cycle used for HF SiN_x:H-induced hydrogenation and Al-BSF formation.

Zone 1 Temp. (°C)	Zone 2 Temp. (°C)	Zone 3 Temp. (°C)	Peak Temp. (°C)	Belt speed (ipm)	Heating rate (°C/s)	Cooling rate (°C/s)	Dwell time (s)
850	850	850	845	15	20	6	98

APPENDIX B

Belt furnace firing profiles

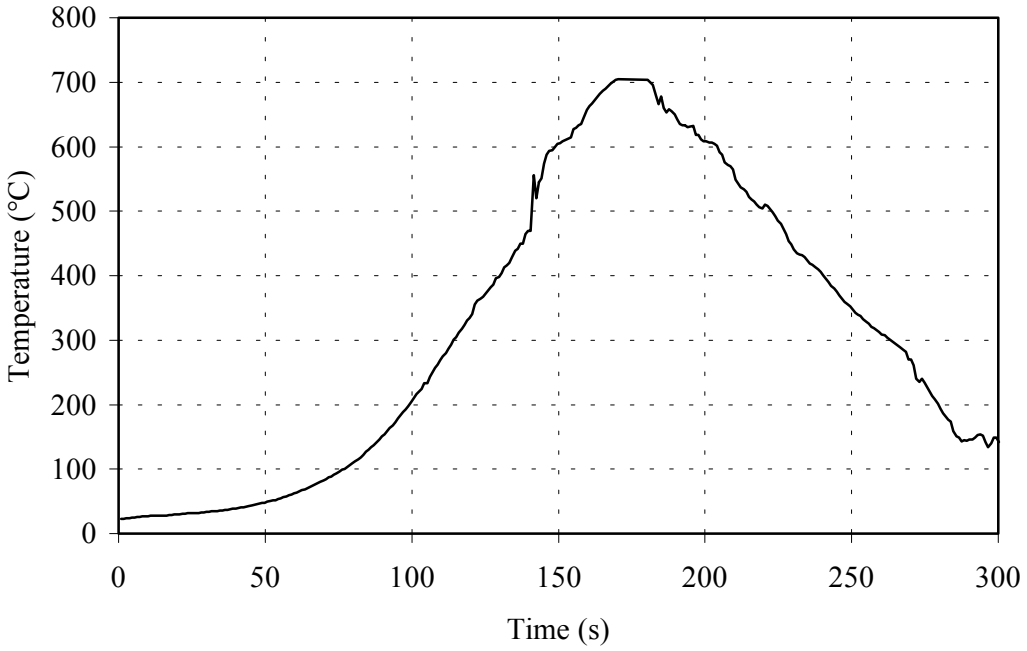

Figure 62. Temperature profile for the conveyer belt furnace firing cycle used for slow Ag grid firing.

Table 22. Set point temperatures and characteristics of the belt furnace firing cycle used for slow belt furnace contact firing.

Zone 1 Temp. (°C)	Zone 2 Temp (°C)	Zone 3 Temp. (°C)	Belt speed (ipm)	Peak Temp. (°C)	Heating rate (°C/s)	Cooling rate (°C/s)	Dwell time (s)
430	580	730	15	705	6	4	23

REFERENCES

[1] Energy Information Administration. (2001,October). *Annual Energy Review 2002*. [Online], Available: http://www.eia.doe.gov

[2] Energy Information Administration. (2001,December). *Annual Energy Outlook 2002 with Projections to 2020*. [Online], Available: http://www.eia.doe.gov/oiaf/aeo/index.html

[3] Environmental Protection Agency Clean Air Market Programs, (2001, June). *Acid Rain*. [Online], Available: http://www.epa.gov/

[4] American Wind Energy Association. (2001, June). *Global Wind Energy Market Report*. [Online], Available: http://www.awea.org/

[5] P. Maycock, PV News, vol. 22, 2003, p. 1.

[6] R. Margolis, "Photovoltaic technology experience curves and markets," presented at the *National Center for Photovoltaics Program Review Meeting*, Denver, CO, 2003.

[7] R. Moran, "Photovoltaics: Markets and Technologies", Business Communications Company, Inc. Norwalk, Connecticut, Tech. Rep. RE-038U, September 2002

[8] National Center for Photovoltaics. (1999, June). *Report of the Photovoltaic (PV) Industry Roadmap Workshop*. [Online], Available: http://www.nrel.gov/ncpv

[9] T.M. Burton, G. Luthardt, K.D. Rasch, K. Roy, I.A. Dorrity, B. Garrard, L. Teale, K. Declerq, J. Nijs, J. Szlufcik, A. Rauber, W. Wettling, and A. Vallera, "A study of the manufacture at 500 MWp p.a. of crystalline silicon photovoltaic modules," in *Proc. 14th European Photovoltaic Solar Energy Conf.,* 1997, pp. 11-16.

[10] K. W. Mitchell, "The status of polysilicon feedstock," in *Proc. National Center for Photovoltaics Program Review Meeting*, 1998, pp. 362-371.

[11] D. K. Schroder, "Carrier Lifetimes in Silicon," *IEEE Trans. Electron Devices*, vol. ED-44, pp 160-170, 1997.

[12] E. R. Weber, "Transition Metals in Silicon," *App. Phys. A*, vol. A 30, pp. 1-22, 1983.

[13] J.R. Davis, A. Rohatgi, R. H. Hopkins, P. D. Blais, P. Rai-Choudhry, J. R. McCormick, and H. C. Mollenkopf, "Impurities in silicon solar cells," *IEEE Trans. Electron Devices*, vol. 27, pp. 677-687, 1980.

[14] J.T. Borenstein, J.I. Hanoka, B.R. Bathey, and J.P. Kalejs, "Influence of ion-implanted titanium on the performance of edge-defined film-fed grown silicon solar cells," *Appl. Phys. Lett.*, vol. 62, pp. 1615-1616, 1993.

[15] L.L. Kazmerski, "Chemical, compositional, and electrical properties of semiconductor grain boundaries," *J. Vac. Sci. Tech.*, vol. 20, pp. 423-429, 1982.

[16] S. A. McHugo, A.C. Thompson, and G. Lamble, "Chemical states and stability of metal precipitates in silicon materials," in *Proc. 9th Workshop on Crystalline Silicon Solar Cell Materials and Processes*, 1999, pp. 116-119.

[17] A.A. Istratov, and E.R. Weber, "Electrical properties and recombination activity of copper, nickel, and cobalt in silicon," *Appl. Phys. A*, vol. A 66 pp. 123-136, 1998.

[18] A.A. Istratov, H. Hieslmair, E.R. Weber. "Iron and its complexes in silicon," *Appl. Phys. A*, vol. 69 pp.13-44, 1999.

[19] J. Schmidt, and A. Cuevas, "Electronic properties of light-induced recombination centers in boron-doped Czochralski silicon," *J. Appl. Phys.*, v 86, pp. 3175-3180, 1999.

[20] S. W. Glunz, S. Rein, J. Y. Lee, and W. Warta, "Minority carrier lifetime degradation in boron-doped Czochralski silicon," *J. Appl. Phys.*, v 90, pp. 2397-2404, 2001.

[21] K. Bothe, J. Schmidt, and R. Hezel, "Comprehensive analysis of the impact of boron and oxygen on the metastable defect in Cz-silicon," presented at 3rd World Conference on Photovoltaic Energy Conversion, Osaka, Japan, 2003.

[22] S. W. Glunz, S. Rein, J. Knobloch, W. Wettling, and T. Abe, "Comparison of boron- and gallium-doped p-type Czochralski silicon for photovoltaic application," *Prog. Photovoltaics: Res. Appl.*, vol. 7, pp. 463-469, 1999.

[23] J. Krinke, M. Albrecht, W. Dorsch, A. Voigt, H.P. Strunk, B. Steiner, and G. Wagner, "Grain boundaries in silicon: Microstructure and minority carrier recombination," in *Proc. of 25th IEEE Photovoltaic Specialists Conference*, 1996, pp.473-476.

[24] H. El Ghitani, and S. Martinuzi, "Influence of dislocations on electrical properties of large grained polycrystalline silicon cells: I. Model," *J. App. Phys.*, vol. 66, pp. 1717-1722, 1989.

[25] H. El Ghitani, S. Martinuzi, "Influence of dislocations on electrical properties of large grained polycrystalline silicon cells: II. Experimental results," *J. App. Phys.*, vol. 66, pp. 1723-1726, 1989.

[26] V. Kveder, M. Kittler, and W. Schroter, "Recombination activity of contaminated dislocations in silicon: A model describing electron-beam-induced current contrast behavior," *Phys. Rev. B*, vol. 63, pp. 115208-8 - 115208-11.

[27] R. Sinton, A. Cuevas, and M. Stuckings, "Quasi-steady state photoconductance, a new method for solar cell material and device characterization," *Proc. 25th IEEE Photovoltaic Specialists Conference*, pp. 457-460, 1996.

[28] A. Cuevas, and R. Sinton, "Prediction of the open-circuit voltage of solar cells from steady-state photoconductance," *Prog. Photovolt: Res. Appl.*, vol. 5, pp. 79-90, 1997.

[29] D. Macdonald and A. Cuevas, "Trapping of minority carriers in multicrystalline silicon," *Appl. Phys. Lett.*, vol. 74, pp. 1710-1712, 1999.

[30] H. M'saas, J. Michel, A. Reddy, and L. C. Kimerling, "Monitoring and optimization of silicon surface quality," *J. Electrochem. Soc*., vol. 142, pp. 2833–2835, 1995.

[31] A. Rohatgi, S. Narasimha, S. Kamra, P. Doshi, C.P. Khattak, K. Emery, and H. Field, "Record high 18.6% efficient solar cell on HEM multicrystalline material," in *Proc. 25th IEEE Photovoltaic Specialists Conf.*, 1996, pp. 741-744.

[32] J. Zhao, A. Wang, P. Cambell, and M. Green, "A 19.8% efficient honeycomb multicrystalline silicon solar cell with improved light trapping," *IEEE Transactions on Electron Devices*, vol. 46, pp. 1978-1983, 1999.

[33] S. Arimoto, M. Nakatani, Y. Nishimoto, H. Morikawa, M. Hayashi, H. Namizaki, and K. Namda, "Simplified mass production process for 16% efficiency multicrystalline Si solar cells," in *Proc. 28th IEEE Photovoltaic Specialists Conf.*, 2000, pp. 188-193.

[34] R.O. Bell and J.P. Kalejs, "Growth of silicon sheets for photovoltaic applications," *J. Mat. Res.*, vol. 13, pp. 2732-2739, 1998.

[35] M. Rinio, H. J. Moller, and M. Werner, "LBIC investigation of the lifetime degradation by extended defects in multicrystalline solar silicon," *Sol. State Phen.*, vol. 63-64, pp. 115-122, 1998.

[36] J. Cao, M. Prince, and J. Kalejs, "Impurity transients in multiple crystal growth from a single crucible for EFG silicon octagons," *J. Crystal Growth*, vol. 174, pp. 170-175, 1997.

[37] J.P. Kalejs, "Silicon ribbons and foils- state of the art", *Solar Eng. Mats and Solar Cells*, vol. 72, pp. 139-153, 2002.

[38] J. Kalejs, B. Bathey, J. Cao, J. Doedderlein, R. Gonsiorawski, B. Heath, B. Mackintosh, M. Ouellette, M. Rosenblum B. Southimath and G. Xavier, "EFG ribbon technology R&D for large scale photovoltaic manufacturing," in *Proc. National Center for Photovoltaics Solar Program Review Meeting,* 2003, pp. 200-203.

[39] A. Rohatgi, D.S. Kim, K. Nakayashiki, V. Yelundur, and B. Rounsaville, "Highest efficiency solar cells on EFG (18.2 %) and String Ribbon (17.8 %) Silicon by rapid thermal processing," *Appl. Phys. Lett*., to be published.

[40] A. Upadhyaya, K. Nakayashiki, M. Hilali, A. Rohatgi, J. Kalejs, B. Batey, and K. Matthei, "Record high efficiency screen-printed belt co-fired cells on EFG Si ribbon (16.1%) and HEM mc-Si (16.9%)", in *Proc.13th Workshop on Crystalline Silicon Solar Cell Materials and Processes*, 2003, pp. 215-218.

[41] S. Narasimha, G. Crotty, T. Krygowski, A. Rohatgi, and D. Meier, "Back surface field and emitter passivation effects in the record high efficiency n-type dendritic web silicon solar cell," *Proc. 26th IEEE Photovoltaic Specialists Conference*, 1997, p 235-238.

[42] M. Hilali, A. Ebong, A. Rohatgi, and D. Meier, "Resistivity dependence of minority carrier lifetime and cell performance in p-type dendritic web silicon ribbon," *Sol. State Electro.*, vol. 45, pp. 1973-1978.

[43] D. L. Meier, J. A. Jessup, P. Hacke, S. J. Granata, N. Ishikawa, and M. Emoto, "Production of thin (70-100 mu m) crystalline silicon cells for conformable modules," *Proc. 29th IEEE Photovoltaic Specialists Conference*, 2002, pp. 110-113.

[44] A. Schonecker, L. Laas, A. Gutjahr, M. Goris, P. Wyers, G. Hahn, and D. Sontag, "Ribbon-Growth-on-Substrate: status, challenges and promises of high speed silicon wafer manufacturing," presented at the. 12th Workshop on Crystalline Silicon Solar Cell Materials and Processes, 2002, pp 7-14.

[45] J. Rand, and J. Culik, "APex™ solar cell manufacturing," in *Proc. National Center for Photovoltaics Solar Program Review Meeting*, 2003, pp, 597-599.

[46] A. Barnett. M. Mauk. I. Hall. W. Tiller, R. Hall, and J. McNeely, "Thin-film silicon and GaAs solar cells," in *Proc. 17th IEEE Photovoltaic Specialists Conference*, 1984, pp. 747-754.

[47] A. Barnett, R. Hall, D. Fardig, and J. Culik, "Silicon-Film solar cells on steel substrates," in *Proc. 18th IEEE Photovoltaic Specialists Conference*, 1985, pp. 1094-1099.

[48] Y. Bai, D. Ford, J. Rand, R. Hall, and A. Barnett, "16.6% Efficient Silicon-Film™ Polycrystalline Silicon Solar Cells," in *Proc. 26th IEEE Photovoltaic Specialist Conf*., 1997, pp.35-38.

[49] J.I. Hanoka, "An overview of silicon ribbon growth technology," *Sol. Eng. Mats. Solar Cells*, vol. 6, pp. 231-237, 2001.

[50] R.L. Wallace, J. I. Hanoka, A. Rohatgi, and G. Crotty "Thin Silicon String Ribbon," *Sol. Eng. Mats. Solar Cells*, vol. 48 pp. 179-186, 1997.

[51] J. I. Hanoka, E. Behnin, J. Michel, M. Symko, and B. Sopori, "Growth and characterization of String Ribbon," in *Proc. 5th Workshop on Crystalline Silicon Photovoltaics*, 1996, pp. 53-53.

[52] J. I. Hanoka, "Multiple ribbon growth via the String Ribbon method," in *Proc. 13th Workshop on Crystalline Silicon Solar Cell Materials and Processes*, 2003, p. 13.

[53] J. Hanoka, "Continuous, Automated Manufacturing of String Ribbon Si PV Modules," in *Proc. of National Center for Photovoltaics Solar Program Review Meeting,* 2002, pp. 153-154.

[54] D. A. Clugston, P. A. Basore, "PC1D version 5: 32-bit solar cell modeling on personal computers," in *Proc. 26th IEEE Photovoltaic Specialist Conf*., 1997, pp. 207-210.

[55] T. Tan, P. Plekhanov, S. Joshi, R. Gafiteanu, and U. Gosele, "Physics of impurity gettering in PV silicon," in *Proc. 8th Workshop on Crystalline Silicon Solar Cell Materials and Processes*, 1998, pp. 42-49.

[56] A.J.R. de Kock, S.D. Ferris, L.C. Kimerling, H.J. Leamy, "Investigation of effects and striations in as-grown Si crystals by SEM using Schottky diodes," *Appl. Phys. Lett*., vol. 27, pp. 313-315, 1975.

[57] C.H. Seager, D.S. Ginley, "Passivation of grain boundaries in polycrystalline silicon," *Appl. Phys. Lett*., vol. 34, pp.337-340, 1979.

[58] C. Dube, J.I. Hanoka, D.B. Sandstrom, "Hydrogen diffusion along grain boundaries in silicon ribbon," *Appl. Phys. Lett*., vol. 44, pp. 425-427.

[59] S. J. Pearton, W. Corbett, and M. Stavola, *Hydrogen in Crystalline Semiconductors*. New York: Springer-Verlag, 1992.

[60] S. J. Pearton and A. J. Tavendale, "Hydrogen passivation of gold-related deep levels in silicon," *Phys. Rev. B*, vol. B 26. pp. 7105-7108, 1982.

[61] W. L. Hansen, E. E. Haller, and P. N. Luke, "Hydrogen concentration and distribution in high-purity germanium crystals," *IEEE Trans. Nuc. Sci.*, vol. NS-29 pp. 738-744, 1982.

[62] N. Fukat, K. Murakami, K. Ishioka, K.G. Nakamura, M. Kitajima, S. Fujimura, J. Kikuchi, and H. Haneda, "Thermal stability of hydrogen molecule in crystalline silicon," *Mat. Sci. Forum*, vol. 258-263, pp. 211-216, 1997.

[63] B. Bech Nielsen, "Interaction of deuterium with defects in silicon studied by means of channeling," *Phys. Rev. B*, vol. B 37, pp, 6353-6367, 1988.

[64] Van de Walle, and C. G., Tuttle, B. R., "Microscopic theory of hydrogen in silicon devices," *IEEE Transactions on Electron Devices*, vol. 47, pp. 1779-1786, 2000.

[65] A. Van Wieringen and N. Warmoltz, "On the permeation of hydrogen and helium in single crystal silicon and germanium at elevated temperatures," *Physica*, vol. 22, pp. 849-865,1956.

[66] T. Ichimiya and A. Furuichi, "Solubility and diffusion coefficient of tritium in single crystals of silicon," *Int. J. Appl. Raidat. Isot.*, vol 19, pp. 574-578, 1968.

[67] C. Kisielowski-Kemmerich, and W. Bayer, "Hydrogen desorption from crystalline silicon and its modifications due to the presence of dislocations," *J. Appl. Phys.*, vol. 66, pp. 552-558, 1989.

[68] T.S. Shi, S.N. Sahu, J. W. Corbett, and L. C. Snyder, "The state and behavior of hydrogen in silicon lattice," *Scientica Sinica*, vol. 27, pp. 98-112, 1984.

[69] S. Pearton, J. Corbett, and T. Shi, "Hydrogen in crystalline semiconductors," *Appl. Phys. A.*, vol. 43, pp. 153-195, (1987).

[70] S. K. Estreicher, and J. L. Hastings, "Defect-induced dissociation of H_2 in silicon", *Phys. Rev. B*, vol. 57, pp. 12663-12665, 1998.

[71] B. Sopori, M.I. Symko, R. Reedy, K. Jones, and R. Mason, "Mechanism(s) of hydrogen diffusion in silicon solar cells during forming gas anneal," in *Proc. 26th IEEE Photovoltaic Specialists Conf.*, 1997, pp. 25-30.

[72] B. Pivac, I. Kovacevic, and V. Borjanovic "Point defects in carbon-rich polycrystalline silicon," *Diff. Def. Data B (Sol. State Phen.)*, vol.80-81 pp.115-120, 2001.

[73] G. Hahn, P. Geiger, P. Fath, and E. Bucher, "Hydrogen Passivation of ribbon silicon- electronic properties and solar cell results," in *Proc. 28th IEEE Photovoltaic Specialists Conf.*, 2000, pp. 95-98.

[74] Y. S. Tsuo, and J. B. Milstein, "Hydrogen passivation of silicon sheet solar cells," *Appl. Phys. Lett*, vol. 45, no. 91, pp. 971-973, 1984.

[75] M. Ghannam, G. Palmers, H.E. Elgamel, J. Nijs, R. Mertens, R. Peruzzi, and D. Margadonna, "Comparison Between different schemes for passivation of

multicrystalline silicon solar cells by means of hydrogen plasma and front side oxidation," *Appl. Phys. Lett.*, vol. 62, pp. 1280-1282, 1993.

[76] M. Rosmeulen, H. E. Elgamel, J. Poortmans, M. A. Trauwaert, J. Vanhellemont, and J. Nijs, "A study on the microscopic and macroscopic effects of hydrogenation on the performance of multicrystalline solar cells," in *Proc. First World Conf. on Photovoltaic Energy Conversion*, 1994, pp. 1621-1624.

[77] M. Spiegel, G. Hahn, W. Joos, S. Keller, P. Fath, G. Wileke, and E. Bucher, "Investigation of hydrogen diffusion, effusion, and passivation in solar cells using different multicrystalline silicon base materials," in *Proc. Second World Conf. on Photovoltaic Energy Conversion*, 1998, pp. 1685-1688.

[78] R. Ludemann, A. Hauser, and R. Schindler, "Hydrogen passivation of low- and high- quality mc-silicon for high-efficiency solar cells," in *Proc. Second World Conf. on Photovoltaic Energy Conversion*, 1998, pp. 1638-1641.

[79] A. Rohatgi, Z. Chen, P. Sana, N. Evers, P. Lolgen, and R. A. Steeman, "Gettering and passivation for high efficiency multicrystalline silicon solar cells," *Optoelectronics – Devices and Technology*, vol. 9, pp. 523-536, 1994.

[80] H. Morita, A. Sato, H. Washida, T. Kato, and A. Onoe, "Efficiency improvement of solar cell utilizing plasma-deposited silicon nitride," *Jap. J. Appl. Phys*. vol. 21, pp. 47-51, 1982.

[81] F. Duerinckx and J. Szlufcik, "Defect passivation of industrial multicrstalline solar cells based on PECVD silicon nitride," *Sol. Eng. Mats. Sol. Cells*, vol. 72, pp. 231-246, 2002.

[82] Student Thesis, Bernd Stannowski, Unverstiy of Utrecht, 2002, pp. 41-45.Silicon based thin-film transistors wit high stability.

[83] W. A. Lanford, M. J. Rand, "The hydrogen content of plasma-deposited silicon nitride," *J. of Appl. Phys.*, vol. 49, pp. 2473-2477, 1978.

[84] S. Wolf and R. N. Tauber, *Silicon Processing for the VLSI Era: Volume 1 Process Technology*. Sunset Beach, CA: Lattice Press, pp. 172-173.

[85] B. Sopori, Y. Zhang, R. Reedy, K. Jones, N.M. Ravindra, S. Rangan, and S. Ashok, "Trapping and detrapping of H in Si: impact on diffusion properties and solar cell processing," *Materials Research Society Symposium,* vol. 719, 2002, pp. 125-131.

[86] I. Jonak-Auer, R. Meisels, and F. Kuchar, *Infr. Phys. Technol.*, vol. 38, 1997, pp. 223-226.

[87] A. Aberle. *Crystalline Silicon Solar Cells - Advanced Surface Passivation and Analysis*. Sydney, Australia: Centre for Photovoltaic Engineering, University of New South Wales, 1999.

[88] L. Cai and A. Rohatgi, "Effect of post-PECVD photo-assisted anneal on multicrystalline silicon solar cells," *IEEE Trans. Electron Dev.*, vol. ED 44, pp. 97-103, 1997.

[89] B. Bitnar, RQ. Glaatthaar, C. Marckmann, M. Spiegel, R. Tolle, P. Fath, G. Willeke, and E. Bucher, in *Proc .2nd World Conf. on Photovoltaic Energy Conversion*, 1998, pp. 1362-1365.

[90] F. Duerinckx, J. Szlufcik, J. Nijs, R. Mertens, C. Gerhards, C. Marckmann, P. Fath, and G. Willeke, "High efficiency, mechanically V-textured, screen-printed multicrystalline silicon solar cells with silicon nitride passivation," in *Proc.2nd World Conf. on Photovoltaic Energy Conversion*, 1998, p. 1248--1253.

[91] W. Soppe, A. Weber, H. de Moor, W. Sinke, T. Lauinger, R. Auer, B. Lenkeit, and A. Aberle, "Cost-effective mc-Si cell processing by screenprinting on remote-PECVD layers," in *Proc. 2nd World Conf. on Photovoltaic Energy Conversion*, 1998, p. 1826-1828.

[92] J. Szlufcik, K. De Clercq, P. De Schepper, J. Poortmans, A. Buczkowski, J. Nijs, and R. Mertens, "Improvement in multicrystalline silicon solar cells after thermal-treatment of PECVD silicon nitride AR coating,'in *Proc. 12th European Photovoltaic Solar Energy Conf.*, 1994, p. 1018-1021.

[93] J. Jeong, A. Rohatgi, M.D. Rosenblum, and J.P. Kalejs, "Aluminum-enhanced PECVD SiN hydrogenation of defects in edge-defined film-fed grown (EFG) multicrystalline silicon," in *Proc. 9th Workshop Crystalline Silicon Solar Cell Materials and Processes*, 1999, pp. 193-197.

[94] H. Nagel, J. Schmidt, A. Aberle, and R. Hezel, "Exceptionally high bulk minority-carrier lifetimes in block-cast multicrystalline silicon," in *Proc. 14th European Photovoltaic Solar Energy Conf.*, 1997, pp. 762-765.

[95] F. M. Roberts, and E. L. G. Wilkinson, "The effect of alloying materials on regrowth-layer structure in silicon power devices," *J. Mat. Sci.*, vol. 6, pp. 189-199, 1971.

[96] S. K. Estreicher, J. L. Hastings, and P. A. Fedders, "Hydrogen-defect interactions in Si," *Mat. Sci. and Eng.,* vol. B 58, pp. 31-35, 1999.

[97] D. A. Porter, and K. E. Easterling, *Phase Transformations in Metals and Alloys, Second Edition*. New York: Chapman and Hall, 1995.

[98] D.R. Poirier, and P.K. Sung, "Thermodynamics of hydrogen in Al-Si alloys," *Metall. and Mat. Trans.*, pp. 3874-3876, 2002.

[99] P. Anyalebechi, "Analysis of the effects of alloying elements on hydrogen solubility in liquid Al alloys," *Scripta Mettalurgica et Materialia*, vol. 33 pp. 1209-1216, 1995.

[100] M. Apel, I. Hanke, R. Schindler, and W. Schroter, "Aluminum gettering of cobalt in silicon," *J. Appl. Phys.* vol. 76, pp. 4432-4433, 1994.

[101] H. Hieslmair, S. McHugo, and E.R. Weber, "Aluminum backside segregation gettering," in *Proc. 25th IEEE Photovoltaic Specialists Conference,* 1996, pp. 441-444.

[102] A. Laugier, H. El Omari, J.P. Boyeax, B. Hartiti, J.C. Muller, L. Q. Nam, and D. Sarti, "Rapid thermal sintering of the metallizations of silicon solar cells," in *Proc. of 1st World Conf. on Photovoltaic Energy Conversion*, pp. 1535-1538, 1994.

[103] D.M. Huljic, D. Biro, R. Preu, C. C. Castillo, and R. Ludemann, "Rapid thermal firing of screen printed contacts for large area crystalline silicon solar cells," in *Proc. of 28th IEEE Photovoltaic Specialists Conf.*, pp. 379-382, 2000.

[104] A. Rohatgi, V. Yelundur, J. Jeong, A. Ebong, M.D. Rosenblum, and J.I. Hanoka, "Fundamental understanding and implementation of Al-enhanced PECVD SiN_x hydrogenation in silicon ribbons," *Sol. Eng. Mats. Solar Cells*, vol. 74, p 117-26, 2002.

[105] J. Metzdorf, W. Moller, T. Wittchen, and D. Huerhoff, "Principles and applications of differential spectroradiometery," *Metrologia*, vol. 28, pp. 247-250, 1991.

[106] S. Narasimha and A. Rohatgi, "Optimized aluminum back surface field techniques for silicon solar bells", in *Proc. of 26th IEEE Photovoltaic Specialists Conf.*, 1997, pp. 63-66.

[107] E. van de Ven, W. Connick, and A. Harrus, "Advantages of dual frequency PECVD for deposition of ILD and passivation films," in *Proc. VLSI Multilevel Interconnection Conf.*, 1990, pp. 194-200.

[108] B.L. Sopori, Y. Zang, and R. Reedy, "H diffusion for impurity and defect passivation: a physical model for solar cell processing," in *Proc. 29th IEEE Photovoltaic Specialists Conf.*, 2002, pp. 222-226.

[109] G. Agostinelli, S. De Wolf, H.F.W. Dekkers, G. Beaucarne, Q.N. Le, H.D. Goldbach, R.E.I. Schropp, I. Pinter, G. Walther, K. Schade, P. Vitanov, M. Vukadinovic, and M. Topic, "Dry Processing for crystalline silicon solar cells," in *Proc. 13th Workshop on Crystalline Silicon Solar Cell Materials and Processes*, 2003, pp. 47-54.

[110] H.F.W. Dekkers, S. De Wolf,G. Agostinelli, J. Szlufcik, T. Pernau, W. M. Arnoldbik, H. D. Goldbach and R. E. I. Schropp, "Investigation on mc-Si bulk passivation using deuterated silicon-nitride," in *Proc. 3rd World Conf. on Photovoltaic Energy Conversion*, to be published.

[111] C. Boehme and G. Lucovsky, "Origins of silicon solar cell passivation by SiNx:H anneal," *J. Non-Crystal. Sol.*, vol. 299-302, pp. 1157-1161, 2002.

[112] F. Jiang, M. Stavola, A. Rohatgi, D. Kim, J. Holt, H. Atwater, and J. Kalejs, "Hydrogenation of Si from SiNx(H) films: characterization of H introduced into the Si," *Appl. Phys. Lett.*, vol. 83, pp. 931-933

[113] S. Ostapenko, I. Tarasov, J. P. Kalejs, C. Haessler, and E-U. Reisner, "Defect monitoring using scanning photoluminescence spectroscopy in multicrystalline silicon wafers," *Semi. Sci. Tech.*, vol. 15, pp. 840-848, 2000.

[114] I. Tarasov, S. Ostapenko, W. Siefert, M. Kittler, and J. Kalejs, "Defect diagnostics in multicrystalline silicon using scanning techniques," *Physica B*, vol. 308-310, pp. 1133-1136, 2001.

[115] I. Tarasov, M. Dybiec, S. Ostapenko, A. Rohatgi, V. Yelundur, and A.M. Gabor, "Improvement of electronic quality in mc-Si wafers with SiN_x:H layer after rapid thermal processing accessed by scanning photoluminescence," in *Proc. 13th Workshop on Crystalline Silicon Solar Cell Materials and Processes*, 2003, pp. 177-181 .

[116] J. Brody, A. Rohatgi, V. Yelundur, "Bulk resistivity optimization for low-bulk-lifetime silicon solar cells," *Prog. Photovolt: Res. Appl.*, pp. 273-285, 2001.

[117] M. Hilali, V. Meemongkolkiat, and A. Rohatgi, "Advances in screen-printed high-sheet resistance emitter cells," in *Proc. 13th Workshop on Crystalline Silicon Solar Cell Materials and Processes*, 2003, pp. 211-214.

[118] T. Williams, K. McVicker, A. Shaikh, T. Koval, S. Shea, B. Kinsey, and D. Hetzer, "Hot Melt ink technology for crystalline silicon solar cells," in *Proc.29th IEEE Photovoltaic Specialists Conf.*, 2002, pp. 352-355.

[119] A. Rohatgi, W. A. Doolittle, A. W. Smith, F. V. Wald, R. O. Bell, and C. E. Dube, "Doping and oxygen dependence of efficiency of EFG silicon solar cells," in *Proc. 21st IEEE Photovoltaic Specialists Conf.*, 1990, pp. 581-587.

PUBLICATIONS FROM THIS WORK

[1] A. Rohatgi, D.S. Kim, K. Nakayashiki, **V. Yelundur**, and B. Rounsaville, "Highest efficiency solar cells on edge-defined film-fed grown (18.2 %) and String Ribbon (17.8 %) silicon by rapid thermal processing, submitted to *Appl. Phys. Lett.*, 2003.

[2] I. Tarasov, M. Dybiec, S. Ostapenko, A. Rohatgi, **V. Yelundur**, and A. M. Gabor, "Scanning room temperature photoluminescence in SiN_x:H layers," in Proc. *10th International Conference on Defects - Recognition, Imaging and Physics in Semiconductors*, to be published.

[3] D.S. Kim, K. Nakayashiki, **V. Yelundur**, B. Rounsaville, A. Rohatgi, A. Gabor, B. Bathey, and J. Kalejs, "Record high efficiency solar cells on EFG (18.3%) and String Ribbon (17.8%), in Proc. *13th Workshop on Crystalline Silicon Solar Cell Materials and Processes*, 2003, pp. 219-223.

[4] I. Tarasov, M. Dybiec, S. Ostapenko, A. Rohatgi, **V. Yelundur**, and A.M. Gabor, "Improvement of electronic quality in mc-Si wafers with SiN_x:H layer after rapid thermal processing accessed by scanning photoluminescence," in *Proc. 13th Workshop on Crystalline Silicon Solar Cell Materials and Processes*, 2003, pp. 177-181 .

[5] A. Rohatgi, **V. Yelundur**, J-W. Jeong, D.S. Kim, and A.M. Gabor, "Implementation of rapid thermal processing to achieve greater than 15% efficient screen-printed ribbon silicon solar cells," in *Proc. 3rd World Conference on Photovoltaic Energy Conversion*, to be published.

[6] D.S. Kim, A.M. Gabor, V.Yelundur, A.D. Upadhyaya, V. Meemongkolkiat, and A. Rohatgi, "String Ribbon silicon solar cells with 17.8% efficiency," in *Proc. 3rd World Conference on Photovoltaic Energy Conversion*, to be published.

[7] A. Rohatgi, **V. Yelundur**, J-W. Jeong, M. Hilali, and D.S. Kim, "Rapid Thermal Processing Enhanced Hydrogenation and Screen-Printed Contacts in Silicon Ribbon Solar Cells," in Proc. NCPV and Solar Program Review, 2003, pp. 221-224

[8] **V. Yelundur**, A. Rohatgi, J.-W. Jeong, and J. Hanoka, "Improved String Ribbon silicon solar cell performance by rapid thermal firing of screen-printed contacts," *IEEE Trans. Electron Dev*. vol. ED-49, pp. 1405-1410, 2002.

[9] S. Bowden, **V. Yelundur**, and A. Rohatgi, "Implied-Voc and Suns-Voc measurements in multicrystalline solar cells, in Proc. *29th IEEE Photovoltaic Specialists Conf.*, 2002, pp. 371-374.

[10] A. Rohatgi, **V. Yelundur**, and J. Jeong, A. Ebong, M.D. Rosenblum, and R.L. Wallace, "Fundamental understanding and implementation of Al-enhanced PECVD SiN_x hydrogenation in silicon ribbons," *Sol. Eng. Mats. Sol. Cells*, vol. 74. pp. 117-126, 2002.

[11] A. Rohatgi, **V. Yelundur**, and J. Jeong, A. Ristow, M. Hilali, B. Damiani, "Recent advances and approach toward low-cost high-efficiency multicrystalline silicon solar cells," in *Proc.11th International Workshop on the Physics of Semiconductor Devices*, vol. I, 2001, pp. 73-80.

[12] A. Rohatgi, **V. Yelundur**, and J. Jeong, "Lifetime enhancement and low-cost technology development for high-efficiency manufacturable silicon solar cells," in Proc. *11th Workshop on Crystalline Silicon Solar Cell Materials and Processes*, 2001, pp. 80-84.

[13] J. Jeong, A. Rohatgi, **V. Yelundur**, A. Ebong, and M.D. Rosenblum, J.P. Kalejs, "Enhanced silicon solar cell performance by rapid thermal firing of screen-printed metals," *IEEE Trans. Electron Dev.*, vol. 48, pp. 2836-2840, 2001.

[14] J. Brody, A. Rohatgi, and **V. Yelundur**, "Bulk resistivity optimization for low bulk-lifetime silicon solar cells," *Prog. Photovolt: Res. Appl.*, vol. 9, pp. 273-285, 2001.

[15] **V. Yelundur**, A. Rohatgi, A. Ebong, A.M. Gabor, J. Hanoka, and R.L. Wallace, "Al-enhanced PECVD SiN_x induced hydrogen passivation in String Ribbon silicon," *J. of Electr. Mats.*, vol. 30, pp. 526-529, 2001.

[16] A. Rohatgi, **V. Yelundur**, and J. Jeong, "High-efficiency screen printed silicon ribbon cells through process-induced enhanced hydrogenation and gettering," in *Proc. of the NCPV Program Review Meeting*, 2001, pp.159-160.

[17] **V. Yelundur**, J. Jeong, A. Rohatgi, M. D. Rosenblum, and R.L. Wallace, "Understanding and optimization of Al-enhanced SiN_x induced defect passivation in ribbon silicon," in *Proc. 10th Workshop on Crystalline Silicon Solar Cell Materials and Processes*, 2000, pp. 228-233.

[18] Rohatgi, **V. Yelundur**, J. Jeong, A. Ristow, A. Ebong, and B. Sopori, "Advances in low-cost multicrystalline silicon solar cell processing in the last decade," in *Proc. 10th Workshop on Crystalline Silicon Solar Cell Materials and Processes*, 2000, pp. 12-20.

[19] **V. Yelundur**, A. Rohatgi, A.M. Gabor, J. I. Hanoka, and R. L. Wallace, "PECVD SiN_x induced defect passivation in String Ribbon," in *Proc.28th IEEE Photovoltaic Specialists Conference,* 2000, pp. 91-94.

[20] A. Rohatgi, A. Ebong, **V. Yelundur** and A. Ristow, "Rapid thermal processing of next generation silicon solar cells," *Prog. Photovolt: Res. Appl.*, vol. 8, pp. 515-527, 2000.

[21] A. Rohatgi, **V. Yelundur**, J. Jeong, A. Ebong, D. Meier, A.M. Gabor, and M. Rosenblum, "Aluminum enhanced PECVD SiN_x hydrogenation in silicon ribbons," in *Proc. 16th European Photovoltaic Solar Energy Conf. and Exhibition,* 2000.

[22] A. Rohatgi, A. Ebong, **V. Yelundur** and A. Ristow, "Rapid thermal processing of next generation silicon solar cells," in *Proc. 10th International Workshop on the Physics of Semiconductor Devices*, 1999.

[23] **V. Yelundur**, A. Rohatgi, A.M. Gabor, J. Hanoka, and R. L. Wallace, "Understanding and optimization of manufacturable defect gettering and passivation treatments on String Ribbon silicon," in *Proc. 9th Workshop on Crystalline Silicon Solar Cell Materials and Processes*, 1999, pp. 223-227.

[24] S. Venkataraman, R. Singh, V. Parihar, K. F. Poole, A. Rohatgi, **V. Yelundur**, and A. Ebong, "A study of the effect of ultraviolet (UV) and vacuum ultra violet (VUV) photons on the minority carrier lifetime of single crystal silicon processed by rapid thermal and rapid photothermal processing," *J. of Electr. Mats.*, vol. 28, pp. 1394-1398, 1999.

[25] **V. Yelundur**, A. Ebong, S. Kamra, A. Rohatgi, J. Hanoka, and A. Gabor, "Approach towards high efficiency, manufacturable thin String Ribbon silicon solar cells," in *Proc. 8th Workshop on Crystalline Silicon Solar Cell Materials and Processes*, 1998, pp. 240-243.

[26] A. Ebong, **V. Yelundur**, and A. Rohatgi, "Effective surface and bulk defect passivation of low resistivity multi-crystalline silicon by annealed RTO/PECVD SiN stack", in *Proc. 8th Workshop on Crystalline Silicon Solar Cell Materials and Processes*, 1998, pp. 232-235.

VITA

Vijay Nag Yelundur was born on July 1, 1975 in Danbury, Connecticut. He earned his Bachelor's of Science Degree in Materials Science and Engineering from the Georgia Institute of Technology in 1997. He is currently pursuing the Doctorate of Philosophy from the Georgia Institute of Technology in School of Materials Science and Engineering, under the supervision of Dr. Ajeet Rohatgi in the University Center of Excellence for Photovoltaic Research and Education. His graduate research has focused on the understanding and development defect passivation techniques for low-cost, high-efficiency silicon solar cells. This work has resulted in over 20 publications in professional journals and conference proceedings.